DISCOTIC LIQUID CRYSTALS AND POLYMERSOMES:

MOLECULE GONIOMETERS

A Dissertation

by

YA-WEN CHANG

Submitted to the Office of Graduate Studies of
Texas A&M University
in partial fulfillment of the requirements for the degree of

DOCTOR OF PHILOSOPHY

August 2012

Major Subject: Chemical Engineering

Discotic Liquid Crystals and Polymersomes: Molecule Goniometers

DISCOTIC LIQUID CRYSTALS AND POLYMERSOMES:

MOLECULE GONIOMETERS

A Dissertation

by

YA-WEN CHANG

Submitted to the Office of Graduate Studies of
Texas A&M University
in partial fulfillment of the requirements for the degree of

DOCTOR OF PHILOSOPHY

Approved by:

Co-Chairs of Committee,	Zhengdong Cheng
	Victor M. Ugaz
Committee Members,	Arul Jayaraman
	Paul S. Cremer
Head of Department,	Charles Glover

August 2012

Major Subject: Chemical Engineering

ABSTRACT

Discotic Liquid Crystals and Polymersomes: Molecule Goniometers. (August 2012)

Ya-Wen Chang, B.S., National Taiwan University

Co-Chairs of Advisory Committee: Dr. Zhengdong Cheng
Dr. Victor M. Ugaz

Controlling the assembly of amphiphilic molecules and micron-sized, disk-shaped particles at different length scales into ordered structures enables bottom-up organization which is of great interest to emerging technologies based on structured materials. The primary object of this work is the investigation of structure forming components — Zirconium phosphate (ZrP) discotic particles and polymersomes/amphiphiles on their self-assembly and interactions.

The effect of bilayer architecture of polymersomes on surface reactivity was investigated via fluorescent probing method. Established through complementary experiments, correlation between reactivity and molecule diffusivity in polymer-rich environment revealed the mechanism of reduced reactivity when tethered reactive groups are located deeper within the hydrophilic polymer layer.

The phase diagram of charged nanoplatelets was constructed as a function of particle concentration, surface cation moiety, and ionic strength. Influence of surface cation on the isotropic-nematic transition was done by measuring the transition boundaries of discotic suspensions prepared by acid-base exfoliation reaction with a series of exfoliating agents. Furthermore, a novel phase transition was found, where

platelet-platelet interaction was influenced synergistically by ionic strength and ion exchange. At low pH, directional inter-platelet attractions lead to the formation of low volume fraction colloidal gels. Alternative surface modification approaches, including biomolecule deposition and alkyl chain grafting were explored.

Finally, self-assembly of platelets in emulsions and oil-water interface was examined. Surface modification was applied to link surface properties to stable emulsion-forming ability in mixed surfactant-particle system. Emulsion uniformity was achieved by microfluidic flow focusing method. Surface engineering and interaction control was demonstrated throughout this work to be viable approaches to the fundamental understanding of collective behaviors of individual building blocks.

To my family

ACKNOWLEDGEMENTS

There are a number of people I would like to thank for helping me through this stage of my life. First, I need to acknowledge my co-chairs, Dr. Victor Ugaz and Dr. Zhengdong Cheng for their guidance and encouragement. I am grateful to Dr. Ugaz for helping me through the transitional times during the course of my studies, and gave me the freedom to peruse research paths that speak most to my interests. I owe a big thank you to Dr. Cheng, for giving me the opportunity to work with him. His dedication to research and insights into fundamental problems lead to numerous inspiring conversations and discussions that refined this work. As a good mentor, he never hesitates to help me in various aspects of my academic career. I would also like to express my gratitude to my former advisor, Dr. James Silas, who helped shape me as a scientist and initiated my passion for research, and to Dr. Michael Bevan for teaching me the fundamentals of colloidal science. I would like to thank my committee members, Dr. Paul Cremer and Dr. Arul Jayaraman, for their support throughout the course of this research. Thanks go to Dr. Akbulut Mustafa and Dr. Manuel Marquez for their input and feedback on my research.

Thanks also go to my friends and current/former colleagues: Dr. Jeffery Gaspard, Dr. Karym Kinnibrug, Dr. Peng He, Clemente Contreras, Andres Mejia, Min Shuai, Yi-Hsien Yu, Scott Henderson, Tony Huang, Yu-Wen Huang, and Serdar Ozturk. This dissertation would not have been possible without the help and contribution from the

others. Massive thanks to the department faculty and staff for making my time at Texas A&M University a great experience.

Last but not least, I'd like to thank my mum and dad for their endless love and support throughout the years. They have given me, for as long as I can remember, every opportunity to make my own life decisions and career choices, even if it means leaving them behind on the other side of the planet. For this, I am forever in their debt. Thanks also extend to my partner, Gregory Fernandes, for the words of encouragement that kept me going through all the ups and downs in this process.

TABLE OF CONTENTS

LIST OF FIGURES

LIST OF TABLES

CHAPTER I

INTRODUCTION

1.1 Objectives and Significance

Self-organization of nature's most minute units, molecules, or colloidal particles is one of the most basic yet perplexing phenomena that reflect information of the building blocks through its collective behaviors. The ability to precisely control interactions of the individual units to arrange them into desired order and functions is a longstanding quest and pivotal to emerging technologies based on structured materials. Self-assembly is a general strategy acceptable at all scales,[1] and encompass much more than single-level organization. Bicelles (bilayered micelles), for instance, are disk-shaped molecular assemblies from lipids/surfactants, with liquid crystalline (lamellar) bilayer structure. These discotic particles (bicelles), again self-orient in a suspension at high volume fraction or under external magnetic field. Hence, controlling self assembly in soft matters (e.g., liquid crystals, emulsions, amphiphilic molecule mesophases) at different length scales enables creation of novel materials for various applications. In addition to its own macroscopic properties as an assembly, some soft matter could also serves as medium that induce or direct the interaction of surrounding molecules, what is being referred to here as "**molecule goniometers**" (the term was originally coined for bicelle liquid crystal systems[2] that aligns biomolecules).

_____

This dissertation follows the style of *Journal of Ameircan Chemical Society*.

The main objective of this dissertation is to design self-assembled systems in which the surface properties of the components and inter-particle interactions can be controlled to construct aggregates or ordered materials. Compared to systems consist of rigid, spherical particles, soft "squishy" particles and anisotropic particles, in particular disks are a lot less researched and understood. Thus, the objective is approached through the use of two classes of soft materials, namely synthetic di-block copolymer vesicles and inorganic, disk-shaped particles. Some of the central questions we are seeking answers to in this dissertation are (1) how polymersome surface structure influences surface reactivity, (2) what type of structure will deformable particles (polymersomes) form under strong attraction, (3) how various parameters including aspect ratio, polydispersity, inter-particle interaction would change the phase diagram and the assembly behavior of discotic suspensions, and (4) how disk particles self-assemble in emulsion droplets. Surface modifications (physical and chemical bonding) and solvent mediated interactions (salt or polymer concentrations, type of solvents) were utilized to systematically vary properties of the building blocks, and the overall properties of the assemblies were evaluated experimentally. These strategies offer valuable information to investigate property relationships between the building units and the structure established. Active control over the stability and self-assembly of these complex fluids is then possible via the fundamental research carried out throughout this study.

1.2 Background

1.2.1 Polymersomes from Di-block Copolymers

Biomembranes and vesicles play a critical role in various chemical and biological functions from the day that a cell began to exist. Since the introduction of fluid mosaic model by Singer and Nicolson,[3] which describes cell membranes as two dimensional fluids of lipids and proteins, where the proteins are embedded in the ordered matrix of phospholipids, groups of material and polymer scientists have developed artificial membranes to improve stability, control inter-membrane dynamics and incorporate functionalities. The synthetic di-block copolymer is an example amongst the different building blocks[4-5] for artificial memberanes that share the same amphiphilic features to phospholipids. Amphiphilic molecules, due to its dual hydrophilic and hydrohpobic properties, are thermodynamically driven to self-assembly in solution, usually arranged into structures with polar groups facing the aqueous phase, and the nonpolar parts buried in the hydrophobic interior. Depending on the architecture of the molecules (i.e. size ratio between the hydrophobic to hydrophilic block, effective hydrodynamic volume of the headgroup or hydrophilic region), micelles, cylindrical micelles, planar bilayers, or vesicles can be obtained[6]. Self-assembled polymer vesicles, or polymersomes, are hollow, spherical capsules with hydrophobic bilayer membrane and hydrophilic internal and external coronas (Figure 1.1a), with size in nanometers to tens of microns.
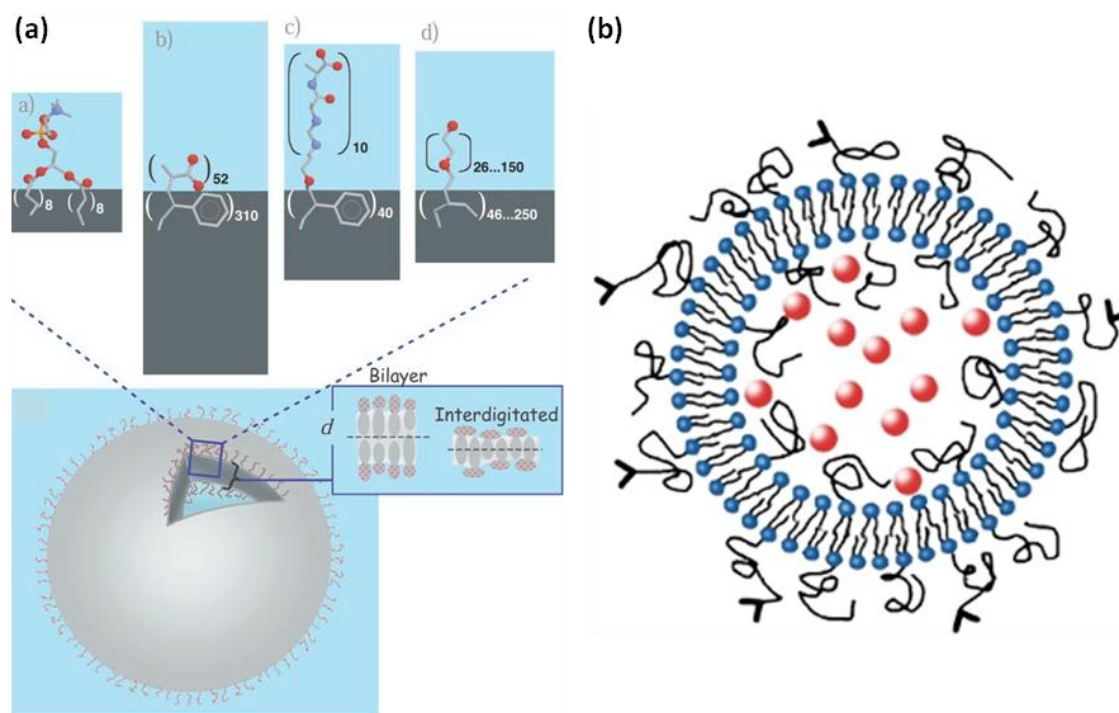
Figure 1.1. (a) Schematic structure of a vesicle and vesicle forming lipids and di-block copolymers[4]. (b) Schematic of a stealth liposome with phospholipids and headgroup-grafted PEG layer.[7]

The early development of polymers on vesicular structures stems from the need to improve the stability and "stealth property" of lipid vesicles or liposomes (Figure 1.1b). This is achieved by the introducing polyethylene glycol (PEG) grafted lipids (Pegylated lipids) into liposome formulation.[8-9] The biocompatible polymer chains anchored onto liposomes were designed to act similar to glycocalyx as repellent, to resist adsorption of components of the immune systems. The polymeric surface structure creates the colloidal effect "steric stabilization", a repulsive force whose range dependents on thickness and conformation of the polymer layer. The repulsive forces keep the vesicles dispersed and separated from other interacting surfaces, and result in

prolonged lifetime in bloodstream from an application standpoint. The Pegylated lipids, though can be mixed into liposomes, do not form vesicles in aqueous on their own and tend to de-mix and segregate when lipid composition contain up to 10% PEG-lipids.[10] The development of polymer vesicles overcame some of the major stability issues of liposomes, and was soon regarded an alternative candidate for viral drug carrier.[11-12]

Surface modification of polymersomes is of great importance in its applications as sensors, nanoreactors, and in drug delivery applications.[11-14] Conjugation chemistries that provide stable functional group attachments is considered state-of-the-art;[15] The other essential consideration in designing functional polymersomes to meet optimized performance is on structures: how surface interactions are governed by the architecture of the polymer layer presenting the target molecule.[16-18] This is the area in which we will explore by combining a new surface modification approach and quantitative fluorescence measurements.

1.2.2 Colloidal Particles and Suspensions

Colloidal suspensions are omnipresent, and can be encountered pretty much everywhere in the surroundings of our daily life; from the toothpaste we use first thing in the morning, the glass of milk to go with your cereal, the dust particles that appears to fly around in the air, the clay mineral particles that compose of our soil, to the latex paint we apply to the walls, and the list goes on. Colloids are tiny particles with diameter in between approximately 1nm to 10 micron, where surface phenomenon (associated with the large surface areas) and Brownian motion from thermal fluctuations are of extreme importance. The physical state of colloidal dispersions is determined by how the

particles interact across the dispersion medium, which complexity originates from the intricate balances between Brownian and various attractive and repulsive forces acting among the particles.[19] The spatial distributions and the dynamics of the particles in colloidal dispersions describe the stability and phase behaviors of the suspensions. They can assume fluid, ordered crystal, gel, or glass state. While "colloid" is generally defined by size, the following will described the considerable importance of particle shape on microscopic properties of colloidal suspensions.

1.2.3 Self-assembly of Colloidal Particles

Due to their close resemblance to atomic systems, colloidal suspensions have been used extensively as model systems to experimentally probe physical behavior such as crystallization, melting and other types of phase transitions. For spherical particles interacting through hard-core potential or weak attractions, the suspensions display fluid or gas to crystal (solid) phase transition with increased concentration. These transitions are the same as in atomic or molecular matters.[20-22] Monodisperse, spherical colloids self-assemble into ordered, periodic three-dimensional lattices—colloidal crystals, at certain volume fractions depending on their interactions. The periodic structure also finds its way to many applications involving the devolvement of new types of diffractive devices such as optical sensors[23] and photonic bandgap materials.[24]

It was discovered almost a century ago that anisotropic particles, e.g. disks[25] and rods,[26-27] display an isotropic to nematic phase transition. While the isotropic phase is equivalent to the fluid phase for spheres, which exhibits no long-range positional or orientational order, the nematic liquid crystal phase has long-range orientaional order

even though no positional order is in place (Figure 1.2a). The nature of liquid crystal phase transition was later recognized by Onsagar[28] as the gain in excluded volume entropy due to anisotropic shape of the particles. The competition between excluded volume (or free volume) entropy (to maximize the space between particles, which favors particle alignment) and the orientational entropy (which favors random particle orientation) determines the nematic phase stability. The former term dominates when increase particle volume fraction or shape anisotropy. The Helmholtz free energy for isotopic-nematic transition of hard cylinders with length L, diameter D, and volume V based on Onsagar-Parson theory is described by[29]

$$\frac{\beta F}{N} = \ln \frac{V}{D^3} - 1 + \left\langle \ln 4\pi f\left(\bar{u}\right) \right\rangle + c \frac{G_p(\phi)}{2} \frac{\left\langle\left\langle V_{excl}(\gamma) \right\rangle\right\rangle}{D^3} \tag{1.1}$$

where $\beta^{-1} = k_B T$ is the thermal energy, V/D^3 is the dimensionless thermal volume, c is particle concentration ND^3/V, the brackets denote single and double orientational average over a distribution f($\bar{u}$) of the unit vector $\bar{u}$, which is normalized to $\int d\bar{u}f(\bar{u}) = 1$. G_p is the scaling factor that incorporates the effect of higher than second-order vial terms, which when approaches unity (as $\phi \rightarrow 0$), recovers the Onsagar free energy description. The first and second term in Eq. 1.1 correspond to the translational and orientational entropy, respectively. The last term represents the packing entropy, which includes the key quantity, the excluded volume V_{excl} between two cylinders at fixed inter-cylinder angle γ. This parameter has been calculated by Onsagar as the following.[28]

$$\frac{V_{excl}(\gamma)}{D} = \frac{\pi}{2}|\sin\gamma| + \frac{L}{D}\left(\frac{\pi}{2} + 2E(\sin\gamma) + \frac{\pi}{2}\cos\gamma\right) + 2\left(\frac{L}{D}\right)^2 |\sin\gamma| \tag{1.2}$$

Positional ordering in one and two dimensions further gives rise to other liquid crystal phases known as the lamellar (or smectic) and hexaganol (or columnar) phases, both of which could occur theoretically for suspensions of rod[30-31] or disk-like particles.[32] Experimental verification of these computer simulated phase transitions was to follow throughout the years.[33-35]
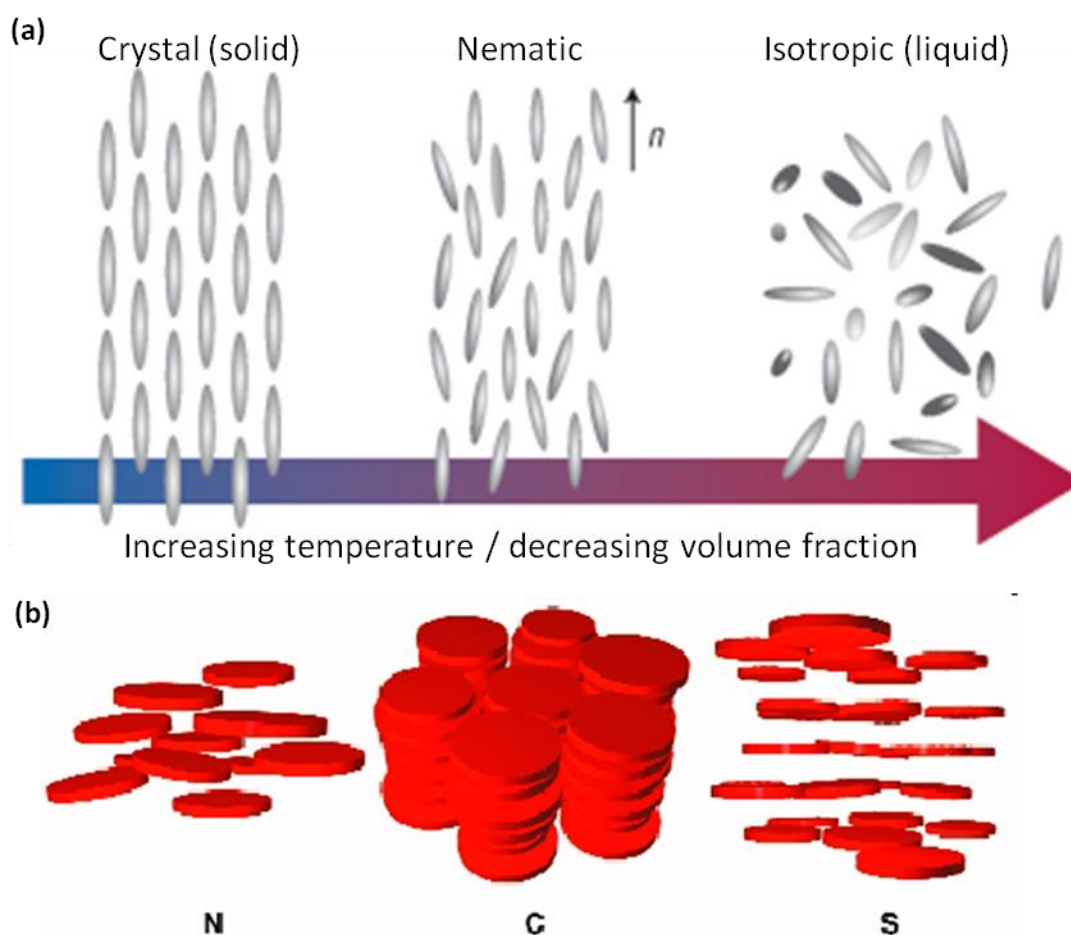
Figure 1.2. Example liquid crystal phases for rods and disks. (a) Comparison between crystalline, nematic and isotropic phases composed of rod-shaped molecules or particles, n is the nematic director. Melting of ordered phases is achieved via increasing temperature (thermotropic calamitic liquid crystal materials) or decreasing particle volume fraction. (b) Schematic of nematic, columnar and smectic phases for discotic liquid crystals. Figure is modified from literature[35-36].

1.2.4 Discotic Liquid Cystals

Discotic liquid crystals (of disk-like molecules) distinguish itself from the more widely used calamitic (rod-like molecules) liquid crystals by the shape of the mesogens (building blocks, in our case colloidal particles)[37]. Common categories of discotic mesophases are nematic, columnar, and smectic phases (Figure 1.2b). Accurate calculations to describe the phase diagram of discotic suspensions are more challenging than its rod-shaped counterpart since the mesogens cannot be treated simply as one-dimensional objects. Different approximations including the use of hard, infinitely thin plate[38-39], ellipsoids[40], and cut spheres[32] have been insightful in addressing factors that affect the formation of various mesophases and the properties of discotic liquid crystalline materials. For example, computer simulation done by Veerman and Frenkel[32] found the existence of discotic columnar phase for disks of finite thickness at high concentrations, and demonstrated the dependence of phase behavior on particle aspect ratio (diameter-to-thickness ratio) and concentration (Figure 1.3a). Polydispersity is another important parameter concerning the phase behavior in terms of the position of the transition lines as well as the type of transitions and phases formed [39,41-43], as indicated elusively in previous experimental findings[35,44].
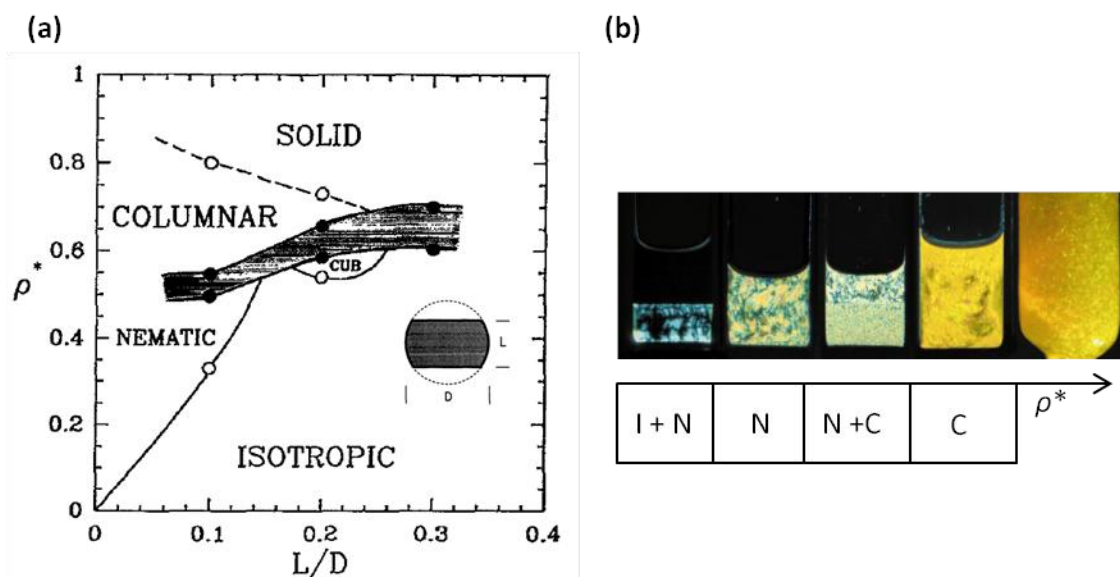
Figure 1.3. (a) Computer simulated phase diagram for cut spheres, the reduced density (ρ^*, density relative to the close-packed density) is plotted as a function of inversed aspect ratio (L/D). (b) Liquid crystals phases of Gibbsite suspensions at increasing particle concentrations (left to right). The upper panel shows polarized photograph of the suspensions in tubes to distinguish varying phases (isotropic appears dark, and the other phases birefringent). The far right sample is illuminated with white light, showing bragg refraction property of columnar phase. The lower panel demonstrates the corresponding phases.

Despite the prediction of stable nematic phase for suspensions of sufficiently anisometric platelets (disk-like particles) made by Onsagar in 1948 and the hint of liquid crystal phase observed by Langmuir[25], it was not until half a century later that this idea was collaborated experimentally by Van der Kooij and Lekkerkerker for sterically stabilized gibbsite Al(OH)$_3$ particles (Fig 1.3b)[35]. Following this irrefutable prove of thermodynamically stable phase transitions of discotic suspensions, Patrick and co-workers[45] showed the presence of isotropic-nematic transition for aqueous suspensions of natural clay Nontrinite, a system where electrostatic interactions do not hinder the formation of nematic phases. Until now, limited number of experimental systems can be

used to systematically vary parameters such as polydispersity, aspect ratio[46-48], and inter-particle interactions[49-51] to investigate how these factors influence phase behavior of suspensions of colloidal plate-like particles. Suspensions of high aspect ratio, plate-like particles exfoliated from inorganic α-Zirconium phosphate (ZrP) layered crystals were recently shown to exhibit stable nematic (N) and smectic (S) liquid crystal ordering when increasing particle volume fraction[44]. The aspect ratio of these platelets could be controlled by synthetic conditions[52] and the polydispersity tuned via separation procedures, making the ZrP suspensions a good candidate as s model system for discoitic liquid crystal studies.

1.2.5 Microfluidics

Microfludics concerns the use of miniaturized devices to precisely manipulate and handle small amount of liquids. It is an ongoing multidisciplinary field that involves chemical and biological processes miniaturization (lab-on-a-chip technology) as well as optics and information technology[53-55]. Most microfluidic devices are fabricated using standard photolithography and soft lithography on silicone, glass[56-57] or polymer[58]. The scale-down process provides obvious advantages such as low sample volume, low energy consumption, short time analysis, and high detection sensitivity. Additionally, enhanced surface phenomenon and distinct fluid characteristics such as low Reynolds number hydrodynamics comes into play as the dimensions of the channels approaches the microscale.

Controlled formation of droplet and bubble in microchannel is a unique feature in microfluidics by exploiting the laminar flow nature of the fluids. The increasing

popularity of droplet-based operations, from rapid reagent mixing, materials encapsulation, to droplet-based particle synthesis, has lead to its own microfluidic subcategory—droplet microfluidics[59]. Different from continuous flow systems, droplet microfluidics focus on using two immiscible fluids (liquid-liquid or liquid-gas) to create small, discreet volumes in a continuous phase. Conventional bulk emulsification (mixing and turbulent droplet breakup) can only yield polydisperse emulsions, whereas the bottom-up approach with microfluidics enabled precise generation of individual emulsion droplets (Figure 1.4a). High throughput formation of uniform, size controlled droplets has been demonstrated in microfluidic devices with flow focusing[60] and T-junction geometries[61]. Highly structured, monodispersed multiple emulsions have also been generated in a similar fashion using capillary microfluidic designs[62] (Figure 1.4b). Uniform single and double emulsions, in addition to their general applications as microreactors, are novel platforms for particle synthesis[63] and kinetic studies (i.e. biomacromolecule and colloidal crystallization)[64-66] as well as an excellent tool for particle interfacial assembly[67-68].
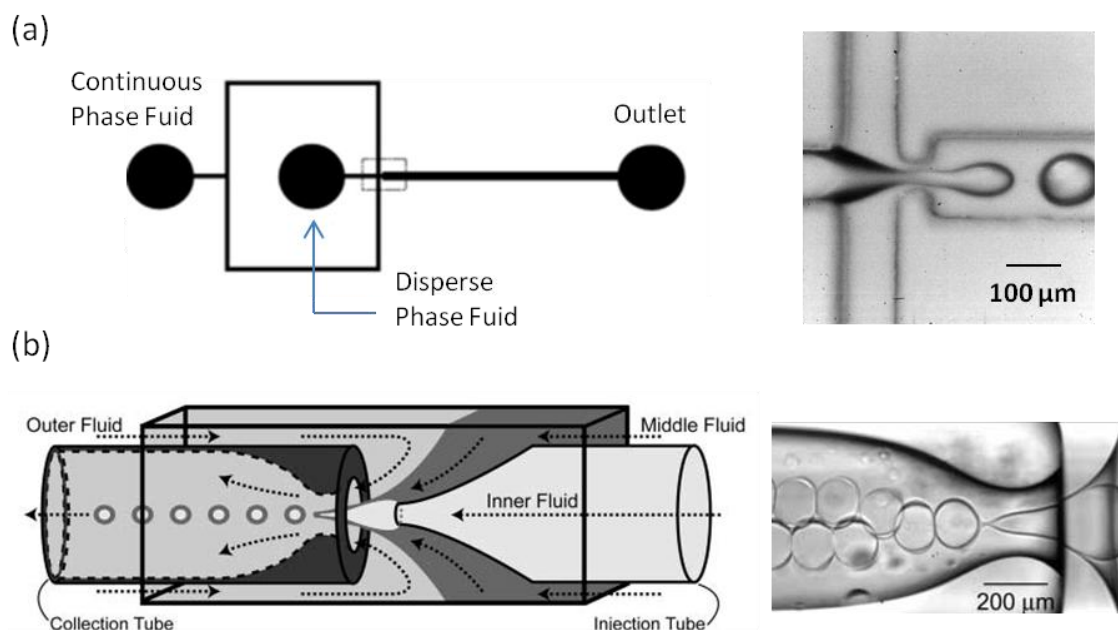
Figure 1.4. Device schematic and corresponding microscopy image for (a) (PDMS) flow focusing microfluidics and (b) glass microcapillary coaxial flow double emulsion generator[62].

1.3 Dissertation Outline

This dissertation is organized as follows. General experimental methods are outlined in Chapter II. In Chapter III a novel surface modification method and fluorescent technique has been developed to investigate the reactivity of surfaces on polymersomes as influenced by polymer architecture. Detailed explanation of the variance in reactivity for different surfaces is provided. The chapter also describes a protocol for polymersome assembly and deformation induced by depletion attraction. The focus then switches to platelet assembly and discotic particle-based liquid crystals system from Chapter IV and onwards. Fabrication of high aspect ratio plate-like particles via bulky cation exfoliation and hydrophilic polymers is discussed. Ordered phase

formation in suspensions of such particles is then compared to the general phase diagrams for discotic systems predicted from previous simulations, and the role of polydispersity is experimentally examined. Comparison of suspension stability is compared for platelets of different surface functionalizations. A fresh look on ion exchange and how it modulates inter-disk interactions to change suspension phase behavior, especially colloidal gel formation, is unveiled in Chapter V. In Chapter VI, organic-inorganic hybrid systems are created by surface modification of colloidal platelets, via chemical coupling and physical adsorption. The hydrophobicity-dependent suspension stability and platelet self-assembly is investigated. Chapter VII describes the encapsulation of colloidal platelets in emulsion droplets, a first study on discotic liquid crystal suspensions in spherical confined geometry. Controlled droplet generation by microfluidic emulsification technique enables extensive study on emulsion stability for mixed platelet/surfactant systems. Summary and conclusions of the findings of this dissertation is presented in Chapter VIII. Finally, current work and future directions not detailed in the dissertation is provided in Chapter IX.

CHAPTER II

EXPERIMENTAL METHODS

2.1 Materials and Equipments

2.1.1 Generic Chemicals

- Sucrose, sodium chloride, sodium iodide, sodium thiosulfate, phosphate butter saline, methanol, acetone, hydrogen chloride, sulfuric acid, zirconium chloride octahydrate, tetramethylammonium hydroxide, tetraethylammonium hydroxide, tetrapropylammonium hydroxide, tetrabutylammonium hydroxide (Fisher Scientific, PA)

- Chloroform, toluene, hexadecane, sodium hydroxide, tetrabuthylammonium chloride, propylamine, Sorbitane monooleate (Span 80), polyethylene glycol of molecular weight 20000 (Sigma-Aldrich)

- Polyethylene glycol (polyglykol) of molecular weight 1000, 2000, and 8000 (Clariant Corp., NC)

2.1.2 Di-block Copolymers, Lipids, and Particles

- Poly(ethylene oxide -b- butadiene) (PEO_{89}-PBd_{120}, MW 10400 g/mol; PEO_{20}-PBd_{33}, MW 1800 g/mol) copolymers (Polymer Source Inc., Canada)

- 1,2-di-(9Z-octadecenoyl)-*sn*-glycero-3-phosphocholine (DOPC) and 1,2-di-(9Z-octadecenoyl)-*sn*-glycero-3-phospho-(1'-*rac*-glycerol) (sodium salt) (DOPG) lipids (Avanti Polar Lipids, Alabaster, AL)

- Carboxylate-modified FluoSpheres® microspheres (2 μm polystyrene microspheres, red fluorescent) (Invitrogen, CA)

2.1.3 Reactive Fluorophores

- 8-amino-4-(trifluoromethyl) coumarin (Sigma-aldrich, MO)

- Nile Red, Texas Red® 1,2-dihexadecanoyl-*sn*-glycero-3-phosphoethanolamine, triethylammonium Salt (TR-DHPE) (Invitrogen)

2.1.4 Surface Functionalization Chemicals

- *N*-Ethyl-*N'*-(3-dimethyl aminopropyl) carbodiimide (EDC), and *N*-Hydroxysuccinimide (NHS) (Pierce, IL)

- 4-methoxy-2,2,6,6-tetramethyl piperidine-1-oxyl (TEMPO), sodium hypochlorite (NaOCl), sodium bicarbonate (NaHCO$_3$), and octadecyl isocyanate (Sigma-Aldrich)

- Bovine serun albumin (BSA)

- Jeffamine M-1000, ED-900, ED-2003 (Hustman)

2.1.5 Photolithography and Soft Lithography Chemicals

- SU-8 2050 (MicroChem, MA), SU-8 Developers

- Sylgard 184 polydimethylsiloxane (Dow Corning)

2.1.6 Instruments and Equipments

- QuantaMaster™ UV VIS spectrofluorometer equipped with FeliX32™ software package (PTI, Birmingham, NJ)

- Shimadzu IRAffinity-1 Fourier Transform Infrared Spectrometer in an ATR, attenuated total reflection mode with a ZnSe ATR prism (Model: PIKE MIRacle^{TM} A) (Columbia, MD)

- Parr-Physica MCR-300 rheometer

- D8 Advanced Bragg-Brentano X-ray Powder Diffractometer (Bruker Instrument)

- Zetasizer Nano ZS90 dynamic light scattering (DLS) (Malvern)

- Axiovert 200M inverted microscope equipped with Zeiss AxioCam MRm camera (Zeiss, Germany)

- Eclipse TE2000-U inverted microscope (Nikon)

- Leica TCS SP5 confocal microscope (Bannockburn, IL)

- JEOL JSM-7500F scanning electron microscope (JEOL, Ltd., MA)

- Phantom V4.2 fast camera equipped with Cine controller software (Vision Research, Wayne, N.J.)

- Q4000 mask aligner (Quintel); SCS P6204 spin coater; reactive ion etcher (March Plasma Systems, CS-1701); pH and hand-held conductivity/°C meter (Oakton® Acron series CON6); Osmometer model 3320 (Advanced Instruments, Inc., Norwood MA)

2.1.7 Miscellaneous

- Vacuum grease (Dow Corning)

- Syringe pump (Havard Apparatus)

- MiniExtruder (Avanti Polar Lipids)

2.2 General Procedures

2.2.1 Fluorescent Labeling

Fluorescent labeling of PEO-b-PBD di-block copolymer used in Chapter III were achieved by modification of the ethylene oxide block following the protocol of Kinnibrugh[69] in a two-step procedure as the following. First, the ethylene oxide end was converted into carboxylic acid. The end-carboxylated block copolymer was made via a two-phase oxidation reaction. An organic phase (dichloromethane as solvent) containing block copolymers (as received) were mixed and stirred in with an aqueous phase containing a regenerating agent NaOCl buffered with $NaHCO_3$ at pH 8.6 to form an emulsion. The oxidizing agent TEMPO (dissolved in dichloromethane) was added in separate doses every 3-5 min. After all reagents were added and reacted, the pH of the mixture was adjusted to ≥ 11 with 3 N NaOH to break down the emulsion. Then the organic phase was separated from the mixture and dried in a vacuum oven, obtaining carboxylated block copolymers. Once the carboxylated block copolymers were made, a second labeling reaction could be done using a modified EDC/NHS peptide linkage reaction. The oxidized block copolymers were prepared in chloroform. EDC (dissolved in chloroform) and NHS (dissolved in THF) in ten-fold excess were then added and allowed to activate for 15 min at room temperature. An excess of amine-containing dye (in chloroform) was then added to the reaction flask and allowed to react for 2 h. Extra doses of EDC and NHS were added every 2 h to increase linking efficiency. Finally, the unreacted products were separated using dialysis tubing (MWCO 8000 Da) against $CHCl_3$ and the product was dried in a vacuum oven.

Labeling of carboxylate-modified microspheres followed the standard EDC/NHS peptide linkage procedure in aqueous at room temperature, similar to the second labeling procedure for the block copolymer modification. Twenty microliters of a 1 wt% microspheres (surface charges 0.1 ~ 2.0 milliequivalents/g as specified by manufacturer) suspension were added to a 1mL solution containing EDC and NHS (ten-fold excess based on the maximum number of carboxylate groups possible, buffered to pH 6). The mixture was stirred and incubated for 15 min to form a semi-stable NHS-ester, after which the fluorophore prepared in 0.15 M PBS buffer (pH 7.13) was added, pH adjusted to 7.3 (with dilute NaOH), and allowed to react for an additional 2 h. A second dose of EDC/NHS was added and reacted for another 2 h for complete labeling. This was followed by centrifugation of the reaction mixture to remove unreacted products, and the supernatant was replaced with DI. Several additional washes were made to ensure purity of the particle sample.

2.2.2 Functional Vesicle Formation

Giant polymer vesicles were prepared via thin film rehydration method, where the di-block copolymer was diluted with aqueous into the lamellar phase (Figure). First, an appropriate amount of di-block copolymers (in Chloroform) were mixed in a glass vial or small scintillation vial. The solvent was evaporated and the polymer mixture desiccated under vacuum for a minimum of 8 h. The polymer film was then reconstituted in ~320 mOsm/kg sucrose solution by heating at 60 °C for 24 h. For higher concentration samples (> 0.5 mg/mL), stirring was applied after heating for 18 h to

gently agitate vesicles from the surface of the film. Vesicle dispersions were kept at 4°C

to increase long-term stability.
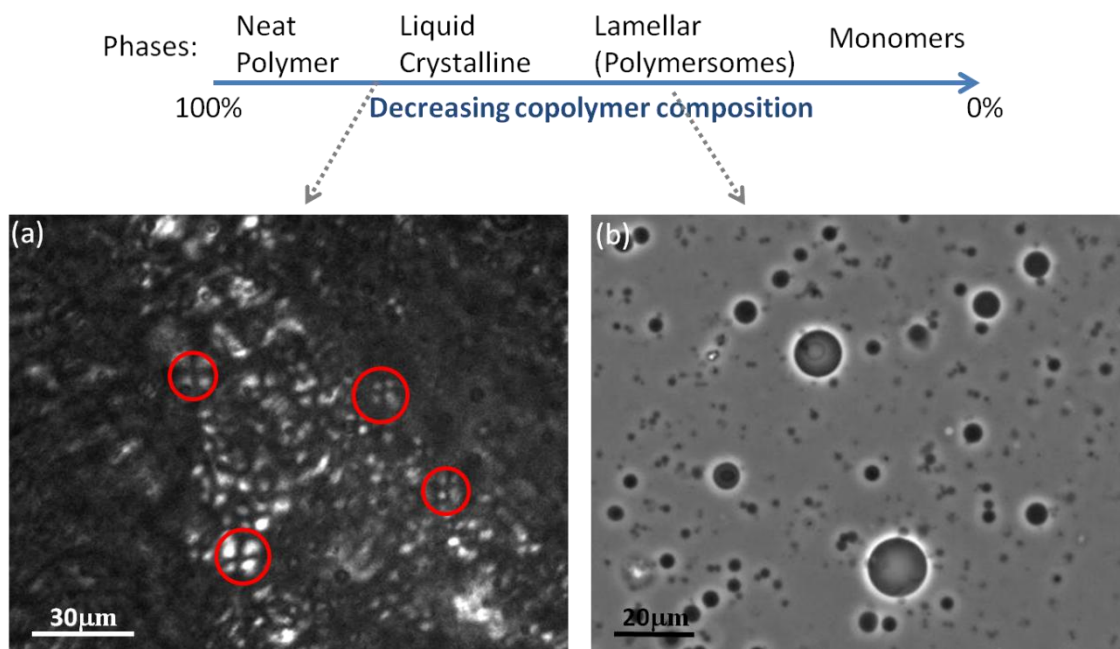
Figure 2.1. Phase diagram of di-block copolymers upon dilution. (a) Polarized micrograph of swollen copolymer film, showing liquid crystalline textures (maltese crosses circulated with red circles). (b) Phase contrast image of polymersome suspension, interior of the membrane is sucrose and the exterior is salt solution.

2.2.3 Fluorescence Quenching

Fluorescent properties were used as a probe to quantify reaction dynamics in Chapter III. Sample solutions containing coumarin dye were placed in a 1-cm path length plastic cuvette, and sample excitation was achieved by a xenon arc lamp at 375 nm, with 5 nm slit width. The steady-state fluorescence spectrum was recorded from 400 nm to 650 nm, with 1 nm step size, 0.5 s integration time, and averaged over 3

measurements. Fluorescence lifetime measurements were obtained using the same PTI instrument with a 375 nm LED light source attachment and a PMT detector at 490 nm.

Fluorescence quenching is a process in which fluorescence emission intensity decreases in the presence of a quencher. This is most commonly due to the collision between quencher molecules and an excited fluorophores, and depopulates "active" excited fluorophores, which would regularly have relaxed back to the ground state through emission of photons. The intensity decrease (for a fix fluorophore concentration) at increasing quencher concentration is describe generally with a linear Stern-Volmer relation[70]

$$\frac{I_0}{I} = 1 + k_q \tau_0 [Q] = 1 + K_{SV}[Q] \tag{2.1}$$

Where I and I_0 are the fluorescence intensities in the presence and absence of the quencher at a concentration [Q], I_0 is the lifetime of the fluorophore without a quencher, k_q is a quenching rate constant and K_{sv} is the quenching constant.

Estimation of the rate constant of the quenching reaction in non-ideal cases was made by applying the finite sink approximation, a non-linear Stern-Volmer plot used to account for deviations from linear relationship. In brief, the finite sink approximation incorporates a description of quenching rate constants based on Smoluchowski and Collins and Kimball (SCK) solution flux equation.[71] Integration of the time-independent flux equation for biomolecular quenching yields

$$\frac{1}{k_q} = \frac{1 - (R/r_0)}{k_d} + \frac{1}{k_a} \tag{2.2}$$

Where k_a is the activation energy controlled rate constant describing the reaction of encountered pairs at a reactive distance R, and k_d is the diffusion-limited reaction rate that is directly related to the diffusion coefficient D by $k_d = 4\pi N_{AV}DR$, where N_{AV} is Avogadro's number. Since an excited fluorophore is most susceptible to quenching by its nearest neighbor at some initial average separation r_0, only the first encounter is of interest in the case of efficient fluorescence quenching. The diffusive region of interest for a first encounter is $R \leq r \leq r_0$ and contributions from all subsequent encounters in the range $r_0 \leq r \leq \infty$ are eliminated. The upper limit of this boundary is defined as the sink radius r_0, the most probable initial average separation $(2\pi N_{AV}[Q])^{1/3}$, yielding the following.

$$K_{SV}^{-1} = \left(K_{SV}^0\right)^{-1} - \frac{(2\pi N)^{1/3}}{4\pi ND\tau_0}[Q]^{1/3} \tag{2.3}$$

The parameter K_{SV} is calculated from experimental data using Eq. 2.1, yielding $((I/I_0)-1)/[Q]$. The value of K_{SV}^0 ($= \tau_0 k_d = \tau_0 4\pi N_{AV}DR$ for a diffusion-limited reaction) is given by the intercept of plot K_{SV} against $[Q]^{1/3}$, and the diffusion coefficient can be obtained from the slope. Relative magnitudes of diffusion coefficients with the same quencher-fluorophore pair in different solvent environments can also be determined by comparing K_{SV}^0 values.

Halide ions are known to quench coumarin fluorescence through a photoinduced electron transfer (ET) mechanism[72-74]. Amino-coumarins are polarity sensitive dyes[75] susceptible to quenching by halides and some aromatic amines[74,76-77]. The lack of a twisted intramolecular charge transfer (TICT) state ensures a viscosity independent

fluorescence lifetime[75] so fluorescence intensity measurements are sufficient. A stock solution of quenchers was prepared at around 0.16 M, and less than 3×10^{-4} M $Na_2S_2O_3$ was added to prevent I_3 formation. Different amounts of quencher solution were added to series of samples to construct the quenching plot. Ionic strength was maintained constant throught various samples by mix-and-matching with NaCl (no noticeable quenching occurs when using other halide ions). Fluorophore concentrations in all samples were maintained below 0.5 µM to avoid inner-filter effects.

2.2.4 Pristine α-ZrP Particle Synthesis and Exfoliation

The zirconium phosphate (α-ZrP) particles used in Chapter III to VII were synthesized using hydrothermal method[52] to grow high crystallinity pristine particles. A solution containing 6.0 g $ZrOCl_2 \cdot 8H2O$ was mixed with 60mL 12M H_3PO_4 by pre-dissolving the zirconium salt in water, and adding it drop wise into a 15M acid solution under constant stirring. The mixture was then homogenized under 2 h of constant stirring at room temperature. The further crystal growth process was achieved by charging the mixture into a Teflon-lined autoclave reactor and heated for 24 h at 200°C. After the reaction, the products were washed with DI and collected by centrifugation. The pellets were dried at 65 °C for 24 h, and ground with mortar and pestle to a fine α-ZrP powder. This yields layered particles, with size of around one micron (Figure 2a). The particle size and thickness can be readily controlled by changing the acid concentration and reaction time.

Monolayered platelets were prepared via (bulky) cation intercalation and exfoliation (Figure 2b). Equal molar ratio of α-ZrP and exfoliating agents (quaternary

ammonium hydroxides, amines) were combined in aqueous and subjected to sonication for 30 min. The suspension was allowed to react over 48 h (suspension pH stabilizes) for complete exfoliation. Purification was carried out via centrifugation and re-dilution with DI for 2~3 times when needed. The platelet suspensions were stored at room temperature. Exact weight percentage of solids in the suspensions were determined by drying a known amount of sample in the oven.
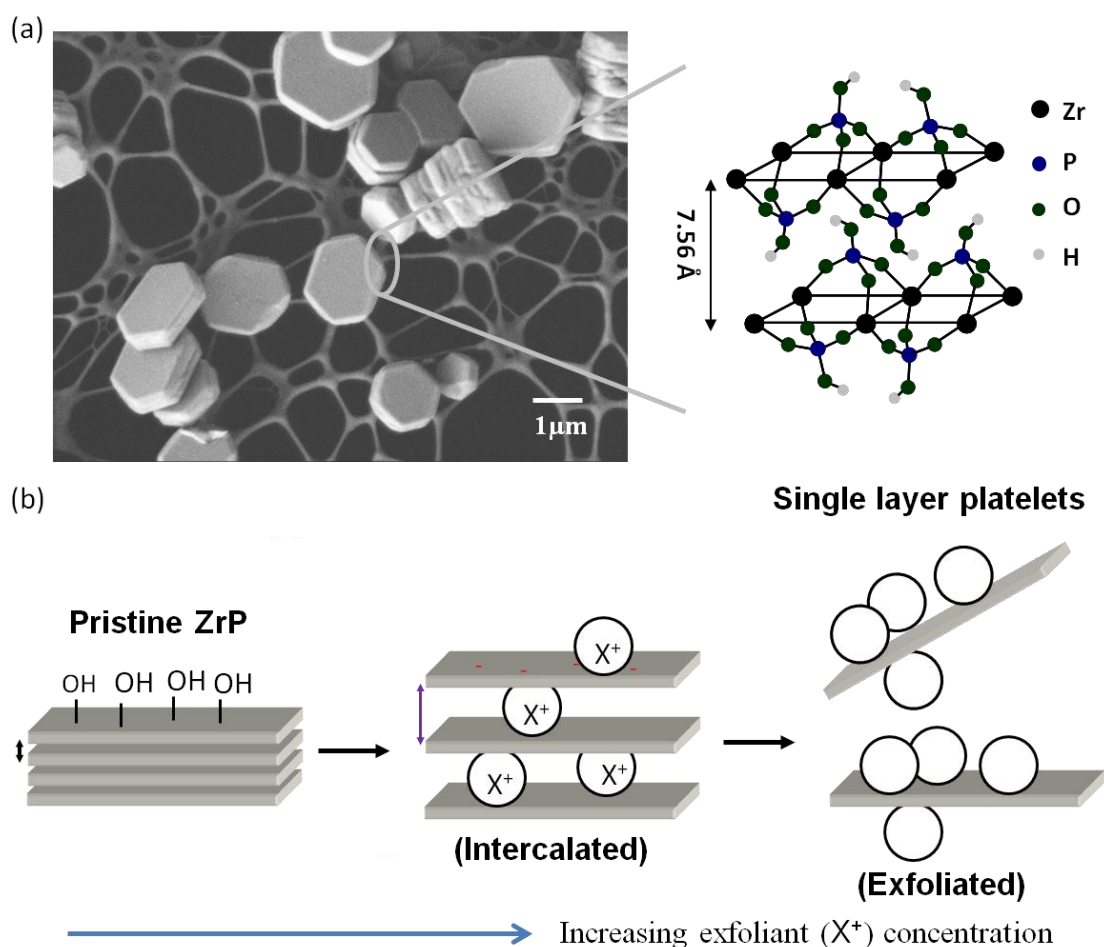
Figure 2.2. (a) SEM image of pristine α-ZrP on carbon grid. On the right is the crystal structure. (b) Schematic of chemical exfoliation process for layered crystalline materials.

2.2.5 Chemical Modification of ZrP Monolayer Platelets

As the high crystallinity and small interlayer spacing prevent long chain molecule from entering the inter-layer galleria directly, an alternative approach is required to make all POH groups accessible to reaction. An exfoliation-deintercalation method[78-79] was adapted to functionalize ZrP on both sides of the layers. First, a colloidal suspension of exfoliated ZrP was made by mixing propylamine with pristine particles, as described in previous section. Then, the suspension was treated with 0.1M HCl (to pH < 2.0) to regenerate the protons on ZrP. The suspension would now have a gel-like consistency. Afterwards, the particles were separated from the exfoliant and excess chloride ions by washing and centrifugation in DI for 4 times. Solvent displacement was preceded by washing the particles with acetone 3 times, followed by 2 washes in dry acetone and 3 times in dry toluene or octadecane. Sonication was performed after each solvent exchange to avoid aggregation. Once dispersed in an organic solvent, the dispersion was transferred in a three-necked round-bottomed flask equipped with a reflux condenser and kept under nitrogen atmosphere. An excess of n-octadecyl isocyante in comparison with the POH groups available at the surface of the ZrP platelets was added slowly (drop by drop) as the temperature reaches 80°C. The temperature was then increased (to around 10~20°C lower than the boiling point of the solvent) and kept for 6~8 hours. The modified particles were washed with toluene and ethanol to remove any by-products and unreacted octadecyl isocyantes.

2.2.6 Particle Sizing

Particle sizes were measured by dynamic light scattering. A monochromatic laser light was passed through a diluted colloidal suspension and the time-dependent scattering intensity fluctuation was monitored at a 90-degree angle from the incident beam. Typically, the hydrodynamic radius (R_h) of the particles is determined via Stokes-Einstein relation $R_h = k_BT/(6\pi\eta D)$ as the diffusion coefficient (D) be extracted from the auto-correlation functions generated by intensity versus time data. Here, k_B is the Boltzmann's constant and η is the viscosity of the solvent. The Stokes-relation for platelets with thickness t, diameter $2R_p$, and aspect ratio $\delta = 2R_p /t$ is approximated by that obtained for oblate ellipsoids[80-81]

$$t = \frac{k_BT}{3\pi\eta D} \frac{\arctan\left(\sqrt{\delta^2 - 1}\right)}{\sqrt{\delta^2 - 1}} \tag{2.4}$$

By setting the diffusion coefficients equivalent to that obtained for spheres, one can convert the size R_h calculated by the instrument software package to the aspect ratio (thickness pre-determined through literature and atomic force microscopy) of disk-shaped particles.

For non-exfoliated particles, SEM was used to determine particle size distributions. SEM images were analyzed using ImageJ, where the area A of each disk was measured. Size of the disks was reported as the calculated diameter $D_p = 2 (A/\pi)^{1/2}$, which represent circle diameter with an equivalent total area.

2.2.7 X-ray Diffraction (XRD) Analysis

For solid α-ZrP powders, the sample was gently packed on a quartz sample holder for XRD characterization. For the intercalated and exfoliated ZrP, the sample was cast onto the holder and dried in the oven overnight prior to characterization. Raw data collected from $2\theta = 5°$ or above were presented as collected without background subtraction; for lower angels (minimum attainable angle $2\theta = 2°$) cases, background subtraction was performed with standard XRD data processing software. The peak positions (2-theta) were converted to distance d (Å) according to Bragg's law relationship.

$$n\lambda = 2d \sin \theta \tag{2.5}$$

Where n is an integral number, and the wavelength λ is 1.54 Å for copper target.

2.3 Microfabrication and Soft Lithography

The microfluidic devices used for droplet generation is Chapter VII were fabricated by standard soft lithograph[82] using a silicon wafer mold. Conventional photolithographic techniques were used to create microfluidic patterns, and all microfabricaiton procedures were conducted in the cleanroom. Figure 2.3 outlines the steps carried out in the procedure. First, a thin layer (~75 µm) of SU-8 2050 photoresist was spin coated onto a clean silicon wafer preheated at 120°C. The photoresist was soft baked on a hot plate at 65 °C and 95 °C, and then exposed to UV-radiation for 40 s through a patterned mask with the microchannel geometry. The photoresist was post-baked at 95 °C and 115 °C prior to immersion in the developer solution (for 5 min). The

non-irradiated photoresist, now soluble, was removed with gentle agitation, and rinsing with isopropyl alcohol, leaving the microfluidic patterns on the silicon wafer.

Once the master molds were made, a ratio of prepolymer/curing agent (Sylgard 184) were prepared and degassed in a vacuum to remove air bubbles generated during mixing. The mixture was then poured onto the wafer mold containing the microfluidic channels in positive relief, and put back into the vacuum chamber to remove the remaining air pockets. The PDMS elastomer was cured in the oven at a 60 °C overnight. The PDMS layer was then cut off and peeled away from the molds. Interconnection holes were punched with an end-sharpened blunt needle, and cleaned with isopropanol prior to bonding. PDMS mixture was prepared in the same way as mentioned previously, spin coated onto a glass slide, and cured for 15~20 min at 60 °C. The ready-cured PDMS slab was sealed onto the glass slide with the thin layer of partially cured PDMS film, and finished curing in the oven for another 4 h. An alternative method was used to adhere PDMS to glass via oxygen plasma etching. The PDMS slab and a glass slide were placed together in the RIE chamber and exposed to oxygen plasma for 30s at 25W at an O_2 flow rate of 4 cm^3/min. Silanol groups were exposed on both PDMS and glass surface after the treatment, forming irreversible, covalent bonding between the PDMS and the glass substrate at the two were pressed together.
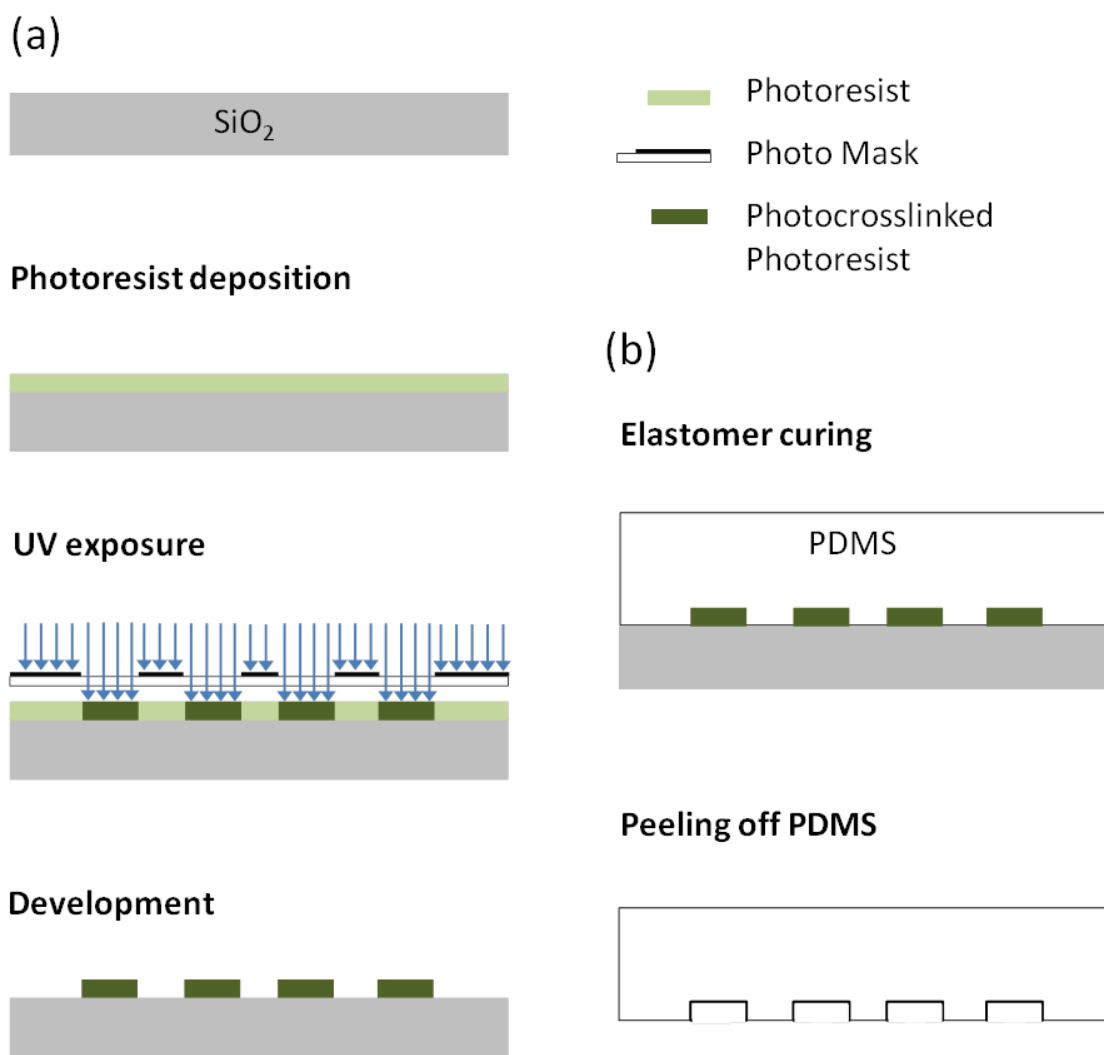
Figure 2. 3. Schematics for (a) fabrication of reusable wafer mold via photolithography processes, and (b) soft lithography (replica molding) for microfluidic channels.

2.4 Microscopy and Polarized Photography

2.4.1 Microscopy Imaging

Sample cells to contain vesicle dispersions for imaging were constructed with two Teflon strips sandwiched between a cover glass and a glass slide, and sealed with vacuum grease. Typically, 20 μL of vesicle dispersion (~120 μL/mL formed in sucrose)

was diluted into 150 µL iso-osmotic pressure PBS solution, and allowed to settle for 5 min before images were taken. Bright field and phase contrast images were acquired with a 20X, 40X, or 63X oil immersion objective using Carl Zeiss Axiovert 200M inverted microscope equipped with a Zeiss AxioCam MRm camera. Fluorescent images were taken with the same setup, with sample illumination provided with a mercury arc lamp and appropriate filter sets.

Confocal scanning laser microscopy (CSLM) is a slight variation of the above-mentioned fluorescence data collection. As the light is collected through a small pinhole, out-of-focus light is blocked and noises are significantly reduced, hence high spatial resolution can be achieved. CSLM was performed on fluorescently labeled vesicles sample to clearly observe the features of membrane deformation under strong attraction forces. It was also performed on emulsion systems where the continuous phase was fluorescently dyed. 3-dimensional scans provided evidence of fluorophore compartmentalization and identified single and double emulsions present in the dispersion.

Liquid crystal textures of the discotic suspensions were identified with polarized microscopy using a Nikon Eclipse TE2000-U inverted microscope equipped with a colored camera. In general, a drop of suspension was placed onto a microscope slide and covered with a cover glass for day-to-day imaging. The other preparation method was preferred when precise control over sample thickness and sample storage was desired. In this scenario, the suspensions were loaded into Vitrotube W3520-050 (VitroCom, NJ), a

50 mm long rectangular capillary of 0.2×4.0 mm inner dimensions, and sealed with capillary wax.

2.4.2 Polarized Photography

House-made polarize photography set up was used to study the phase behavior of discotic suspensions. Plastic polarizing films were placed in the front and back of the sample in perpendicular polarized direction. Sample illumination from the back side of the sample was provided by a fluorescent lamp, and a layer of tissue paper was used as diffuser. Digital photographs were taken with a Sony DSC-W220 digital camera at low exposure time setting. All images were processed and analyzed with ImageJ software (NIH).

CHAPTER III

TUNING POLYMERSOME REACTIVITY BY

SURFACE STRUCTURE*

3.1 Synopsis

Understanding how the surface interactions (reaction, binding, etc.) are governed by the bilayer structure is critical to enable construction of polymersomes with tailored colloidal behavior. Incorporating coumarin functionalized copolymers into the vesicular structure enables us to probe the effect of PEG brush and surface architecture on the bimolecular quenching reaction occurring at the polymersome surface. The role of vesicle bilayer architecture (copolymer composition, chain length, local concentration surrounding the active site) was revealed through comparison of quenching in free solution, on bare particles, and on two types of vesicle surfaces—one where the functionalized copolymer groups are longer than the surrounding unfunctionalized copolymer, and one where both functionalized and unfunctionalized groups are the same length. The surface reaction appears to be dominated by quencher diffusion, a conclusion supported by conductivity measurements and ion partition studies indicating that these effects arise as a consequence of retarded ion mobility in the presence of the PEG brush. The study of the interplay between the vesicle bilayer architecture and the surface reaction rate provides useful insights that can help guide the design of polymer-

_____

somes with desired functional properties. In addition, polymersome membrane elasticity and its susceptibility to deformation were showcased in this Chapter as well.

3.2 Introduction

Synthetic block copolymer amphiphiles, analogs to natural phospholipids, can self-assemble into enclosed bilayer structures similar to cell membranes.[83-85] These polymeric vesicles (polymersomes) share many features in common with lipid vesicles such as a spherical enclosed structure capable of entrapping hydrophilic components in the interior aqueous region, but they also offer unique advantages including increased stability, and resistance to thermal and mechanical stresses. This makes them superior to conventional phospholipid vesicles. Additionally, many of these properties (membrane bending modulus, rigidity, toughness, etc.) are widely tunable by varying block length or chemical structure.[17,86]

3.2.1 Aggregation of Vesicles

Macromolecule-induced cell aggregation is of fundamental and clinical interest as it has been suggested to be the mechanism for rouleaux formation[87-88] as well as cell organizations.[89] This distinct interaction (from the more regularly known van der Waals, hydrophobic, and ionic interactions), called depletion attraction, is a non-specific interaction that occurs in crowded polymer or protein solutions. Inert agents like polyethylene glycol (PEG) or dextran have been used extensively to promote cell aggregation/fusion. PEG-mediated lipid bilayer fusion mimics protein-mediated biomembrane processes,[90] and has provided a useful model in the study of membrane biophysics.[91] Vesicle-vesicle adhesion, which strength can be modulated by polymer

concentrations,[92-93] is often accompanied by membrane deformation and vesicle destabilization in the case of strong adhesion. Membrane mechanics, in particular the "flexibility" or "stiffness" of vesicle bilayers, which is described quantitatively with bending modulus, plays an important role in vesicle adhesion and deformation[94-95]. Synthetic vesicles, whose range of bending modulus are substantially wider than that of liposomes (over an order of magnitude),[86] expand the range of system over which can be studied, and has recently been used to re-evaluate the effect of bending on adhesion via dual micropipette technique.[96]

Being the simplest model of cells with enhanced mechanical properties, polymeric vesicles were employed here in the formation of bulk aggregates brought together by attraction forces. The cluster geometries were documented at two adhesion strengths and classified with the general structure and number of vesicles in each cluster. The results could elucidate some structural aspect of vesicular aggregates not discovered with lipid-based vesicle systems.

3.2.2 Polymersome Surface Structure-Governed Interactions

The ability to construct polymersomes with tailored properties critically depends on understanding how the kinetics of surface interactions (reaction, binding, etc.) are governed by the bilayer architecture. Previous efforts to probe these interactions have focused mainly on adhesion-based measurements. Surface force apparatus experiments, for example, have been employed to examine receptor-ligand interactions between a supported lipid bilayer incorporating anchored biotinylated PEG chains of varying length and a streptavidin functionalized surface.[97-98] These studies provided precise

measurement of specific and nonspecific forces between the PEG-anchored ligands and model receptor surfaces that were in good agreement with theoretical predictions and simulations.[18,99] But this method is restricted to planar systems, making it challenging to adapt for study of vesicular structures like polymersomes.

Micropipette aspiration is another widely used technique that has been adapted to study adhesion in bilayer membranes such as red blood cells and liposome membranes.[92,100-101] A further variation of the method, micropipette peeling tests, has been applied to assess adhesion strength between biotin-functionalized polymersomes and avidin-coated beads.[16-17] These experiments were instrumental in identifying how surface adhesion depends not only on the bond strength, but also on how the ligand is presented on the polymer brush surface. But despite their simplicity, adhesion-based measurements primarily describe equilibrium interfacial interactions and provide little information about the reaction itself.

Fluorescence-based spectroscopic methods enable interactions and dynamic events involving probe carrying molecules to be quantitatively measured with a high level of sensitivity. Fluorescence quenching is frequently used in biophysics to probe conformational changes, detect binding events, characterize membrane fluidity and permeability,[102] and to elucidate the location of fluorescently tagged molecules inside the bilayer.[70] Here, we adapt the fluorescence quenching technique to probe small molecule reaction kinetics on polymersome surfaces.

We report the results of quenching studies performed to track reactions in the bulk solution, on bare particles, and on polymersome surfaces. Vesicles were

constructed using poly(butadiene-b-ethylene oxide) (PEO-b-PBd) copolymer with two different lengths (PEO_{89}-PBd_{120} and PEO_{20}-PBd_{33}). The long copolymer was end functionalized with coumarin and mixed with unfunctionalized copolymer to create labeled vesicles. We find that quenching is greatly reduced in the presence of PEG, and that the polymersome surface in which the functionalized chains are the same length as the membrane brush displays a lower quenching rate then when these chains are surrounded by shorter brushes (Figure 3.1). Further experiments suggest that these observations can be explained by retarded ion mobility in the presence of the PEG polymer rather than ion exclusion effects. Reaction rates are quantified using a nonlinear Stern-Volmer analysis based on the finite sink approximation,[71,103] and a modified Yasuda free volume model is used to describe ion diffusion.[104] This analysis allows us to identify correlations between the quenching rate and ion diffusivity so that the local polymer concentration surrounding the fluorophore can be inferred. In this way, we are able to establish a relationship between the reaction rate and the bilayer surface structure, thereby providing a useful tool to understand how surface reactions can be manipulated by modifying the polymer vesicle formulation.

$EO_{89}Bd_{120}/COU\text{-}EO_{88}Bd_{120}$ $EO_{20}Bd_{33}/COU\text{-}EO_{88}Bd_{120}$
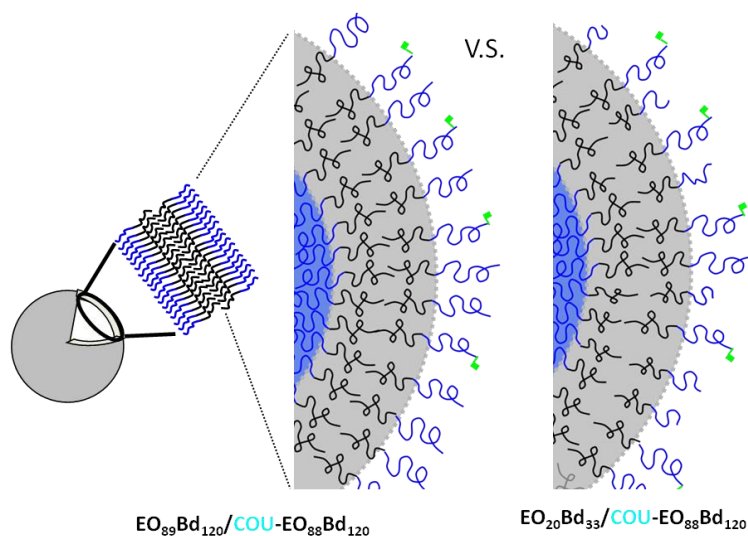
Figure 3.1. Schematic illustration of the two polymersome surface structures created by mixing functional/non-functional di-block copolymers of the same and different length.

3.3 Theory and Experimental Methods

3.3.1 Depletion Attraction Induced by Non-adsorbing Polymer

It is known that increased concentrations of proteins lead to cellular aggregations, and flocculation of colloidal suspensions occurs when a non-adsorbing polymer was added. The common theme of these two phenomenon is depletion interaction, an attractive force between two bodies due to the presence of depletion layer (with a characteristic size equivalent to that of the depletant) near the surfaces. Figure 3.2 depicts two colloids interaction in a solution of non-adsorbing polymers, the so-called depletants represented as smaller spheres. Upon overlapping of the depletion layers, minimization of the distance between two surfaces maximized the total volume available for the polymer chain, minimizing the free energy of the polymers. Exclusion of the depletants from the gaps creates a concentration gradient of the smaller

component (polymers) from the outside of the spheres. The generated osmotic pressure

acts effectively as an attractive force between the two surfaces.
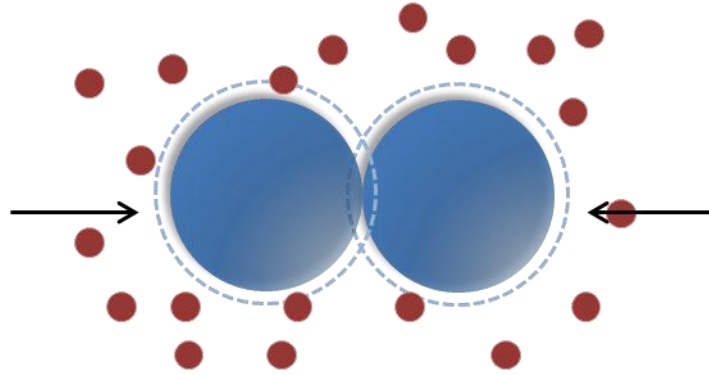
Figure 3.2. Schematic of cluster formation via depletion attraction in a mixture of colloids (blue spheres) and macromolecules (represented with red spheres). The depletion layer is indicated as the area within the dashed lines around the colloids; its thickness is equivalent to the radius of gyration of the polymers.

Theoretical description of the depletion potential was offered by Asakura and Oosawa (the Asakura-Oosawa; AO molel).[20] The depletion potential is written in general as a product of the (ideal) bulk osmotic pressure $P = n_b k_B T$ (n_b bulk number density of the depletant) and the overlap volume V(h). For two spheres of radius R, depletant radius a, the particle-particle AO potential is given as[105]

$$W(h) = \infty, \; h < 0 \tag{3.1a}$$

$$W(h) = -PV(h), \; 0 \leq h \leq 2a \tag{3.1b}$$

$$W(h) = 0, \; h \geq 2a \tag{3.1c}$$

with overlap volume of

$$V(h) = \frac{3\pi}{4}(R+a)^3 \left(1 - \frac{3(h+2R)}{4(R+a)} + \frac{(h+2R)^3}{16(R+a)^3}\right)$$ (3.2)

From the expression described of equation and, range of the attraction is determined by the size the depletant, and the depth of the attraction well, i.e., strength of the attractive force increases with the bulk osmotic pressure, hence the concentration of the depletant.

Sample cell for depletion aggregation experiments were constructed by sealing a 1/4" thickness rubber square (~3/4" length) with a 1/2" diameter hole in the middle on top of BSA (bovine serum albumin) coated cover glass. The pretreatment was employed to prevent vesicles from sticking strongly to the glass surface once settled. Polyethylene gloycol was used as depletant. Vesicles suspensions (0.25mg/mL) prepared in sucrose solution were diluted into the well filled with equal-osmotic pressure PBS buffer, and the vesicles were allowed to settle for a few minutes before a drop of concentrated PEG solution was added.

3.3.2 Quantifying Reactivity on Polymersome Surfaces

Polymer vesicles incorporation courmain-labeled di-block copolymers were formed according to the general procedures described in section 2.2.1 and 2.2.2. Functionalization was performed on the longer polymer (PEO_{89}-PBd_{120}), and 10 wt% of the labeled polymer (Cou-EO_{88}-Bd_{120}) was then mixed with either PEO_{89}-PBd_{120} or PEO_{20}-PBd_{33}. Fluorescence characterization and preparation of coumarin solutions, particle and vesicle suspensions was carried out as outlined in section 2.2.3. Extraction of quenching rates was preceded using the finite sink approximation. By rearranging Eq.

2.3, and defining $f = k_a/(k_d + k_a)$, a modified nonlinear Stern-Volmer plot can be constructed from

$$\frac{I_0}{I} = 1 + \frac{f\tau_0 (4\pi NDR)[Q]}{1 - f(2\pi N)^{\frac{1}{3}} R[Q]^{\frac{1}{3}}}$$ (3.3)

For a diffusion limited reaction ($k_a \gg k_d$), the value of f goes to unity. The quenching rates determined by Eq. 3.3 will be denoted as K_q.

Ion partition experiments were conducted by first compartmenting PEG and salt solutions with a dialysis membrane that allows only small molecules to pass through. PEG solutions (MW 2000) of 15.5 and 50 wt% are placed inside a CE dialysis tubing (MWCO 1000 Da) and dialyzed against KCl salt solutions in an 8.2 x 16.5 cm Ziploc® bag for at least 24 h. The volume ratios of PEG versus salt solution were 1:3 and 1:6 respectively. After the freely moving salt partitioned inside and outside of the tubing reached equilibrium, the concentration of the exterior solution was measured by solution conductivity calibrated by measurements of KCl solutions in the range of 0~10 mM. Bulk visocity measurements were made with cone-and-plate fixture on the MCR rheometer (50 mm cone diameter, data are an average of 10 measurements over shear rates ranging from $20 - 300 \text{ s}^{-1}$).

3.4 Polymersome Assembly via Polymer Depletants

Figure 3.3 illustrates typical depletion-induced adhesion process between two vesicles in PEG solution in time sequence. Initially the vesicles were separated at some minimal distance from each other. The depletion attraction, caused by the addition of non-adsorbing polymer, drives the neighboring vesicles into contact. Note that the force

is relatively short ranged, thus only those vesicles pairs with an initial separation distance smaller than a few microns would aggregate. Unlike rigid spheres, vesicles in suspension can undergo change in volume. Once adhered, vesicles can thus develop flat contact zones, which results in enhanced adhesion energies as compared to rigid, non-deformable vesicles.[106] Due to imbalance in osmotic pressure between the interior of the vesicle and the bulk (addition of PEG solute), water was expelled from the vesicle (total volume change around 50%), as accompanied by progressive vesicle deformation and expansion of the contact region. Under such large adhesion strength and deformation, the bound vesicles remain stable in the form of clusters with individual compartments.
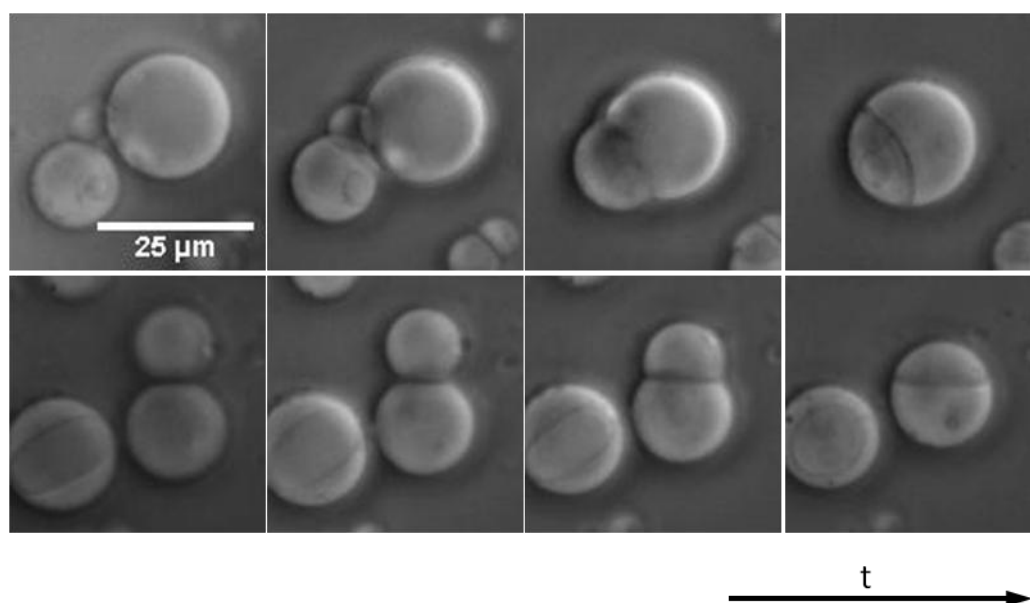
Figure 3.3. Phase contrast images of the polymersome aggregation processes following two pairs of vesicles.

To illustrate in more detail the membrane shape transformation during the adhesion process, 1% Nile Red (fluorescent dye) was incorporated into the

hydrophobilic region of the vesicles for confocal laser imaging. Images in Figure 3.4 demonstrate the rapid deformation of adhering vesicle triplets: within a few seconds within initial contact, the middle vesicle (spherical prior to contact) has transformed from a cut sphere to almond-shape to what appears like a half-moon. The shape remains constant after around 30 s from the first frame. A shape "relaxation" was observed during the process in between 26 ~ 30 s, where the projected area increased by 3.9 % (area at 26 s: 1186 μm^2; 30 s: 1232 μm^2). From the intensity profile through the adhesion plaque in the vesicle triplets, the presence of two bilayers in the contact region was clearly demonstrated.
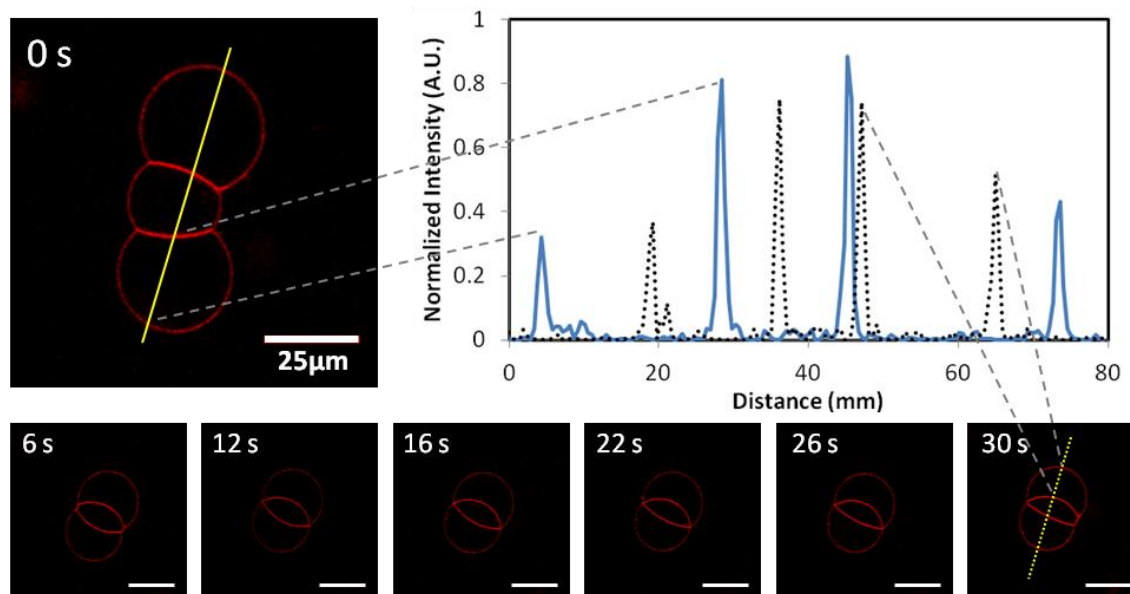
Figure 3.4. CLSM images of adhering vesicle triplets undergoing shape transition. Upper right graph is the fluorescence intensity profile across the region of interest (lines) in the upper right (solid line) and lower right (dashed line) images. Scale bars: 25 μm.

Figure 3.5 summaries some simple cluster geometries obtained at two PEG concentrations. The comparison shows how the depletant concentration changes the equilibrium morphology of the clusters via osmotic compression (images were taken ~ 10 min after the addition of depletants). At higher depletant concentration, i.e., higher adhesion strength (Eq. 3.2) and higher osmotic pressure gradient (higher bulk polymer solute concentration) over the vesicle bilayer, deformation and the total change in internal volume was more significant. Note the highly curved contact zone in a lot of the clusters at high PEG concentration, reminiscent of sigmoidally curved contacts between aggregates of erythrocyte. The role of membrane properties on the formation of these highly curved contacts geometries is unclear as comparison with theoretical models[107-108] is challenging due to 1) the total volume reduction was not controlled and difficult to track, 2) the polymersome samples are fairly polydisperse, and 3) the intrinsic difference between polymeric and lipid vesicles could have an effect on the governing parameter and the modeling approach.

	PEG 8000 17%	PEG 8000 25%
Doublets		
Triplets I		
Triplets II		
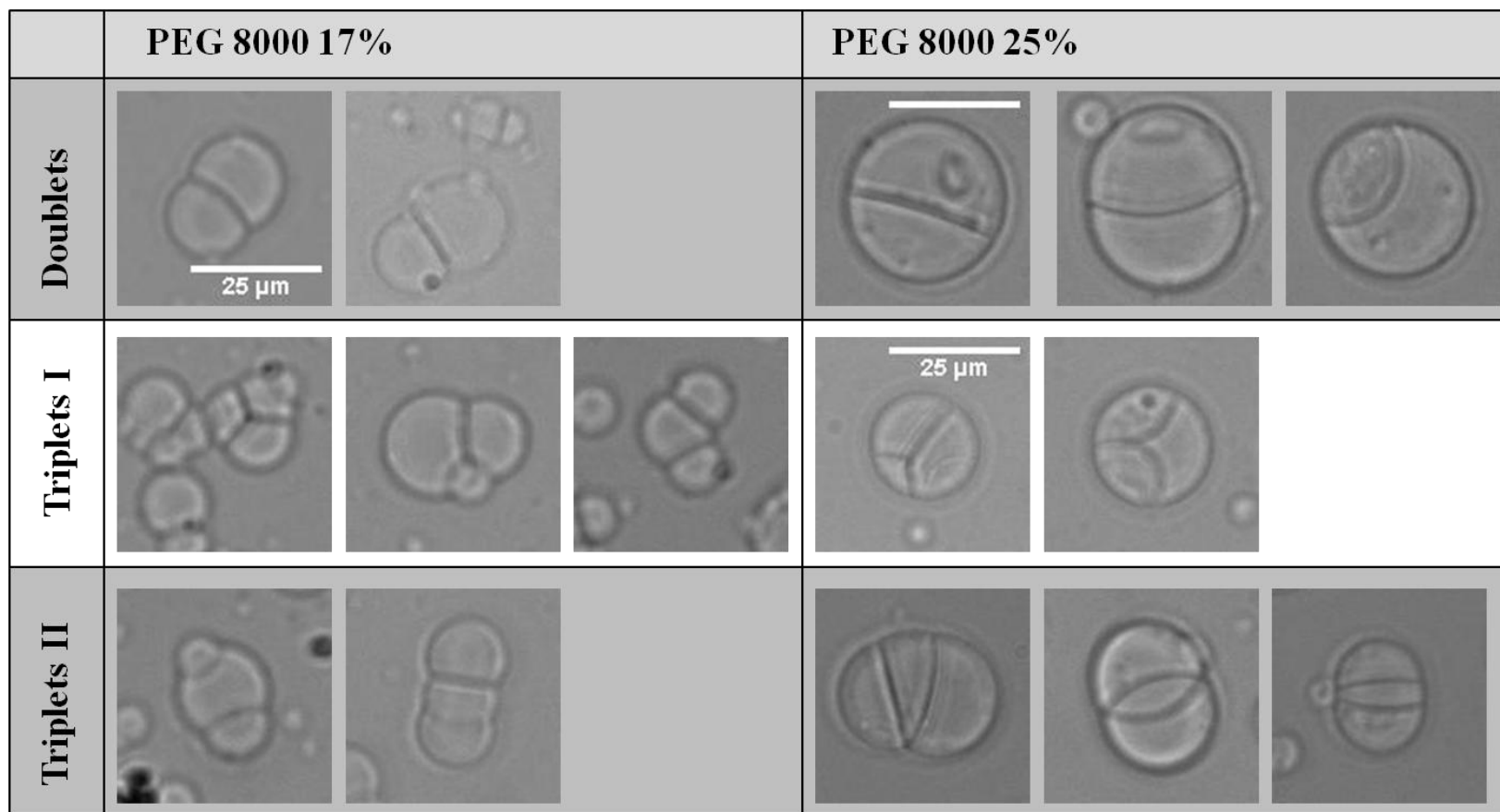
Figure 3.5. Comparison of polymersome clusters produced at two attraction strengths. Cluster morphologies are classified according to the number of adhering vesicles in each cluster and its general geometry.

3.5 Fluorescence Quenching Study on Polymersome Bilayer Morphology and Surface Reactivity

3.5.1 Surface Modification of Particles and Vesicles

To probe reactivity by fluorescence signal, a reactive couramin dye was incorporated into the structures by direct labeling onto particle and vesicle surfaces. Immobilization of coumarin on carboxylated microsphere and vesicle surfaces was verified by optical microscopy. Coumarin was coupled onto bare particles to provide a control representing a surface condition where no PEG polymer brushes are present. Comparison of brightfield and fluorescence images from the microspheres indicates intense emission in the blue spectral region (Figure 3.6a, b). Vesicles incorporating 10 wt% of coumarin functionalized copolymer possess a well-defined shape with a fairly broad size range (Figure 3.6c). The labeled bilayer structure surrounding the polymersome is clearly visible in corresponding fluorescence images (Figure 3.6d). Although the bulk fluorescence intensity increased linearly with the amount of labeled copolymer incorporated up to 50 wt% (data not shown), the corresponding vesicle sizes also became much smaller. We therefore selected 10 wt% of labeled copolymer as an optimal concentration to ensure structural integrity of the vesicles while maintaining a strong fluorescence signal.
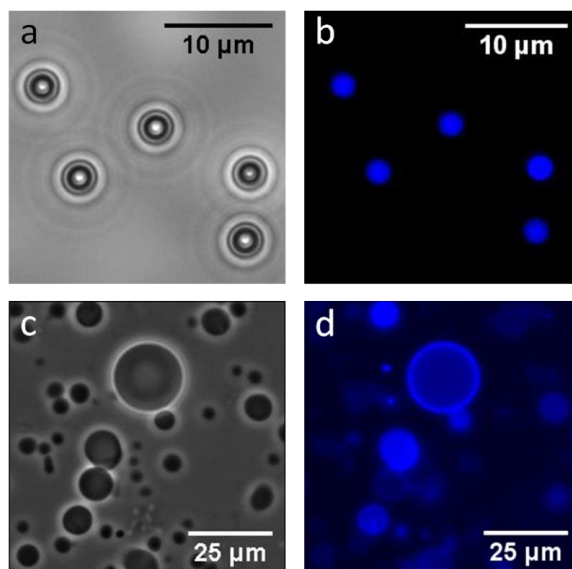
Figure 3.6. (a) Brightfield and (b) fluorescence images of 2 µm FluoroSphere® particles, surface modified with coumarin. (c) Phase contrast and (d) fluorescence images of PEO_{89}-PBd_{120} vesicles functionalized with 10 wt% coumarin-labeled copolymer.

3.5.2 Fluorescence Quenching of Coumarins on Different Surfaces

Figure 3.7a shows the steady-state fluorescence emission spectrum of coumarin in aqueous solution as a function of iodide concentration at an excitation wavelength of 375 nm. Maximum emission intensity was observed in the absence of iodide, and no shifts in either the absorption or emission spectra were observed upon addition of salt. Significant fluorescence quenching was observed upon addition of iodide (e.g., intensity decreases by a factor of 2 when 3×10^{-2} M of iodide is added into the solution). In contrast, the intensity remains constant when other halides (Cl^-, Br^-) are used, even at the highest concentrations studied here (0.15 M; data not shown). Similar spectral characteristics as a function of iodide concentration were exhibited by coumarin on particles in solution under identical excitation conditions (Figure 3.7b). The modified

particles were diluted into solutions containing a mixture of NaCl/NaI with a total salt concentration of 325 mOsm/kg. Corresponding fluorescence spectra of vesicle solutions appear broader with a much higher background than the particles due to polydispersity in size and possible impurities present in the vesicle samples (Figure 3.7c). But these effects can be removed by subtracting the scattered intensity profile measured in an unlabeled vesicle solution. The resulting corrected spectra appear similar to those measured in the free solution and particle cases, with a reduction in intensity as iodide concentration increases (Figure 3.7d).
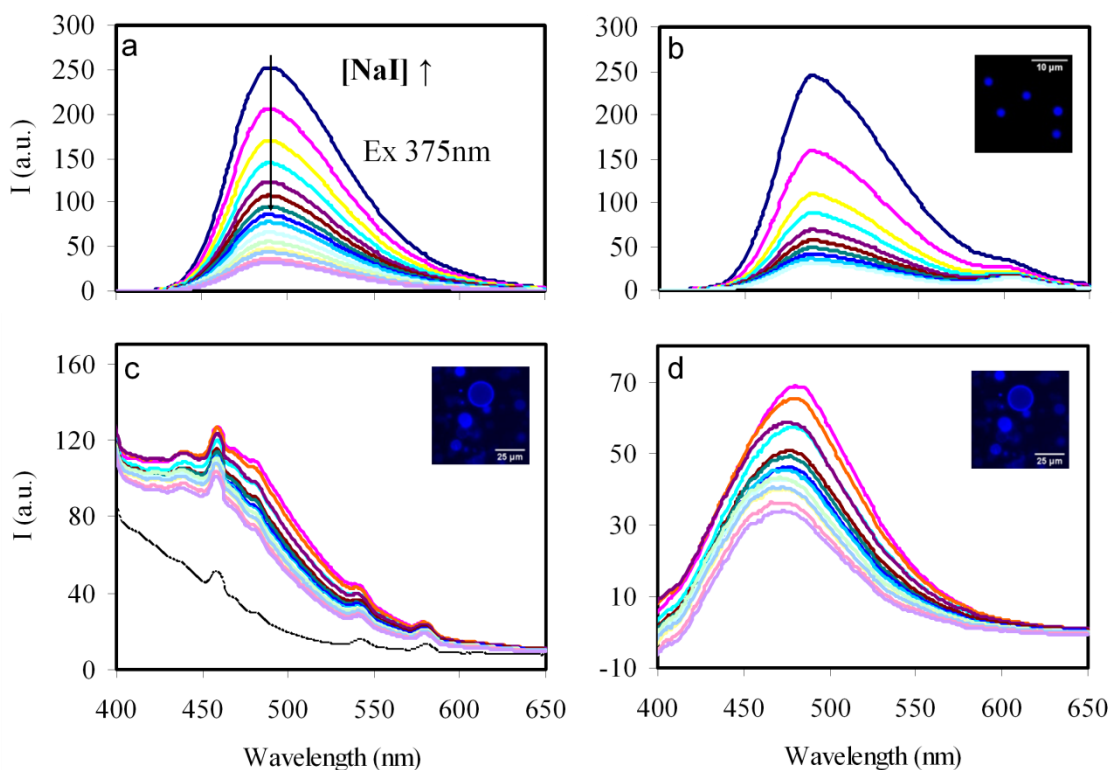
Figure 3.7. Fluorescence emission spectra of coumairn (a) in aqueous solution in the absence and presence of NaI([coumarin] = 200 nM; λmax = 490 nm), (b) immobilized on particle surfaces in 0.15 M solutions of NaCl and NaI, and (c) on vesicles surface (raw data). (d) Corresponding to (c) after subtracting background intensity.

Figure 3.8 shows the variation of fluorescence intensity I_0/I at 490 nm with increasing concentration of iodide. It is apparent that the extent of quenching for free coumarin in aqueous solution and coumarin immobilized on particle surfaces (open symbols) is much greater than either of the coumarin labeled vesicles (filled symbols), which showed rate reductions of more than 50 percent. It can also be seen that the magnitude of quenching is further decreased for vesicles made with $Cou-PEO_{89}-PBd_{120}$ in $PEO_{89}-PBd_{120}$ (labeled copolymer surrounded by brushes of the same length) than in $PEO_{20}-PBd_{33}$ (labeled copolymer surrounded by shorter brushes), suggesting that surface topology as well as presence of PEG brushes appears to play a role in shielding the quenching reaction on the surface.

Unfortunately, extraction of quantitative quenching rates using the standard Stern-Volmer analysis in Eq. 2.1 is challenging due to an overall trend of upward curvature in the data. We investigated this further by fitting the fluorescence versus concentration data using formulations based on the sphere of action model and finite sink approximation. Both approaches accurately represented the data trends and yielded reasonable quantitative predictions of the bimolecular quenching rates. In the sphere of action model, a reaction distance is defined where a quencher molecule within the corresponding spherical volume (V) is assumed to be able to quench the excited fluorophore without a diffusion-controlled collisional interaction. Modification of the linear Stern-Volmer equation using this approach is accomplished by assuming the quenchers are randomly distributed in the solution (the probability of static quenching is given by a Poisson distribution $\exp(V[Q])$), and thus the overall fluorescence intensity is

reduced by this factor. The finite sink approximation is based on a similar idea, but it is treated more rigorously by integrating the solution flux equation used to describe quenching rate constants over the diffusive region of interest ($R \leq r \leq r_0$) rather than simply correcting the final fluorescence intensity with an exponential factor. No pre-assumptions about whether the reaction is diffusion or activation energy controlled are required in order to extract the diffusion coefficients. Consequently, the finite sink model is considered more suitable for comparing diffusion properties of quenching events within the context of this study.
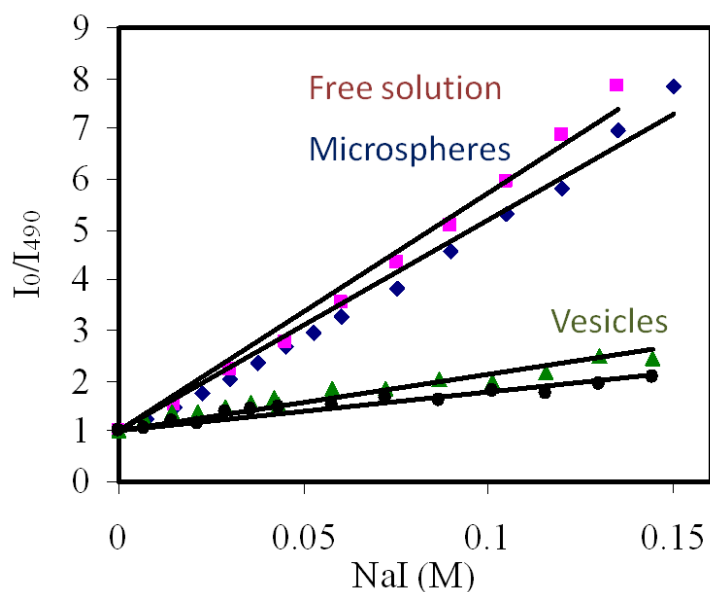
Figure 3.8. Comparison of Stern-Volmer plots for quenching of coumarin in free solution (◆), on particle surfaces (■), on vesicle surfaces where the labeled copolymer surrounded by brushes of the same length (Cou-PEO$_{89}$-PBd$_{120}$ in PEO$_{20}$-PBd$_{33}$; ▲), and on vesicle surfaces where the labeled copolymer surrounded by shorter brushes (Cou-PEO$_{89}$-PBd$_{120}$ in PEO$_{89}$-PBd$_{120}$; ●). Solid lines are linear fits intended to guide the eye.
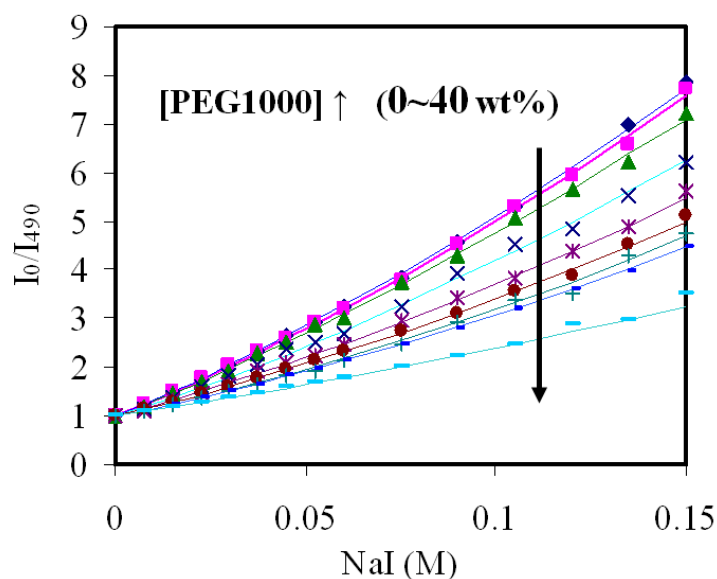
Figure 3.9. Non-linear Stern-Volmer plots of coumarin in free solution containing different PEG concentrations (0, 2.5, 5, 10, 15, 20, 25, 30, 40 wt%, MW 1000 Da). Solid lines are fits obtained using Eq. 3.3.

3.5.3 Quenching in PEG Solutions

Next, we examined the effect of adding PEG to the surroundings of a fluorophore on the quenching reaction. PEG of a desired amount was pre-dissolved in DI water as a co-solvent, then NaI and a trace amount of $Na_2S_2O_3$ were added to part of the PEG solution to make a quencher stock. Fluorescence quenching in PEG solutions was then carried out by mixing alternating proportions of quencher stock with the original PEG solution, and adding aliquots of coumarin (pre-dissolved in MeOH/DI). The solvent composition remains virtually unchanged since the volume of the added fluorophore solution is minimal. Figure 3.9 shows that the intensity at 490 nm decreases with increasing quencher for all PEG concentrations, similar to the trends observed in Figure 3. The solid lines in the plot represent fits to the data using equation 4, with the terms C_1

$= f\tau_0 4\pi N_{AV}DR$ and $C_2 = fR$ as adjustable parameters. For the diffusion-limited process considered here, $f \rightarrow 1$ and C_1 becomes equal to the quenching rate K_q. The slopes of the quenching curves approach C_1 at low quencher concentrations and show a decreasing trend with increasing polymer concentration, indicating that addition of polymer results in a reduced quenching rate.

Figure 3.10 shows quenching rates normalized to the polymer-free case (K_q/K_{q0}) as a function of polymer concentration for three different molecular weights of PEG, along with the corresponding solution viscosities. Eq. 3.3 indicates that quenching rate K_q is directly proportional to the diffusion coefficient, which in general is inversely proportional to viscosity—a solution property influenced by polymer concentration and molecular weight. However, these data also show that the reduction in quenching is not dependent on PEG molecular weight. Furthermore, the viscosity data show a diverging trend, especially at high molecular weight, indicating that quencher diffusion is not influenced by the bulk viscosity. Instead, the decrease in quenching rate could reflect an exclusion and/or kinetic effect when the PEG brush is in the vicinity of the fluorophore.
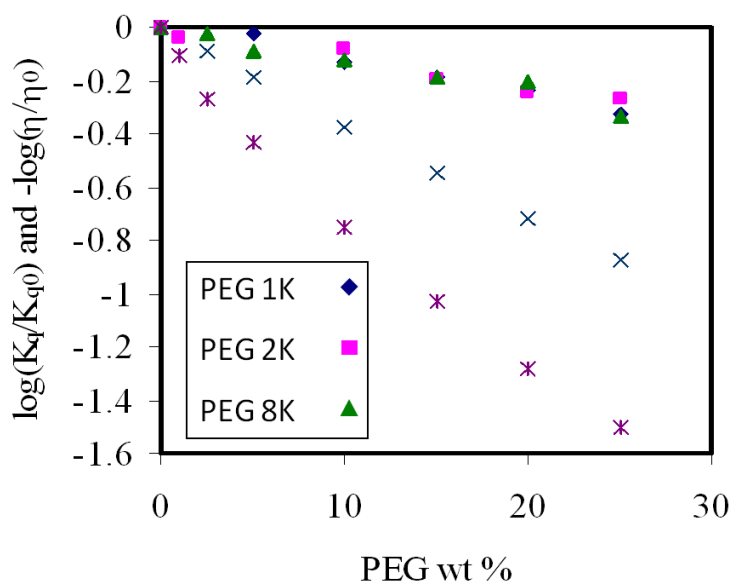
Figure 3.10. Logarithm of ratio of K_q to its value at zero PEG concentration as a function of PEG concentration in aqueous solution. Data are shown for PEG molecular weights of 1000 (◆), 2000 (▲), 8000 (■) Da. The concentration dependence of solution viscosity relative to its value at zero PEG concentration is also shown for PEG molecular weights of 2000 (×) and 8000 (✳).

3.5.4 Kinetics or Themordynamic Exclusion?

To determine whether the observed reduction in quenching with increasing polymer concentration could be due to ion exclusion effects, dialysis experiments were performed and ion concentrations were measured on each side of the membrane (Table 3.1). Exterior KCl solutions were diluted to the proper range for conductivity measurement, and the conductivity value κ was converted to KCl salt concentration. A calibration curve was made and compared to literature values.[109] KCl concentrations inside the membrane (i.e., in the presence of PEG) were determined using an equilibrium dilution factor. These data indicate that equilibrium salt concentrations are identical inside and outside of the dialysis membrane irrespective of the initial PEG or salt

concentrations. These results suggest that ion exclusion effects do not play a significant role in the quenching phenomena observed here. Consequently, the presence of PEG appears to impose a kinetic effect rather than a thermodynamic one.

Table 3.1. Salt Partition in PEG-water

	$C_{out}{}^{\alpha}$	C_{in}*
PEG 50wt%	129.2	128.6
	102.9	102.9
	59.4	60
	42.0	42.9
	8.0	8.6
PEG	112.5	112.5
	94.6	90.0
	38.4	37.5
	7.5	7.5

*C_{in} is calculated assuming no preferential partition of ions in PEG-water system.
$^{\alpha}C_{out}$ is determine through electric conductivity measurements.

The magnitude of this kinetic effect can be quantified via transport property measurements of electrolytes in aqueous PEG solutions. Figure 3.11 shows the extent of conductivity reduction caused by the addition of PEG. In dilute electrolyte solutions, electric current represents the sum of currents carried by individual ions assuming no ion-ion interactions (i.e., independent migration). Under these conditions, the conductivity of an electrolyte solution is described by[110]

$$\kappa = \sum_{\pm} \kappa_i = \sum_{\pm} z_i e \mu_i c_i \qquad (3.4)$$

where z_i is the valence of species i, e the fundamental charge, μ_i is the electric mobility and c_i is the number concentration of species i. The decrease in ion mobility (i.e.,

velocity of ions under an electric potential gradient) of the PEG solutions, apparent by smaller slopes of the conductivity-concentration data, indicates that quenching is strongly influenced by ion mobility effects.
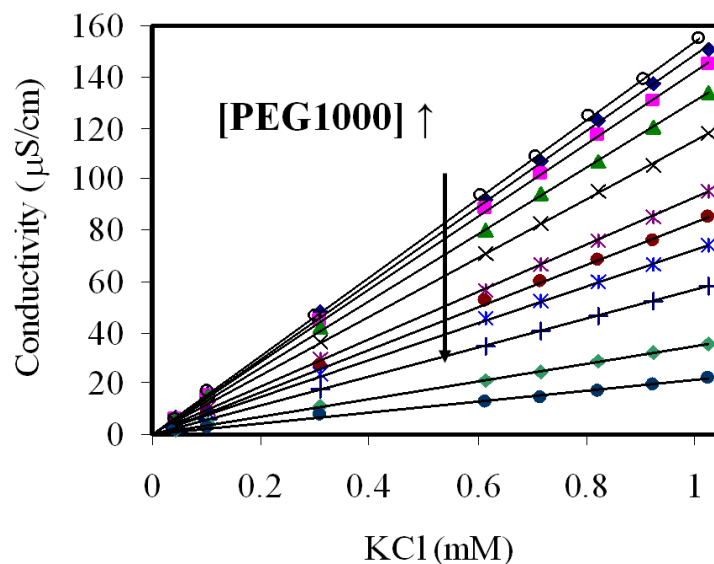
Figure 3.11. Variation of conductivity with KCl concentration for different PEG concentrations (0, 1, 2.5, 5, 10, 15, 20, 25, 30, 40, 50 wt%, MW 1000 Da). Solid lines are linear fits intended to guide the eye.

3.5.5 Ion Diffusion versus Quenching

The retardation of ion mobility in polymer solutions can be attributed to the decrease in free volume of the solvent through which the ions travel. The addition of polymer reduces the effective volume of the conducting solution such that ion migration is influenced primarily by the total volume rather than the detailed structure of the polymer in solution. The effective resistance to ion transport is therefore related to polymer volume fraction rather than bulk viscosity. This is validated through the data shown in Figure 7a, where mobilities measured in different PEG molecular weights

collapse onto the same curve. Diffusion coefficients are related to the ion mobilities by the Nernst-Einstein equation

$$D_i = \mu_{p,i} k_B T = \frac{\mu_i}{|z_i| e} k_B T$$

(3.5)

where μ_p is the mechanical mobility, μ is the electrical mobility from Eq. 3.4, k_B is the Boltzmann constant and T is the absolute temperature.

A number of physical models have been proposed to describe small molecule diffusion in polymer solutions, including concepts based on obstruction effects, hydrodynamic interactions, and the free volume.[111] The free volume theories (i.e., lattice models) view the diffusion process as a succession of jumps driven by thermal motion of the small molecule species, with the polymer represented as an impenetrable obstacle. Models based on free volume theory are well-established for a variety of polymer-solvent systems, and the corresponding diffusion coefficients are found to agree with experimental values over a wide range of polymer concentration. The widely used Vrentas-Duda free volume theory[112-113] has been particularly successful in describing probe diffusion in polymer solutions,[114-116] but is challenging to apply in our system due to the numerous physical parameters that need to be specified. In our case, a single parameter modified Yasuda free volume theory[104] adequately describes the polymer concentration dependence of ion diffusion, as represented by the solid line in Figure 3.12a.

$$\frac{D}{D_0} = \frac{\mu}{\mu_0} = \exp\left[\frac{B_s}{f_w} \left(1 - \frac{1}{\gamma_w \left(1 - \varphi_p\right)} \right) \right]$$

(3.6)

Here, D is the self-diffusion coefficient of solute in the polymer-solvent mixture, D_0 is the self-diffusion coefficient of the solute in pure solvent, B_s is the minimum hole size required for diffusive displacement, f_w is the free volume of the solvent polymer-water system, and φ_p is the volume fraction of the polymer. The quantity of B_s/f_w is a fitting parameter that, based on our data, yields a value of 2.38. The activity coefficient of water γ_w was calculated using the Flory-Huggins equation.[117]

$$\ln \gamma_w = \ln\left(\frac{\varphi_w}{x_w}\right) + \left(1 - \frac{1}{m}\right)\varphi_p + \chi\varphi_p^2 \tag{3.7}$$

The interaction parameter χ of PEG in water was taken as 0.5 for PEG 2000[118] (m is the ratio of the molecular weight of polymer to that of water).
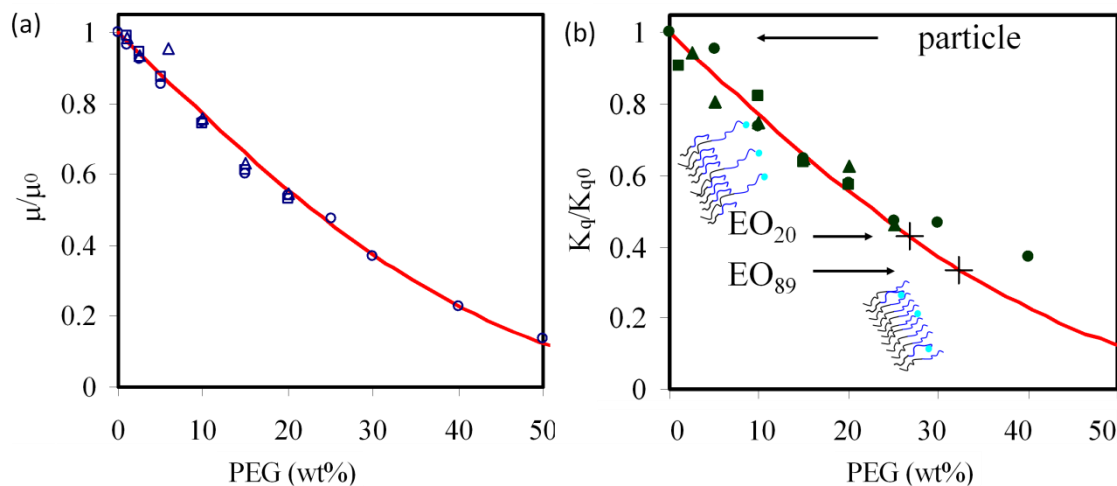
Figure 3.12. (a) Mobility retardation and (b) quenching rate reduction as a function of PEG concentration in aqueous solution. Data are shown for PEG molecular weights of 1000 (●), 2000 (▲), and 8000 (■) Da. The solid lines are fits obtained using the Yasuda free volume model (Eq. 3.6 and Eq. 3.7). These fits make it possible to apply data from quenching measurements made in PEG solutions to infer the local PEG concentration on particle and vesicle surfaces.

Figure 3.12b shows the fluorescence quenching rates in PEG solutions normalized to the polymer-free case as a function of polymer concentration for three different molecular weights, as well as the quenching data for the two vesicle samples. Normalized quenching rates in the PEG solutions are also closely fitted using the modified Yasuda free volume model. For the bimolecular quenching process on vesicle surfaces, where the coumarin is attached to the polymer, the fluorescent probe is essentially stationary on the time scale of the motion of the ion. It can thus be concluded that the measured quenching rates should be directly proportional to the corresponding ion diffusion coefficients. A general expression for the bimolecular reaction with rate constant $Z \exp(-E_a/RT)$ yields the following equation for the reaction rate r_q

$$r_q = Z \exp\left[\frac{-E_a}{RT}\right][A][B] \tag{3.8}$$

where E_a is the activation energy of the reaction, and R is the gas constant. The pre-exponential factor Z represents the collision frequency of the reactants A and B, with A being the fluorophore and B the quencher. The total collision frequency of A with B is given by $Z[A][B] = N_{AV}^2 \sigma_{AB} \bar{v}[A][B]$ where σ_{AB} is the reaction cross section, and $\bar{v}$ is the average velocity. Since the fluorophore is immobilized onto a large polymer, the velocity is primarily associated with the freely diffusing quencher, so the average velocity can be replaced by the velocity of the ion v_B. Therefore, at constant temperature, the reduction in quenching rate can be directly correlated to a corresponding change in ion diffusivity.

$$\frac{r_q}{r_{q,0}} = \frac{K_q}{K_{q0}} = \frac{v_B}{v_{B,0}} \propto \frac{D_B}{D_{B,0}} \tag{3.9}$$

This correlation between the normalized diffusion coefficient and weight concentration of the quencher (roughly equal to volume concentration) has important consequences because it provides a straightforward way to use quenching measurements made in PEG solutions to infer the local PEG concentration surrounding the chain end on a vesicle surface. Applying this analysis using quenching data obtained from the two vesicular surface structures considered (i.e., a long labeled copolymer surrounded by long or short bushes) leads to several key observations (Figure 3.12b). First, the estimated surface PEG volume fractions increase from 27% to 32% as the bilayer composition changes from PEO_{20}-PBd_{33} to PEO_{89}-PBd_{120} (the unlabeled copolymer concentration in the bilayer is held constant at 90 wt%). These surface volume fractions, reflecting a weighted average of the labeled chain end distribution and polymer volume fraction as a function of depth, are within solubility limits (~57 vol%) reported in chemisorbed PEO layers.[119] Secondly, the 32% surface volume fraction estimated in the monodisperse short PEO brush membrane is a relatively high value, in the range of those reported in compressed polystyrene-poly(ethylene oxide) (PS-PEO) diblock copolymer monolayers at air-water interfaces.[120-121] This could be explained in terms of a morphology where chain ends are mostly buried inside the brush structure, which would be expected to reduce the observed quenching rates. Conversely, when the longer Cou-PEO_{89}-PBd_{120} is interspersed among surrounding shorter PEO_{20}-PBd_{33} polymers, the longer chain ends are more likely to extend to the outer edge of the brush,[122-123] yielding

a corresponding increase in quenching rate (we emphasize that the density of labeled chain ends is the same in both vesicular surface structures considered).

The structure of the outer brush surface exhibits a complex dependence on the molecular weight ratio of the long and short polymer, as well as their respective surface densities. Localization of polymer terminal groups relies strongly on the interfacial properties, and chemical modification of chain ends can influence segregation by changing the surface energy.[124] Manipulating the extent of vertical segregation in this way (e.g., by using a charged fluorophore) would directly affect the observed quenching rate, thereby raising the possibility of harnessing our approach to directly probe these interactions.

Our observations indicate that the quenching reaction rate appears to occur 2~3 times more slowly when one of the reactive species is tethered onto the vesicle surface. From a surface modification standpoint, this suggests a broad capability to precisely tune the reaction rates by simply changing the copolymer formulation to create bimodal brushes with different architectures. Additionally, reactions on such surfaces can be size-selective since molecular mobility is attenuated with increasing size in a dense PEG brush. For example, the Yasuda free volume model predicts that the normalized diffusivity of a molecule three to four times the size of an iodide ion in a 0.3 volume fraction PEG medium will be reduced ten-fold. It therefore stands to reason that when an active polymer surface is exposed to a mixture of various size reactants (assuming similar reaction pathways and energies), the larger species will experience a much slower reaction rate due to these exclusion effects. Future studies to elucidate the

interplay among quencher size, surface reaction, and interfacial segregation of chain ends have great potential to establish design parameters that would enable intelligently controlled surfaces to be developed for sensor or specific targeting applications.

3.6 Conclusions

Polymer vesicle system is a versatile platform for cell mimicry. Here, we have described a depletion approach to induce the assembly and organization of giant polymer vesicles. As complexity was build upon the simple self-assembled structures, it is crucial to characterize how the presence of PEG and polymer atchitectue affects reactivity on polymersome surfacds. This was accomplished by developing an approach based on straightforward fluorescence quenching measurements. A fluorescent probe was successfully tethered to bare particle surfaces and onto the hydrophilic terminus of a long polymer vesicle building block. The presence of polymer dramatically decreased the quenching rate, and the greatest reduction was observed on vesicle surfaces composed of a single length copolymer. This can be explained by considering that the labeled chain ends experience increased exposure to the surroundings in the case where the reactive tether is surrounded by shorter brushes, resulting in a clearly distinguishable difference in quenching rate. A diffusion model was used to relate the reduction in quenching to ion diffusivity in the polymer solution. This correlation approach makes it possible to directly estimate the local polymer concentration in a self-assembled bilayer structure, and ultimately offers a promising straightforward approach that can be useful in the design of a variety of functional surfaces.

CHAPTER IV

ISOTROPIC-NEMATIC PHASE TRANSITION OF ZIRCONIUM PHOSPHATE BASED PLATELET SUSPENSIONS

4.1 Synopsis

Stable colloidal suspsensions of Zirconium phosphate nanosheets with counter-cations on their surfaces were prepared by exfoliating highly crystalline α-Zirconium phosphates crystals. The suspension of high aspect ratio nanosheets forms a birefringent, ordered liquid crystalline phase (i.e., discotic nematic) above a critical concentration. Sharp boundaries between the separated phases in the biphasic region enables us to characterize this transition. This chapter reports the effect of organic cations (exfoliating agents) — tetrabuylammonium, tetrapropylammonium, tetraethylammonium, and tetramethylammonium on the istotropic-nematic phase equilibrium. The transition concentration increases with the size of the exfoliating agents, indicating the dominating effect of shape anisotropy over hydrophobic interactions. In addition, polydisperstiy reduction of the condensed phase was obtained through nematic liquid crystal fractionation. By careful analysis of size distribution in the upper isotropic and lower ordered phases separated and compressed via gravity, size segregation was found to occur more significantly at higher particle concentrations rather than in the isotropic-nematic phase region. Finally, a novel exfoliation approach of expanding layer spacings with a small molecule, and subsequently exfoliating with a bulky polymeric one resulted in a more robust, polymer stabilized, discotic suspension system in aqueous media.

4.2 Introduction

Inorganic layered compounds, such as MoS_2, Niobium layered oxide (Niobates), clays, and α-Zirconium phosphates (α-ZrP), upon exfoliation, are two-dimensional (2-D) materials with high surface suitable for the preparation of a diverse array of hybrid materials for sensing, photo-catalysis, energy harvesting applications. Similar to the organic layer compound—Graphene, successful exfoliation and dispersion in a fluid phase is essential to the performance of the composite materials.[125-127] A key feature of these 2D colloids that has been neglected in most studies is its anisotropic shape, which favors the formation of ordered assemblies, namely liquid crystalline phases, via self-assembly. Only since the past decade has experimental studies on colloidal, discotic liquid crystal started to emerge.[35,44-45,128-129]

The liquid crystal phase behavior of anisotropic particles (e.g., rod-like and plate-like particle) is determined by excluded volume interactions (i.e. aspect ratio) and inter-particle forces.[28,50,130-131] For 2-D platelets prepared by chemical exfoliation, the compound used for exfoliation play an important role in determining the surface properties, and hence the inter-platelet interactions. Additionally, the aspect ratio of the platelets can also be altered via the thickness of the adsorbed counterion layer. Any change in the properties of the exfoliating agent could translate to the change in suspension stability and phase behavior. Although some studies have been focused on solvent ionic strength- mediated interactions[49] or depletion attraction induced change in discotic phase diagram,[50,132] not much attention has been paid to the effect of the surface complex moiety.

Herein, we describe aqueous-based exfoliation and functionalization of ZrP nanosheets using a series of tetraalkylammoniums and a combination of *n*-alkylamine with hydrophilic Jeffamines. The effect of different organic cation (tetraalkylammoniums, length of alkyl chain range from one to four) on the istotropic-nematic transition of the discotic suspensions will be investigated. The efficacy of liquid crystal fractionation to reduce polydispersity of the condensed phase was also examined. Additionally, it has been known that the electrostatic anchoring of protonated amines onto ZrP surfaces provides a stronger association than quaternary ammoniums like TBA$^+$, the common exfoliating agent used to produce colloidal suspensions of ZrP monolayers.[133] However, alkylamines used widely for intercalation do not provide good exfoliation in water due to their hydrophobic nature; Jeffamines, a hydrophilic polyether with amine functionality, on the other hand, are too large to diffuse into interlayer galleries for exfoliation. We describe a novel exfoliating approach using a mixture of these exfoliants which produces ZrP dispersions of superior stability than the regular TBA-exfoliated ones.

4.3 Ordered Phase Formation of Organic Cation Exfoliated ZrP

4.3.1 Exfoliation of α-ZrP with Tetraalkylammoniums
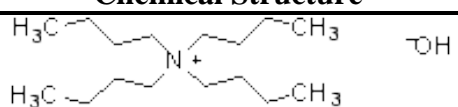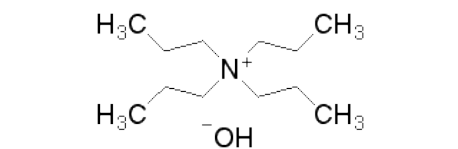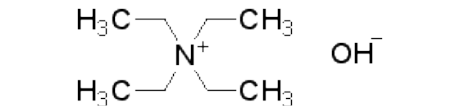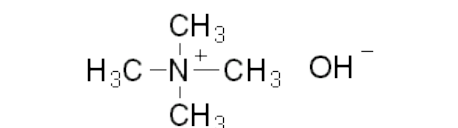
α-Zirconium phosphate particles were synthesized and exfoliated by the addition of Tetraalkylammonium (R_4N^+) hydroxide solutions, as described in the general procedure section 2.2.4. In addition to the commonly used tetrabutylammonium hydroxide, the use of three other basic cation solutions (Table 4.1.) was investigated.

Intercalation/exfoliation reaction of acidic layered metal phosphate follows the chemical formula:

$$Zr(HPO_4)_2 \cdot H_2O + xR_4N^+OH^- \leftrightarrow Zr(HPO_4)_{2-x}(R_4H^+PO_4^-)_x + (1+x)H_2O \qquad (4.1)$$

Where the maximum H^+ displacement is half of the available ionizable phosphate groups in α-ZrP (molar ratio of R_4N^+ to α-ZrP x = 1), due to geometric constraints of the bulky organic cations:[134] The distance between two neighboring phosphate groups (~5.24 Å) on ZrP crystal lattice[135] is smaller than the size of most tetraalkylammonium ions. Experimentally, by increasing molar ratio of R_4N^+ to α-ZrP in the mixture, intercalation and exfoliation occurred in a similar way for the entire series of R_4N^+ (R = Methyl, Ethyl, Propyl, and Butyl). The particle and $R_4N^+OH^-$ mixtures (< 0.5 mg/mL ZrP) became noticeably less opaque at molar ratios x above 0.8, and turned into colloidal suspensions of single-layer platelets.

Table 4.1. List of Tetraalkylammonium Hydroxides Used for Exfoliation

Exfolianting agent	Chemical Structure	Cation Size (nm)
TBA^+OH^-		0.95~1.05
TPA^+OH^-		0.80~0.90
TEA^+OH^-		0.65~0.75
TMA^+OH^-		0.50~0.60

At one to one intercalation ratio (molar ratio between the exfoliant and α-ZrP) with the tetraalkylammoniums, α-ZrP particles are considered completely exfoliated, where the suspension appeared transparent at low particle concentrations. This is verified from the powder X-ray pattern in Figure 4.1 of dried, re-stacked layers. Figure 4.1a demonstrated schematically the expected structure of the dried layers as reported previously,[136] where the distances between the layers would be expanded to incorporate a monolayer of organic cations. The restacked exfoliated α-ZrP have larger interlayer spacing than the original compound (7.6 Å), and the peak positions corresponding to interlayer distances shifted systematically with the size of the exfoliating agents (Figure 4.1b). The restacked layers from TBA-exfoliated particles has an interlayer spacing of 17.0 Å, comparable to values reported in the literature for single-layered cation arrangements in the restack phase (ZrP layer thickness is 6.3 Å). Since the four-armed organic cations do not tilt like single-chained molecules[137-138], the inter-gallery heights can be estimated with known ion sizes (Table 4.1) by adding the value of cation diameter to the layer thickness: 14.8 Å ~15.8 Å for TPA-ZrP, 13.3 Å ~14.3 Å for TEA-ZrP, and 11.8 Å ~12.8 Å for TMA-ZrP samples. The agreement between the experimental values from the diffraction patterns and the estimated values (except for TPA-ZrP) indicates a single-layer ion arrangement between the layers as we expected.
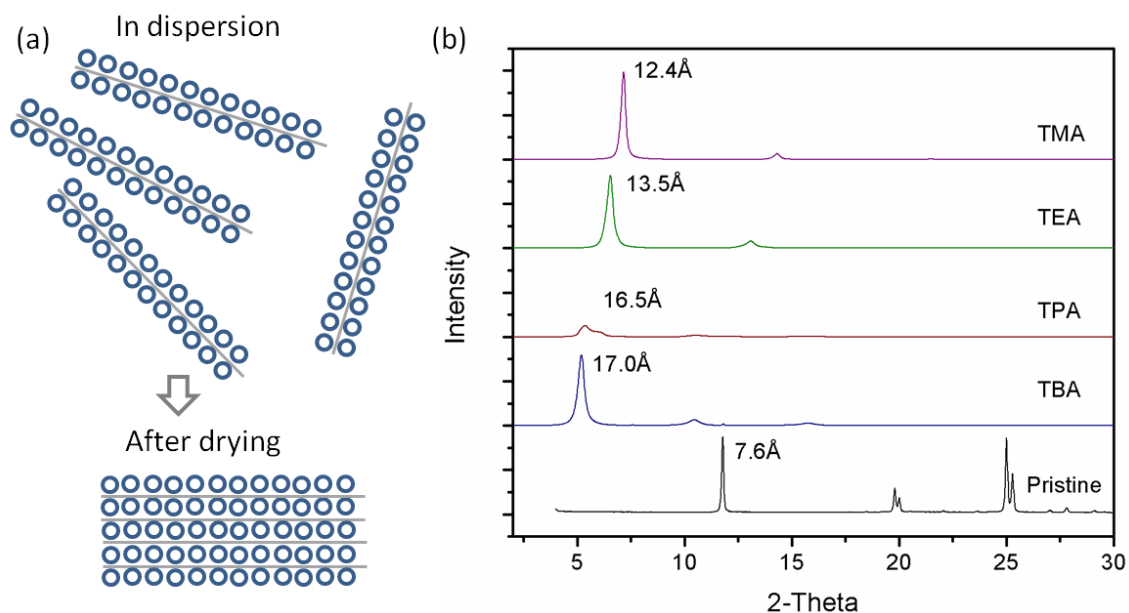
Figure 4.1. (a) Schematic of restacking of exfoliated α-ZrP platelets upon drying. Circle dots represent tetraalkylammonium molecules and the straight lines represent α-ZrP. (b) XRD patterns of exfoliated and restacked nanoplatelets.

4.3.2 Effect of Organic Cations on I-N Phase Transition

Suspensions of all four tetraalkylammonium exfoliated ZrP forms liquid crystalline phases at packing fractions above certain threshold value, i.e., the isotropic-nematic transition concentration (ϕ_I). Figure 4.2 shows the various liquid crystalline textures observed at increasing particle (from left to right) concentrations under cross polarizer. The suspension displays nematic-like schlieren texture at lower concentrations (note: the texture in the Figure 4.2a evolves over time and the defect lines changes), and transforms into birefringent textures with patchy domains at a slightly higher concentration (Figure 4.2b), reminiscent of that of twist grain boundary (TGB) phase.[139-141] As the concentration increases even higher up to 10%, the textures turned into aligned stripe patterns (Figure 4.2c), similar to fingerprint textures of lamellar phase. The exact

transition concentrations for various liquid crystal phases (N-S or N-TGB) will require the use from small angel X-ray scattering (SAXS) measurements;[128,142] the nature of the transitions (whether it be first or second order) remains elusive.
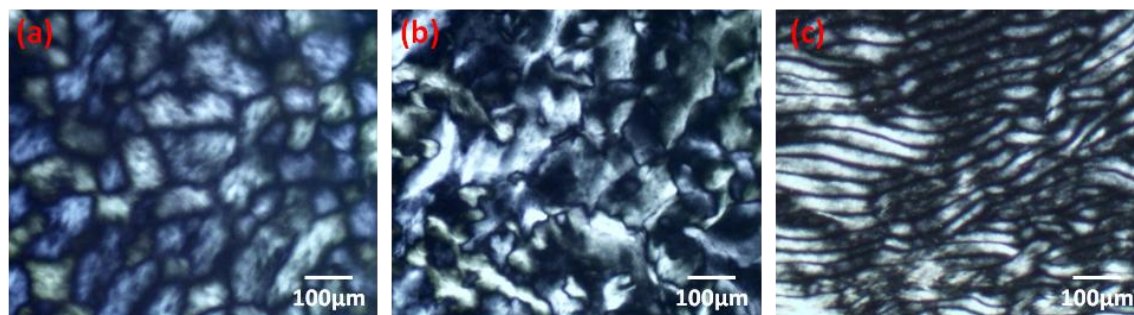
Figure 4.2. Cross-polarized microscopy images of TBA-exfoliated ZrP platelet suspensions of (a) $\phi_w \approx 0.008$, (b) $\phi_w \approx 0.012$, and (c) $\phi_w \approx 0.11$.

Here we focus on the effect of organic cation exfoliants on the nematic phase equilibrium. Phase separation of ZrP platelet suspensions with four different species of counterions was investigated and presented in Figure 4.3. The platelet suspension remains in the isotropic state up to a critical concentration (ϕ_I), where the suspension becomes permanently birefringent. Note here that the isotropic samples exhibit strong flow birefringence, which eventually disappears after the samples were rested. Above a second critical concentration (ϕ_N) the suspension is fully nematic. I-N coexistence or the biphase region is observed in the intermediate concentrations (between ϕ_I and ϕ_N), where the full phase separation yields an upper isotropic phase and a denser, lower nematic phase, with visibly sharp boundary between the two phases. The height of the nematic

layer, i.e., the proportion of nematic phase, grows with increasing total particle concentration.

Macroscopic phase separation was usually completed within 24~48 h. After complete phase separation, however, height of the nematic phase appeared to be time-dependent. This often hindered the observation of a completely nematic sample, making it difficult to identify the exact concentration where phase transition occurred. We recorded this sedimentation and nematic compression profile with time, and extrapolated the nematic heights to time zero (Figure 4.4a). A regular nematic height-particle volume fraction graph (Figure 4.4b) can then be reconstructed, and the coexisting densities ϕ_I and ϕ_N (upper boundary of biphasic region) be determined. An alternative method to determine the transition values when a complete nematic compression profile is not available is to construct a nematic height-particle concentration graph base on single images obtained at a selected equilibrium time . The nematic fraction is then defined by rescaling the original data with the plateau value in the nematic growth curve. This method is only applicable when gravity has not yet created an artificial nematic phase, which typically appears after 3 weeks (see data set represented by squares in Figure 4.4a).
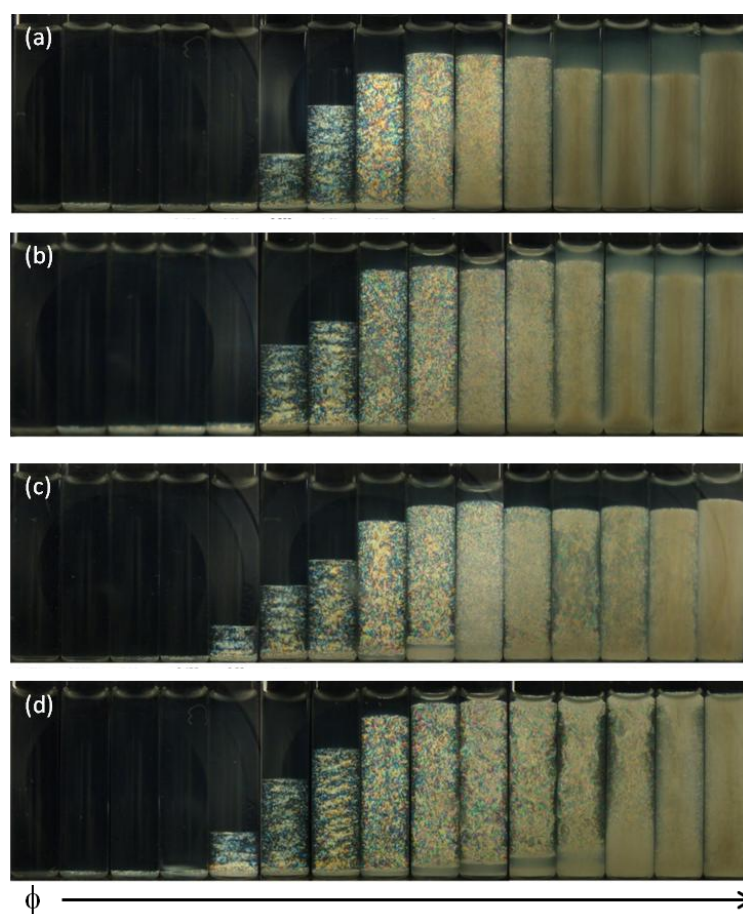
Figure 4.3. Visual observation of isotropic-nematic transition in aqueous suspensions of ZrP nanoplatelets exfoliated with (a) TBAOH, (b) TPAOH, (c) TEAOH, and (d) TMAOH. One milliliter of samples at increasing particle concentration were loaded into glass vials (~8mm diameter) and photographed under cross-polarizers. All panels contain the same series of pristine particle concentrations (0.16, 0.33, 0.39, 0.46, 0.52, 0.59, 0.65, 0.98, 1.3, 1.63, 1.95, 2.28, 2.60, 2.93, and 3.25 % in w/w).
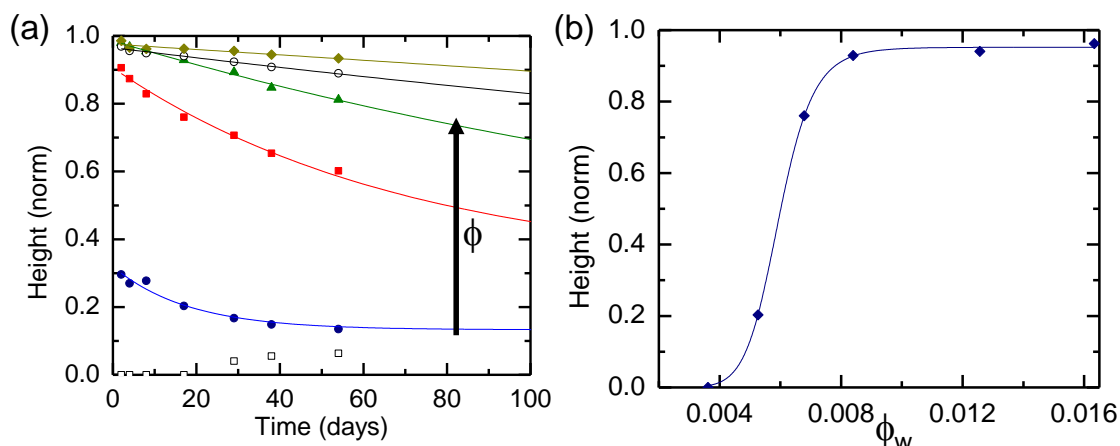
Figure 4.4. Isotroipc-nematic phase transition analysis. (a) Normalized height of nematic phase observed over time. Different symbols indicate individual samples of particle fraction, ϕ. (b) Nematic height versus particle weight fraction (ϕ_w), the line is fitted by a sigmodal function.

In all four organic cation series, the shape of the I-N transition appeared similar. All exfoliated samples used for comparison were derived from the same batch of particles, and no further processing such as centrifugation or fractionation was carried out after the particles have been exfoliated. The approximate I-N transition concentrations was estimated from the experimental data shown in Figure 4.3 by extrapolating nematic height curves (as Figure 4.4a, and methodology outlined in previous paragraph) to height = 0. The results are listed in Table 4.2. The weight fractions (recorded as α-ZrP particle added) were converted to volume fractions for each transition point, taking into account the geometric factor of the cation layers. Specifically, the volume fraction was increased by a factor of 2.4, 2.7, 3.4, and 3.6 from the exfoliation with TMA, TEA, TPA, and TBA, respectively. From the results of the four series, it occurs that the propensity to form ordered phase varied systematically with the alkyl chain length of the cations. The I-N transition volume fraction increases in the

sequence TMA < TEA < TPA < TBA, a result that demonstrates the dependence of ordered phase formation with platelet aspect ratio, as modulated by the surface counter-cations. We found via the estimated aspect ratios and transition concentrations (Table 4.2), a power law relationship written as $\phi_I \propto \xi^m$, where ξ is the inversed aspect ratio and the scaling exponent m = 1.78 ± 0.02. This relationship is in agreement with previous simulation results on I-N transitions of different aspect ratio plate-like particle, for example, Onsager-parson theory on flat cylinders, oblate hard spherocylinders[29,143] and MD simulations on cut spheres.[32] A recent experimental study on ZrP platelet, where the aspect ratio was systematically varied via synthetic/fabricated route also confirmed this scaling relationship.[144]

Table 4.2. Estimated I-N Transition Concentrations for Different Samples

Sample	Aspect ratio[a]	$\phi_{v,I}$
ZrP(TBAOH)	588 ± 20	0.0059
ZrP(TPAOH)	609 ± 41	0.0055
ZrP(TEAOH)	794 ± 21	0.0035
ZrP(TMAOH)	893 ± 15	0.0028

[a]: the aspect ratio is estimated by dividing the average diameter (1.6 ± 0.3 μm, measured with SEM) over the thickness of the platelets, taken into account the thickness of two cation layers.

4.3.3 Size Segregation in Nematic/Smectic Fractionation

As mentioned in the previous section, suspension of ZrP platelet enters I-N coexistence phase at around 0.5wt%, and the nematic proportion increases with

increasing particle concentration. During the investigation of platelet phase behavior, it has come to our attention that, after complete phase separation, the birefringent proportion does not fully occupy the sample until extremely high particle concentration in most cases (Figure 4.5). The proportion of the upper isotropic region that occurs beyond the full N phase concentration varies from batch to batch, and should in no way be regarded as a simple, first order phase separation (the I-N transition). This re-occurring phenomenon could be attributed to polydispersity/ size segregation, sedimentation, or excess exfoliating agents present in the suspension.
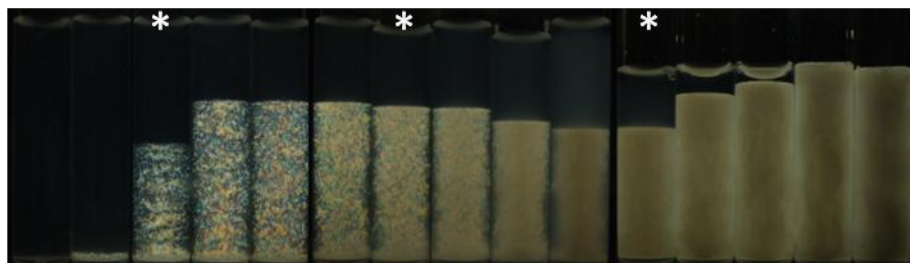
Figure 4.5. Suspension of monolayered ZrP platelets exfoliated with TBAOH photographed via cross polarizers. Concentration of platelets increases from left to right (0.71, 0.86, 1.07, 1.29, 1.50, 1.86, 2.14, 2.50, 2.86, 3.57, 5.72, 7.15, 8.58, 11.44, 14.30 wt%), "*" denotes samples used for further fractionation analysis.

The limiting case of zero polydispersity, while useful as simple model systems, is rarely encountered experimentally. Polydispersity in discotic systems could play a role in the type of liquid crystal phases (i.e., columnar or smectic) formed at higher particle concentrations[35,44]. Polydispersity also has a dramatic effect on the location I-N transition, as described in Frenkel's simulation study.[39] In particular, particle size segregation is associated with the I-N phase separation, where larger nanosheets

populating the nematic phase, reducing the polydispersity of both the lower and upper phases. Size distribution and polydispersity of the upper and bottom phases derived from a mother suspension at various concentrations was investigated. The first fractionations were performed with an initial concentration of 0.71, 2.14, and 5.72 wt%, which are in the biphase, TGB, and smectic phases' region (as denoted in Figure 4.5), respectively. Samples were prepared by diluting a concentrated suspension (> 14%) with deionized water, equilibrated for 2~5 days until a sharp interface between the phases occurred. The upper and lower phases were carefully extracted and analyzed with DLS (section 2.2.6). A second and third fractionation was to followed using the lower nematic phase from its previous fractionation. For example, the nemaitc lower phase from the 1.07 wt% was diluted again with deionized water to the biphase region, where around 50% of the sample volume was occupied by the nematic lower phase. The two phases were separated and the process repeated for a third fractionation. The results are presented in Table 4.3. Samples are identified with the notations "wt%-L/U", the numbers are the weight fraction of platelets in the mother suspension, and the letter L or U denotes lower or upper phase. A second or third notation is added for samples fractionated for more than once.

Table 4.3. Size Distribution for Fractionated and Non-fractionated Platelet suspensions

Number of Fractionations	Sample ID	Diameter (nm)	Polydispersity (nm)
	Pre-fractionation	1044±11	0.27±0.03
1st	1.07-L	1011±18	0.17±0.02
	1.07-U	913±3	0.18±0.04
	2.14-L	1063±22	0.21±0.03
	2.14-U	727±6	0.24±0.01
	5.72-L	1202±41	0.27±0.08
	5.72-U	740±9	0.26±0.03
2nd	1.07-L_0.94-L	1054±14	0.18±0.02
	1.07-L_0.94-U	994±8	0.18±0.04
3rd	1.07-L_0.94-L_0.81-L	1048±19	0.14±0.03
	1.07-L_0.94-L_0.81-U	983±8	0.12±0.04

Looking at the first fractionation, for the (I-N) biphase sample (1.07 wt%), it was expected to see the larger nanosheets populating the nematic phase and the smaller nanosheets staying in the isotropic phase, and reducing the polydispersity from 0.27 to 0.17. On the other hand, size segregation is even more dramatic for the herein-called compressed samples, namely the higher concentration suspensions (2.14 and 5.72 wt%). However, although the platelets in the lower phases of these suspensions are considerably larger than that in the upper phase, the polydispersity of both populations are still within the similar range (~0.25) of the mother suspension. For the purpose of

improving polydispersity of a platelet suspension, it is only effective then, to operate the fractionation at concentrations within the isotropic-nemtaic coexistence region. The first fractionation appeared to be the most efficient as the polydispersity was improved by almost ten percent. A second and third fractionation furthered the reduction of polydispersity only marginally, though a slight increase in size was observed. The decrease in polydispersity was evident through the accompanying change in the width of the biphase gap ($\Delta\phi_{I-N} = \phi_N - \phi_I$), from above 0.006 to 0.0035 when the polydispersity reduced from 0.27 to 0.17.

Figure 4.6 presents the dependence of size segregation on polydispersity σ and concentration of the mother suspension. We observed that size segregation is more obvious in systems with higher polydispersity, which can be emphasized when compression effect is de-coupled, and is most apparent for compressed samples (solid square data points). The results for composition distribution of the I-N coexistence phases (solid circle data points) is in good agreement with simulation data, which is represented with a fitted line ($<D_I>/<D_N> = 1 + 1.3\ \sigma^2$).[39] Our results indicate that the isotropic-nematic crystal fractionation method is a simple, effective route to reduce polydispersity from a highly polydisperse (>25 %) sample to moderate polydispersity (~20 %).
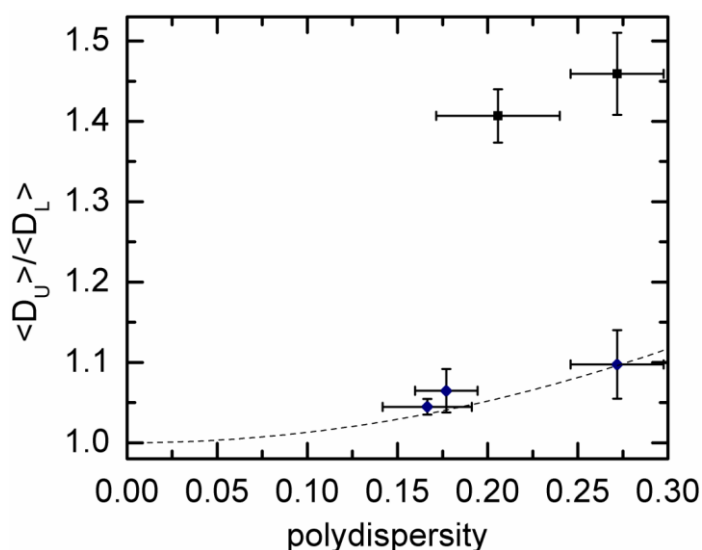
Figure 4.6. Ratio of the average diameter in the upper and lower phases as a function of polydispersity. Solid circles (●) are data obtained with I-N phase separation; Solid squares (■) are data obtained with N or TGB phase compression. The dashed line is the quadratic fitting to a simulation data for isotropic-nematic size segregation in suspension of infinitely thin platelets.[39]
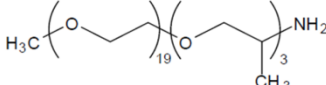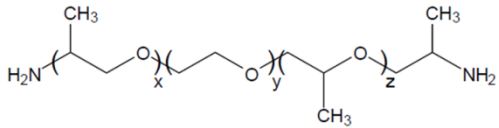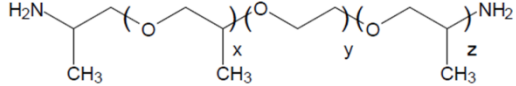
4.4. Preparation of Polymer Exfoliated ZrP Platelets

4.4.1 Exfoliation with Water Soluble Polymers

So far we have demonstrated the preparation of single-layered platelets via exfoliation with basic tetraalkylammoniums. Although TBA exfoliated ZrP platelets are stable in deionized water on their own over an extended period of time (years), one of the major drawbacks of the system is that the suspension often becomes unstable when combined with other components. For example, protein precipitation occurs almost immediately upon the addition of ZrP monolayers, forming aggregates of platelets and proteins that crash out of solution. The suspension is also unstable against dialysis, where gelled structures are formed (see next section for stability comparison). This is partially attributed to the fact that the loosely bounded, bulky cation can be easily

displaced with other cations and subsequently changes the surface properties of the platelets. This aspect is especially troublesome when applications pertaining to stable, homogenous dispersions are desired. It is therefore of great interest to replace the charged system with a more robust one.

Table 4.4. Water Soluble Jeffamines Used for Exfoliation

Jeffamine	Structure	No. of PEG units	PEG R_F (Å)
M1000		19	20.5
ED900	$y \approx 12.5, (x+z) \approx 6$	12.5	15.9
ED2003	$y \approx 39, (x+z) \approx 6$	39	31.5

Note: the PEG segment size was estimated using R_F (nm) $= 0.35$ (no. of PEG units)$^{3/5}$.[145]

Steric stabilization of colloidal particles in aqueous solution is often accomplished by particle surface modification with hydrophilic polymers such as polyethylene glycol. Hydrophilic Jeffamines are ideal candidates since they are polyoxyalkylamines that contain primary amine groups on the terminus of a polyether backbone. The proton accepting primary amines enable the molecule to be attached to ZrP surfaces, which forms a stronger bond than TBA$^+$.[134,146] Although α-ZrP intercalation with different Jeffamines[147] and the exfoliation of small α-ZrP in acetone[148] has been reported, successful exfoliation of highly crystalline, micron-sized pristine

crystal with polymeric exfoilants in aqueous has not yet been fulfilled. The effectiveness of intercalation/exfoliation is strongly dependent on the crystallinity of the pristine crystals and the architecture of the ion exchanging molecules.[138] The energy barrier required for exfoliating high crystallinity α-ZrP directly with high molecular weight (> 1000 Dalton) Jeffamines, as the ones listed in Table 4.4, is obviously too high to overcome. No sign of exfoliation was observed with the addition of Jeffamines to a α-ZrP suspension (at molar ratios up to two). The dispersion remains turbid, and the non-exfoliated particles settled to the bottom of the vial within hours under gravity.

Depending on the conformation of the molecules, interlayer spacing of α-ZrP can increase in a stepwise or continuous fashion.[138] Increasing interlayer distance facilitates the diffusion of bulky molecules into inter-galleria regions. Here, we used propylamine intercalation to expand the interlayer spacing between the α-ZrP layers, which then allows the introduction of Jeffamines into the interlayer galleries to achieve exfoliation. It has been reported that propylamine intercalation creates different percentages of intercalated phases with inter-layer spacing of 10.5 Å and 17.3 Å, which depends on the amount of propylamine incooperated.[137] Since the ultimate goal is to have a hydrophilic polymer-decorated surface, concentration of propylamine and Jeffamine were optimized to realize a surface with enough polymer coverage (minimum propylamine) while still be exfoliated effectively. A series of concentration ratios were designed by first fixing the total amount of amines added at one and two molar ratios to α-ZrP, where the proportion of propylamine to Jeffamine varied (the series included ZrP/M1000/propylamine = 1/0.2/0.8, 1/0.4/0.6, 1/0.6/0.4, 1/0.8/0.2, 1/1.2/0.8, 1/1.4/0.6,

1/1.6/0.4, and 1/1.8/0.2). The efficiency of exfoliation was judged by dispersion properties including sample transparency under regular light, ability to form birefringent nematic phase, and the amount of sediment (indicate non-exfoliated particle) under gravity. Exfoliation was observed for samples containing Jeffamine/propylamine = 1.2/0.8, 1.4/0.6, and 1.6/0.4 per mole of ZrP. The last samples offered the best transparency and obvious nematic texture under cross polarizers, which would be the chosen ratio of propylamine to ZrP (0.4 to 1 in molar ratio) for assisted exfoliation.
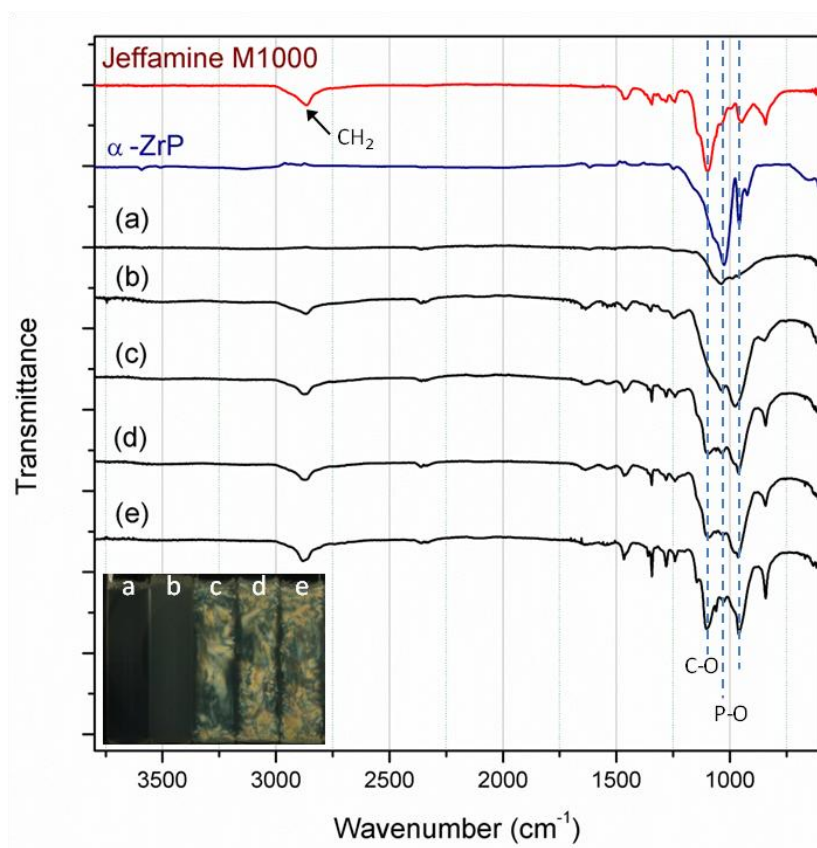
Figure 4.7. FTIR spectra of Jeffamine M1000, α-ZrP, ZrP with propylamine (ZrP/propylamine = 1/0.4) and increasing M1000 at molar ratio of (a) 0, (b) 0.4, (c) 0.8, (d) 1.2, and (e) 1.6. The inserted image is the upper suspension for the (a) ~ (b) samples after removal of non-exfoliated particles.
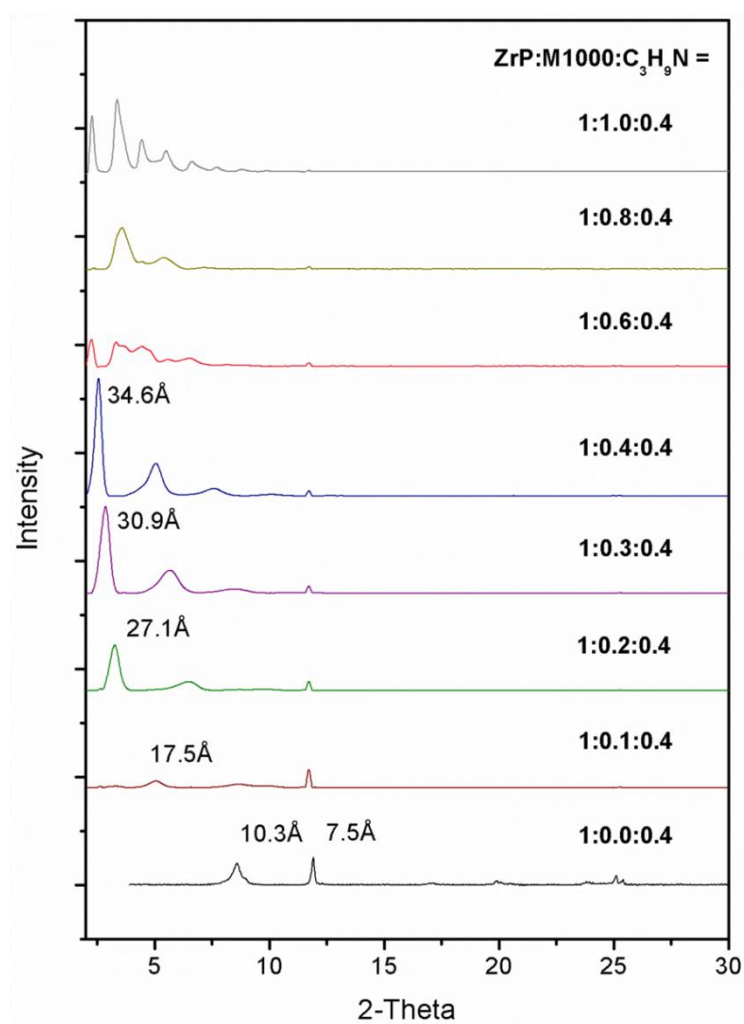
Figure 4.8. XRD patterns of ZrP intercalated or exfoliated by propylamine and Jeffamine M1000 mixture in aqueous. Nanoplatelets were dried and restacked on sample holder directly before testing.

Once the propylamine concentration has been determined, the effect of increasing dosage of M1000 was investigated. Figure 4.7 shows the FTIR spectrum of α-ZrP, M1000, and the cleaned (dialyzed) reaction products. The appearance of the band at 2873 cm^{-1} and 1104 cm^{-1} correspond to C-H stretch, and C-O stretch from the ether group,[147] respectively. Characteristic IR peaks of ZrP were reserved in the

intercalation/exfoliation compounds: 1024 cm^{-1} were attributed to the orthophosphate vibration mode, and the 961 cm^{-1} peak correspond to pyrophosphate group.[149-150] The increase in the relative magnitude of the absorbance band at 1104 cm^{-1} and 1024~961 cm^{-1} indicates the increase of M1000 exchanged or adsorbed onto the platelets as more M1000 was added. The exfoliated particles were separated from the non-exfoliated ones by centrifugation at 3500g for 5 min. The intercalated particles, still in stacks, formed pellets at the bottom of the tube while the exfoliated platelets stayed in the supernatant (insert in Figure 4.7). At intercalation ratio of 1:0.8 (ZrP:M1000) or above, the suspension became homogeneous with little solid residue.

Figure 4.8 shows the X-ray diffraction pattern obtained from dried films of intercalated/exfoliated ZrP. In the case when only propylamine was added, a second peak at 10.3 Å appeared due to intercalation of the short chain alkylamine, coexisting with the original 7.6 Å phase. Alberti et al.,[137] also reported similar behavior at this molar ratio of propylamine to α-ZrP, which contains a little over 50% of the 10.5 Å phase and close to 50% of the 7.6 Å phase. At small intercalation ratios of M1000, the 10.3 Å phase disappeared, and a gradual increase in inter-layer distance with M1000 concentration was observed. The presence of the small 7.6 Å peak indicates that a small amount of α-ZrP remain intact. The intensity of this peak continues to decrease as more M1000 was added, and eventually disappears at M1000/ZrP ratio higher than 0.8. A significant change in the scattering pattern from this point on indicates a jump in the amount of polymers in between the layers, signifying exfoliation. Notice here the inter-layer distance between restacked platelet structures, expected to be larger than 45 Å with
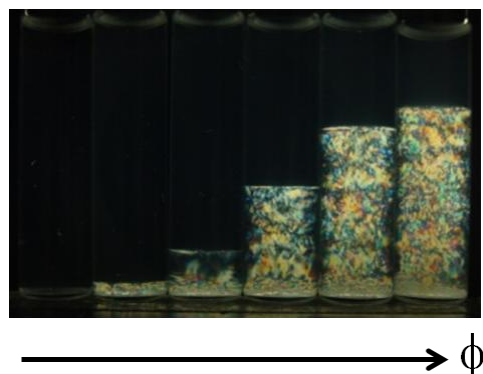
Figure 4.9. Polarized photograph of M1000 and propylamine exfoliated ZrP at increasing platelet concentrations (left to right).

the full intercalation of M1000, is out of the range of the detection limit of the instrument (minimum value of 2-Theta = 2 degrees, equivalent to d spacing of 44 Å).

From the visual observation of the samples (Figure 4.9), FTIR and XRD results, we have confirmed that by expanding the inter-layer spacing with proper intercalating agent, and fine tuning the composition of the intercalating compounds, effective exfoliation of high crystallinity α-ZrP with water soluble polymers can be realized. We have identified the optimal ratio between ZrP, Propylamine, and M1000 to be 1 to 0.4 to 0.8 or higher. Exfoliation using other hydrophilic Jeffamines, such as the ED2003 and ED 900, can be achieved in a similar fashion, all of which can be effectively exfoliated to colloidal platelet suspension that exhibits liquid crystalline properties (Figure 4.10).
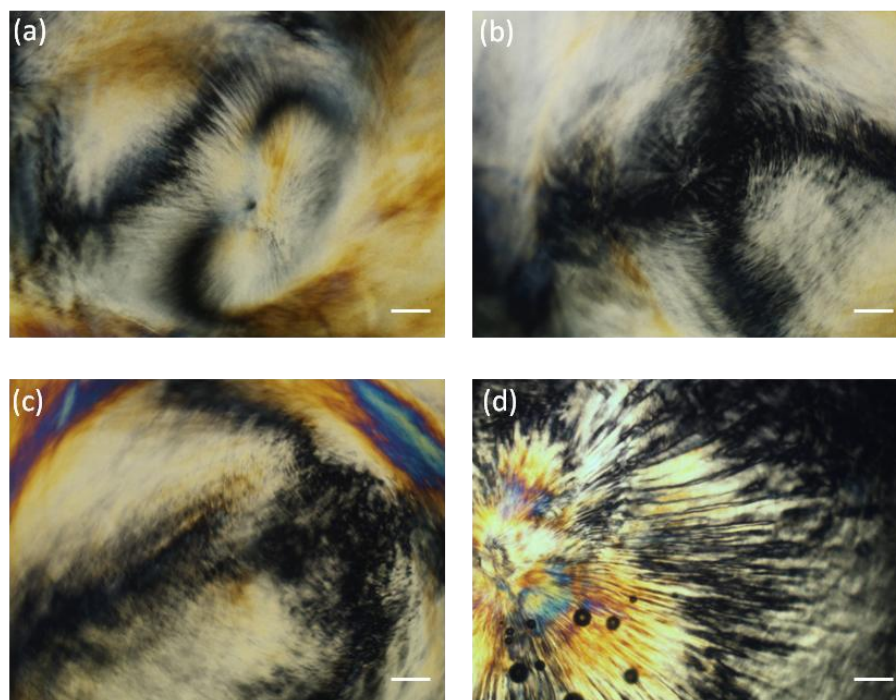
Figure 4.10. Liquid crystal textures of concentrated (> 10%) ZrP suspension exfoliated with mixture of polyamine and Jeffamines (a)-(b) M1000, (c) ED900, and (d) ED2003. Scale bars: 100 μm.

4.4.2 Suspension Stability Dependence on Counterions

To demonstrate the improvement of suspension stability, dialysis and osmotic stress experiments were performed. ZrP suspensions were kept inside a dialysis membrane, which is permeable to ions and Jeffamines while not permeable to the micron-sized particle. Dialyze the platelet suspension against a copious amount of water is an extreme method of dilution, in this case, creating a concentration gradient of the exfoliating agent across the membrane that would remove the unbounded/loosely bounded molecules. We found that under the regular dialysis treatment, suspension of TBA exfoliated platelets formed aggregated colloidal gels. The polymer (M1000) exfoliated particles, on the other hand, remain stable as nematic fluid under the same

condition (Figure 4.11). The reason for gel formation is believed to be the ionic exchange-related detachment of the loosely bounded TBA$^+$ from platelet surfaces, while the polymers containing protonated primary amine remain intact. Mechanism of the gel formation and the gelling behavior of ZrP platelets will be investigated in detail in the chapter to follow.
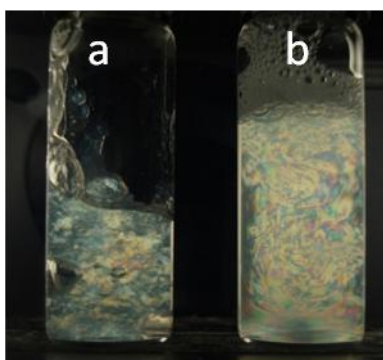
Figure 4.11. Suspension of (a) TBAOH and (b) Propylamine/M1000 exfoliated ZrP platelets after dialysis against deionized water.

4.5 Conclusions

In this chapter, we have demonstrated successful exfoliation of α-ZrP in aqueous media by acid-base reaction with a series of tetraalkylammoniums, including TMA$^+$, TEA$^+$, TPA$^+$, and TBA$^+$ hydroxides. X-ray diffraction of re-stacked solids from ZrP monolayers showed good agreement between the layer thickness and the cation size reported in the literature. The change in isotropic-nematic transition volume fraction decreases in the order of ZrP-TBA > ZrP-TPA > ZrP-TEA > ZrP-TMA (decreasing platelet thickness at fixed particle diameter, i.e., increasing aspect ratio), consistent with theoretical description of aspect ratio or particle anisotropy-dependent I-N transition.

This is, to our knowledge, the first report using direct exfoliation with different organic cations to systematically vary the aspect ratio of liquid crystal-forming colloidal disks. Liquid crystal transition boundaries were identified via sedimentation profile of platelet suspensions, clarifying the role of gravity on apparent nematic phase compression after phase equilibrium was reached. We experimentally confirmed the efficacy of reducing size polydispersity via liquid crystal fractionation in the I-N coexistence region. Finally, an aqueous based, sterically stabilized platelet system that demonstrates similar phase behavior as the charged one, but with improved stability, was developed.

CHAPTER V

LIQUID CRYSTAL AND GELLING TRANSITIONS OF CHARGED

PLATELET SUSPENSIONS: INFLUENCE OF ION EXCHANGE

5.1 Synopsis

Phase behavior of charged disk suspensions displays strong dependence on ionic strengths, as the interplay between excluded volume and various electrostatic interactions determines the formation of glasses, gels, and liquid crystal states. The various ions in natural soil or brine, however, could present additional effects, especially considering most platelet structures bear momentous ion-exchange capacity. In the chapter we demonstrate a novel observation of how ion exchange modulates and controls the interaction between individual disks, which contributes to unconventional phase transitions from gelled phases to fluidic liquid crystal phases upon increasing particle concentrations.

5.2 Introduction

Colloidal dispersions of charged anisotropic particles exhibit an intriguingly wide range of rheological properties and rich liquid crystal phase behaviors. The ability of non-spherical particles to undergo spontaneous disorder-to-order, i.e., isotropic-to-nematic (I-N), liquid crystal transition at high particle concentrations was first demonstrated theoretically by Onsager[28] as a purely entropy-driven process due to particle-shape anisotropy. Stable liquid crystal phases formed by plate-like particles were later confirmed by computer simulations.[32,39] In addition, disordered states, such as

gels or glasses, are particularly prominent in charged systems.[151-153] They were thought always to intervene with the observation of stable nematic phases, with the most notable example of non-reproducible I-N separation in hectorite suspensions observed by Langmuir.[25] However, research in the past decade has revealed the existence of nematic phases for selected natural and synthetic clays,[42,45,49] whose I-N transition occurred at concentration lower than the sol-gel transition point that is strongly dependent on the ionic strength of the solvent. To date, there seems to be little work showing the ionic strength controlled phase diagrams of charged, discotic suspensions that display both gel phase and stable liquid crystal phases. The detailed study here will elucidate gelation of discotic suspensions that readily form liquid crystal phases under normal conditions. These gels are vastly different from structures of nematic liquid crystal embedded in a secondary matrix, the so-called nematic gels.[154-155] The ability to precisely describe gel structure and its formation in such systems is of vital importance to their technological applications such as use as rheology modifiers and fillers in composite materials.

Aqueous suspension of high-aspect-ratio, charge-stabilized zirconium phosphate (ZrP) platelets prepared by exfoliation was recently shown to exhibit stable nematic alignment at low-volume fractions.[44] As with clay, the ion-exchange property of α-ZrP has long been exploited in applications such as nuclear waste treatments and kidney dialysis; hence, its structure and physiochemical properties are well characterized. In this chapter, we present the phase diagram of these equal-thickness platelets as a function of salt and particle concentrations. Different phases were distinguished and characterized with polarized imaging, rheology, and light scattering. We find that a strong specific

attraction induced by ion exchange leads to gelation of the suspension; conversely, with insufficient ion exchange, repulsive interactions remain dominant, drawing the system back to liquid crystal state.

5.3 Experimental Materials

ZrP monolayers were prepared according to the procedure described in section 2.2.4. The exfoliated platelets (with TBAOH) have an identical thickness of 2.68 nm.[134] Several batches (B1~B4) of particles were used in this study, and minimal variations in size and polydispersity were present (D= 1325 nm, polydispersity σ = 32% for B1 batch; D = 1093 nm, σ = 32% for B2 batch; D = 1485 nm, σ = 36% for B3 batch; D = 1431 nm, σ = 34% for B4 batch). Concentrated, stock suspensions were diluted with deionized water or salt solutions to obtain the desired particle concentrations and ionic strengths.

5.4 Results and Discussion

5.4.1 Effect of Organic Chloride Slat on I-N Transition

We investigated the influence of ionic strength on the I-N transition of ZrP suspensions. Tetrabutylammonium chloride (TBACl), a salt with an identical cation to the exfoliating agent, was chosen first to avoid complication of the system, and the samples were monitored through cross-polarizers. Figure 5.1a shows cross-polarized photographs of monolayer platelets at ten concentrations, increasing from left to right, suspended in 0- to 100- millimolar ionic strength solutions. For a fixed ionic strength, very dilute particle suspensions showed strong flow birefringence under cross-polarizers. At increased particle concentrations (in the I-N coexistence region), the suspensions

became permanently birefringent and exhibited nematic defects in polarizing microscopy (Figure 5.1b). Over the course of 48 hours, complete phase separation occurred for these two-phase coexistent samples into an upper isotropic and lower nematic phase, separated by a visibly sharp interface. Figure 5.1c gives a snapshot of the progressive increase of nematic volume fraction in the samples with the overall platelet weight fraction for varying ionic strengths. At fixed particle concentrations (weight fraction ϕ_w) within the biphase region, the nematic appears increasingly compressed with the increase of ionic strengths, a phenomenon anticipated as a result of the decrease in repulsion as is observed in clays.[51] The boundaries of the biphasic gap can be extrapolated by a nonlinear fit (due to wide polydispersity[44]) in Figure 5.1c to the height-concentration curve. Figure 5.1d summarizes the TBACl-dependent phase diagram: The lower boundary $\phi_{w,I}$ was essentially unchanged up to ionic strength of 10 mM; Full nematic phase $\phi_{w,N}$ was obtained at $0.011 \leq \phi_{w,N} \leq 0.014$ for ionic strengths below 1 mM, $\phi_{w,N}$ ~0.017 for 10 mM, and $\phi_{w,N} > 0.022$ for 100 mM (exact position not determined). This increase in $\phi_{w,N}$ with ionic strength is in qualitative agreement with the screening of electrostatic repulsion with ions. In the study of crystallization in suspensions of charged colloidal spheres, fluid-crystal coexistence increases with ionic strength to a maximum at the hard sphere limit.[156]
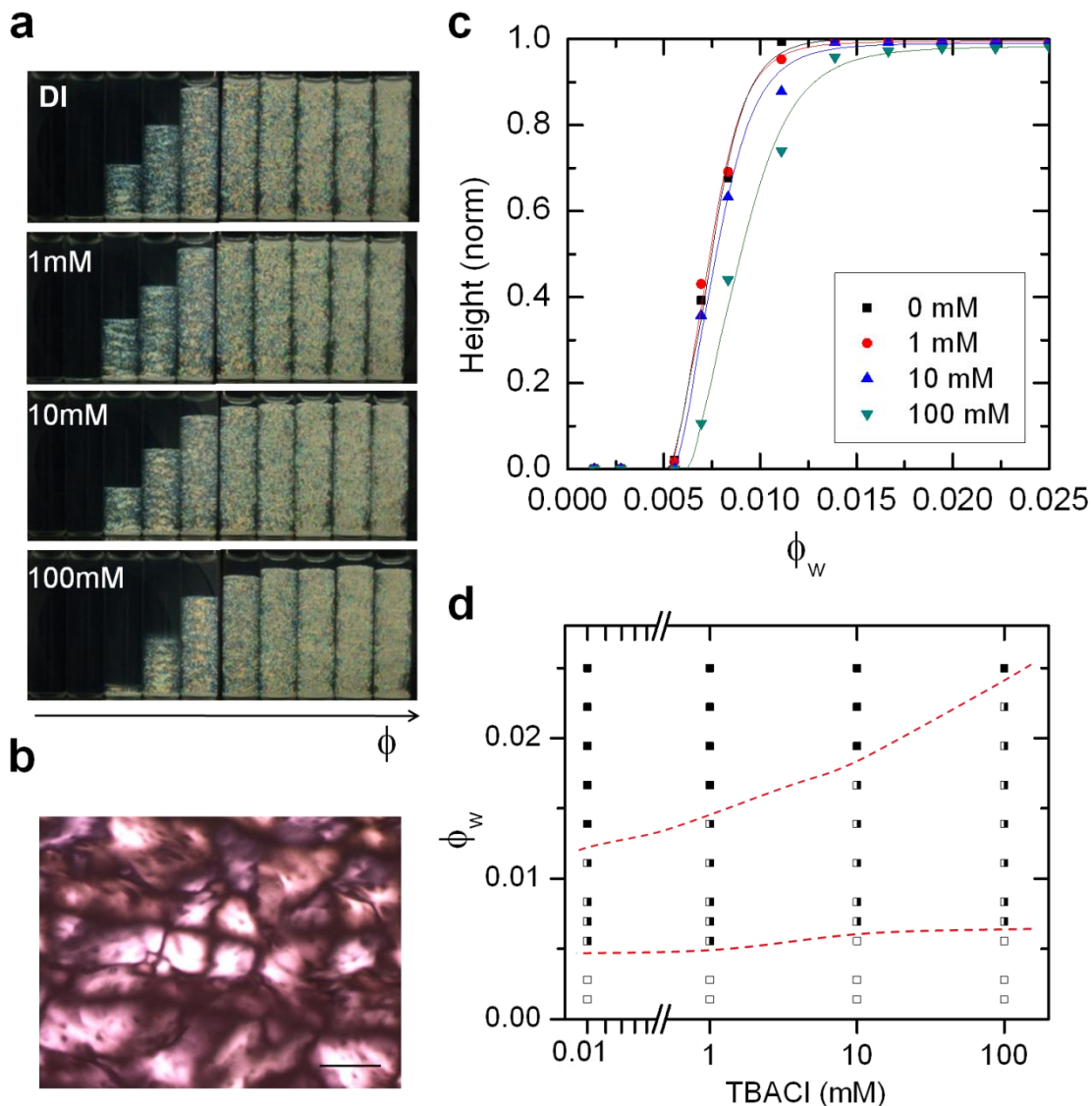
Figure 5.1. Influence of TBA salt concentration on ZrP platelet phase diagram. (a) Polarized light photograph of ZrP platelet suspensions at particle concentrations of 0.28, 0.56, 0.69, 0.83, 1.11, 1.39, 1.67, 1.94, 2.22, 2.50 %w/w in TBACl solutions. (b) Schlierin texture of a nematic suspension ($\phi_w = 2.12\%$, in DI). Scale bar: 150 μm. (c) Nematic height as a function of salt and particle concentrations. (d) Summarized phase diagram. Phase states include isotropic liquid (open rectangle), biphasic (half-filled rectangle), and nematic (filled rectangle) liquid crystals. Dashed curved outlines biphase region.

Theoretical calculations on infinitely thin hard platelets[39] have shown that I-N phase transitions occur between densities ρ_{iso} D^3 = 3.7 and $\rho_{nem}D^3$ = 4.0 for monodispersed suspensions, where ρ is number densitiy of the transitions and D, the platelet diameter. Since our system exhibits high polydispersity, it is reasonable to compare experimental with the theoretical values for polydispersed samples ($\sigma \sim$ 32%), whose densities are found to be $\rho_{iso}D^3$ = 3.5 and $\rho_{nem}D^3$ = 5.6 (according to ref[39]). Following van der Beek and Lekkerkerker [49], the relation between core volume fraction ϕ and number density for platelets of diameter D, thickness t, and polydispersity σ is

$$\rho\langle D\rangle^3 = 8/9\sqrt{3}\left(\langle D\rangle/\langle t\rangle\right)\left(1+3\sigma^2\right)/\left(1+\sigma^2\right)\phi. \tag{5.1}$$

Taking into account the geometrical factor after exfoliation (layer thickness increased by three-fold due to the attachment of TBA$^+$), we convert weight percents into disk ϕ values by an approximate density value of $\sim$1.8 g/cm^3. Eq. (1) yields dimensionless densities of $\rho_{iso}D^3$ = 2.1 and $\rho_{nem}D^3$ = 5.2 for our suspensions at zero ionic strength. The results are comparable to theoretical values; discrepancies might be due to platelet geometry or surface charges.

5.4.2 Gel Phase Formation with Sodium Chloride

In addition to liquid crystal phases, gelled phases occurred when a common salt—sodium chloride (NaCl)—was used to adjust suspension ionic strength instead of TBACl. Figure 5.2 presents the optical photographs of series of suspensions in 0 (as reference for salt-free phase diagram), 10, and 20 mM NaCl, providing preliminary evidence of gelled states, in which samples were able to retain air bubbles due to finite
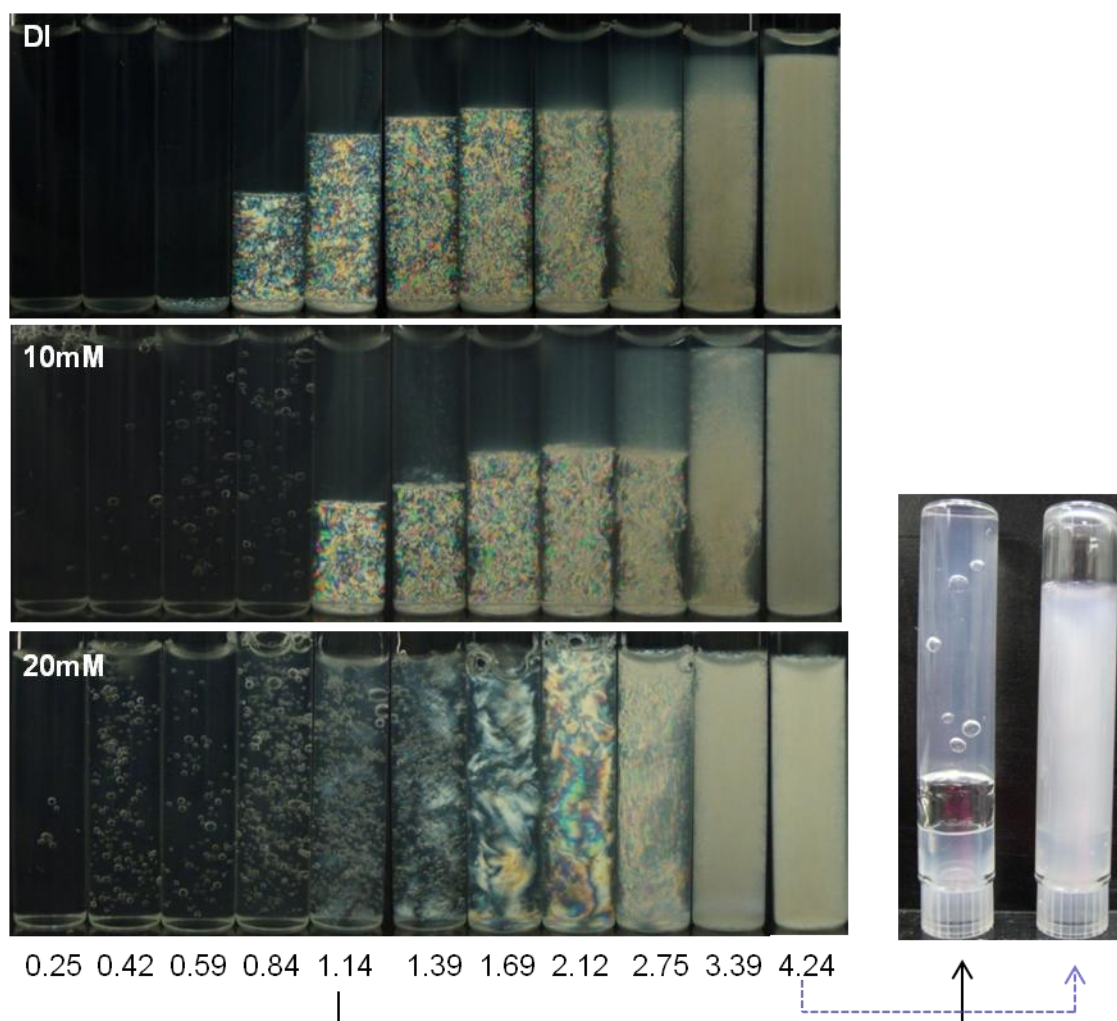
Figure 5.2. Polarized images of ZrP suspensions (B3 batch) in 0, 10, and 20 mM NaCl salt solutions. Left: Photograph of bulk samples at increasing platelet concentration (left to right, labeled conc. in %w/w). Right: regular light photograph of gel (left tube) and liquid crystal (right tube) sample under sample inversion test.

yield stresses. Gelled samples at platelet concentration below $\phi_w = 0.011$ for both 10 mM

and 20 mM ionic strength appeared isotropic; for 20 mM series, those whose

concentrations were in the range of $0.011 \leq \phi_w \leq 0.021$, on the other hand, displayed

strong birefringent textures. For 10 mM ionic strength series, re-entrance of stable liquid

crystalline phase was found at concentrations above 0.011. Biphasic samples (with clear
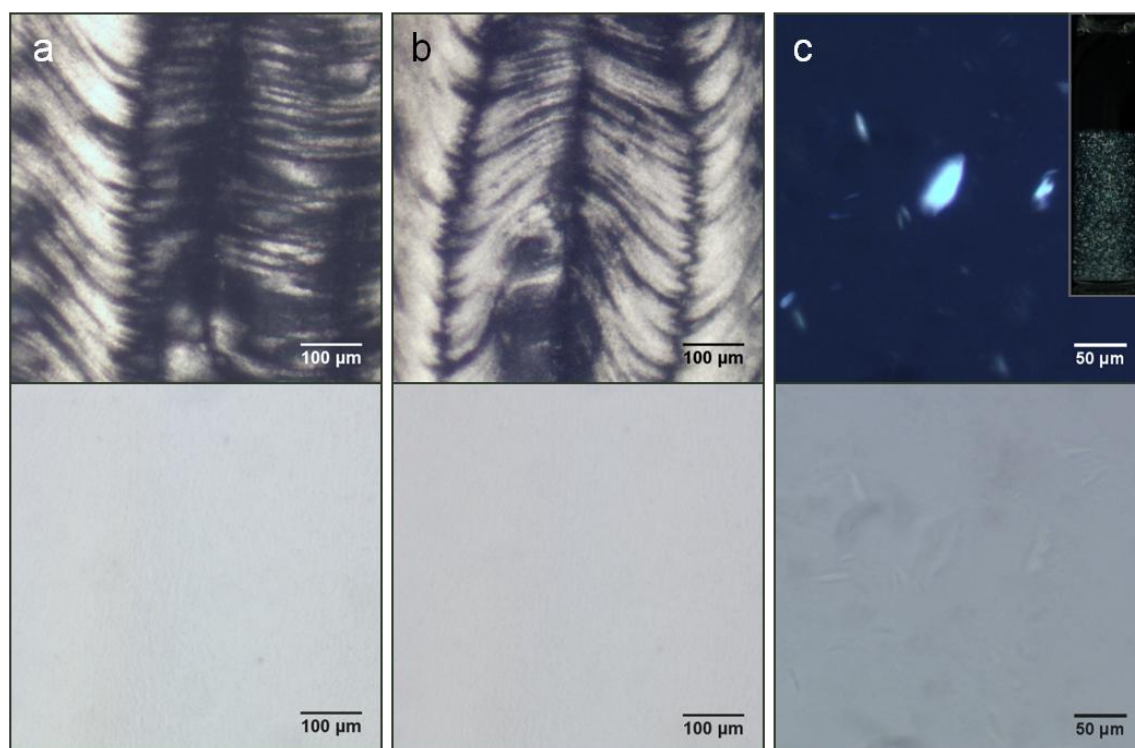
Figure 5.3. Cross-polarized (upper) and the corresponding bright field (lower) microscopy images of ZrP in liquid crystal (upper panel) and flocculated states. Sample compositions: (a) 4.24 %w/w suspension in 20 mM NaCl. (b) 4.24 %w/w suspension in 0 mM NaCl. (c) ≈0.2 %w/w suspension in high concentration acid. Insert in (c) is the photograph of flocculated sample (in 1 mL vial) viewed under cross-polarizers.

phase separation) were observed at $0.011 \leq \phi_w \leq 0.021$, within which the proportion of lower nematic phase increases with the concentration of particles. Full nematic fluid was obtained at $\phi_w \approx 0.028$. Similarly, for 20mM series, the suspensions appeared fluid again at $\phi_w > 0.021$, as shown via sample inversion test in Figure 5.2 (right). The nature of these higher particle and salt concentration samples is less obvious as they appear diffusive in bulk (path length ~9 mm) due to the high refractive index of zirconium phosphate. As flocculated samples could also appear birefringent in consequence of scattering from aggregated (anisotropic) clusters, it is important to demonstrate sample

homogeneity via bright-field imaging. The absence of optical contrast viewed in regular light verifies its homogenous nature, and the suspension can be recognized as liquid crystalline phase by the pronounced optical texture under polarized microscopy imaging, similar to that in zero ionic strength (Figure 5.3a,b). In the flocculated sample ($\phi_w \approx 0.2$ %, strong attraction induced by adding excessive HCl acid), the strong birefringence (high contrast against background) corresponds to particle aggregates (Figure 5.3c). Such type of optical contrast/property from flocculated samples is vastly different from the samples in the liquid crystal states.

5.4.3 Colloidal Gel Characeterization

Formation of gel structures were further verified and characterized with rheology and light-scattering measurements. Small-amplitude oscillatory shear experiments were carried out using a Parr-Physica MCR-300 rheometer with parallel plate geometry (25-mm plate diameter, gap of 0.5 mm) at 25 °C. The samples were pre-sheared at 500 s^{-1} and relaxed for 8 min. The elastic and viscous moduli G′ and G″ were measured at a strain amplitude of $\gamma = 0.02$ with angular frequencies from 0.01 s^{-1} to 100 s^{-1}. Unlike the cases when NaCl concentration is below 7.5 mM, where all the samples (in the particle concentration range prepared, < 15 wt%) appeared fluid, a dramatic increase in viscosity was observed when NaCl concentration reached 10 mM. The thickened samples were degassed via sonication and carefully loaded onto a rheometer for characterization. The selected strain amplitude ensured the testing be done within the linear viscoelastic region for all the gel samples, The measurements provided the basis of determining the sol/gel transition based on the evolution of G′ and G″ with particle concentration at different
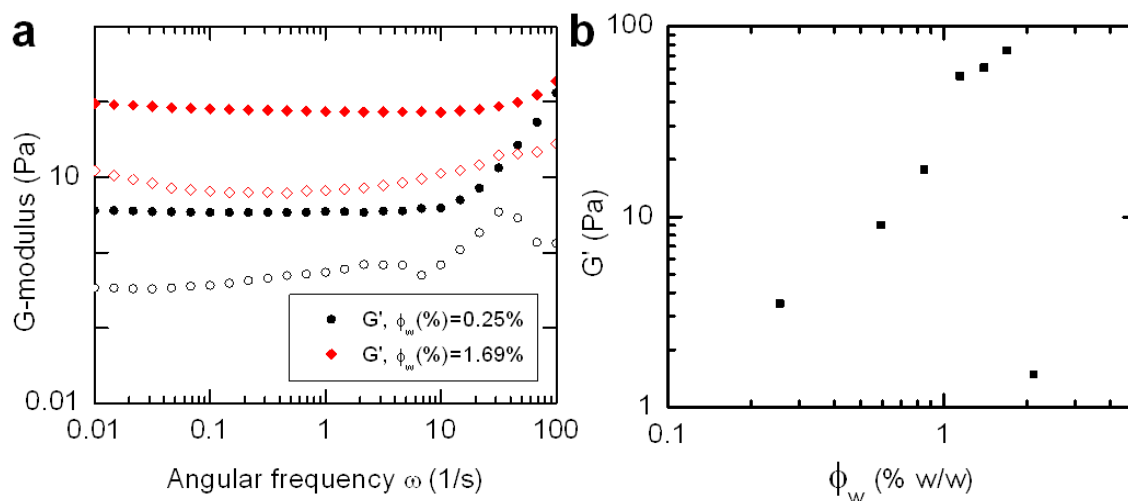
Figure 5.4. Rheology of B3 batch platelet suspensions in 20 mM NaCl. (a) Frequency response of storage (G′, solid symbol) and loss modulus (G″, open symbol) for ZrP gels at two different concentrations. (b) Evolution of the elastic modulus as a function of platelet concentration.

ionic strengths. Signals from low viscosity sol state samples ($0.011 \leq \phi_w$, 20 mM NaCl) are poor and too scattered to be meaningfully represented in the figures. Figure 5.4a presents frequency evolution of storage modulus G′ and loss modulus G″ of selected B3 batch samples at an ionic strength of 20 mM that demonstrates typical gel behavior: G′ is significantly higher than G″ and displays limited frequency dependence. At $\phi_w > 0.021$, both moduli are weak, indicating fluidification of the samples. Figure 5.4b summaries the elastic modulus G′ (value at 1 s^{-1}) as a function of ϕ_w, where the reduced positive dependency of G′ with particle concentrations is demonstrated. The result differs dramatically from previous studies on anisotropic colloidal gels,[157-159] whose storage modulus followed a power law dependence on reduced particle volume fraction $(\phi-\phi_0)^n$ at fixed ionic strength (n = 2.3~2.5 for clay suspensions, ϕ_0 is the critical ϕ above which

gel appears). At this salt concentration, the gel characteristic eventually disappeared at

$\phi_w > 0.021$.
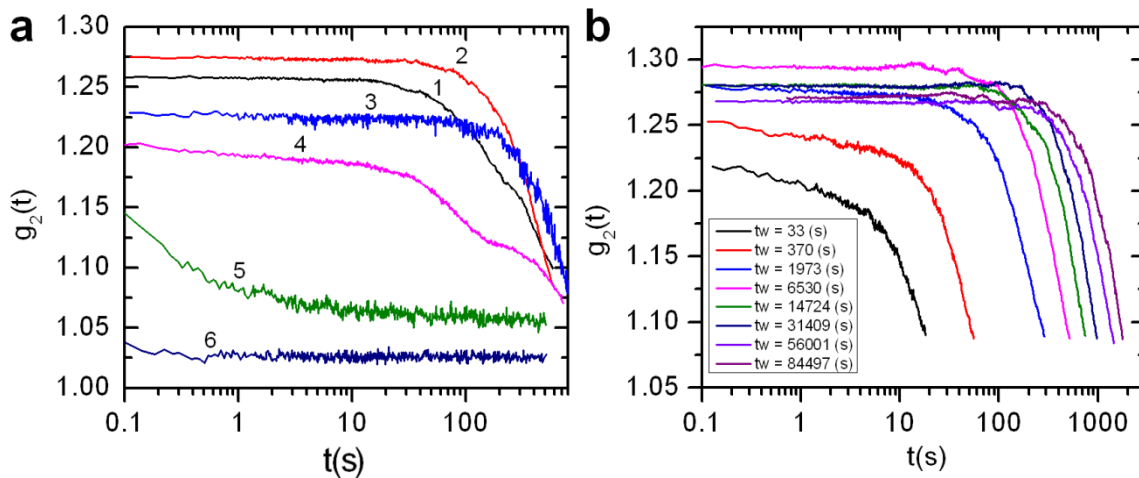
Figure 5.5. (a) Autocorrelation function versus t for ZrP (B4 batch) suspensions of varying concentrations (from 1 to 6, 0.36, 0.71, 1.07, 2.13, 2.84, 4.26 %) at a fixed NaCl salt concentration and aging time (~2 h). (b) Autocorrelation functions of sample number 2 at different aging time.

Multi-speckle diffusive wave spectroscopy (DWS) in backscattering geometry[160-161] was used to identify arrested/non-arrested structures. The samples were illuminated with a 633-nm laser, and the backscattered light was collected onto a CCD camera at 90 frames/s. The ensemble average autocorrelation function is obtained from

$$g_2(t) = \langle i_i(0)I_i(t)\rangle / \{\langle I_i(0)\rangle / \langle I_i(t)\rangle\} \qquad (5.\,2)$$

where I_i refers to the intensity of backscattering light at the ith pixel, which is a function of time. The correlation function g_2 quantitatively describes the similarity between two images at different times. In general, relaxation time (or decorrelation time) is defined as the time required for g_2 to decay to half its value at time zero. Slower decay of g_2 or

longer relaxation time indicates slower particle motions, a sign for restricted motion for frozen systems such as glassy materials and colloidal gels. Figure 5.5a shows g_2 versus time for six samples (B4 batch) at aging time around 2 h, with concentrations span through broader phase states than that included in Figure 5.4 — isotropic gel (sample 1 and 2), nematic gel (sample 3 and 4) , and fluidic liquid crystal phase (sample 5 and 6). Correlation functions of samples 1~4 showed significant long relaxation time, typical of arrested states. Dramatic relaxation-time reduction was apparent for higher concentration samples (5 and 6), confirming un-gelling transition when ϕ_w increased from 0.021 to 0.028 (B4 batch, 20 mM NaCl). Additionally, aging phenomenon (the evolution of the correlation function with time) was observed for gel-state samples (Figure 5.5b) while being absent for liquid crystal samples, providing corroborating evidence for the transition.

5.4.4 Phase Diagram as Influenced by Ion Exchange

The liquid crystal and sol-gel phase behaviors in NaCl solutions were evaluated using the above-described methodologies and mapped onto a two-dimensional phase diagram (Figure 5.6). At salt concentrations below 10mM, the offset of phase boundaries is qualitatively consistent with the TBACl case. In contrast to the TBACl system, where the dispersion appears stable up to 100 mM ionic strength, gelation occurred for NaCl concentrations larger than 10mM. The location of the gel region determined by rheology and light-scattering data infers unprecedented gel-to-liquid crystal transitions upon increasing particle concentration at fixed ionic strengths. Although arrested states are encountered frequently in charged platelet systems, the phase behavior of the NaCl-ZrP

system is different from the gelling behavior observed for most natural or synthetic clays, where the percolated networks expand throughout the entire sample with particle concentrations above the sol-gel transition.[45,157-159,162] The unique phase evolution pathway suggests an intrinsically different mechanism for the gelling behavior of ZrP platelets in the presence of NaCl.
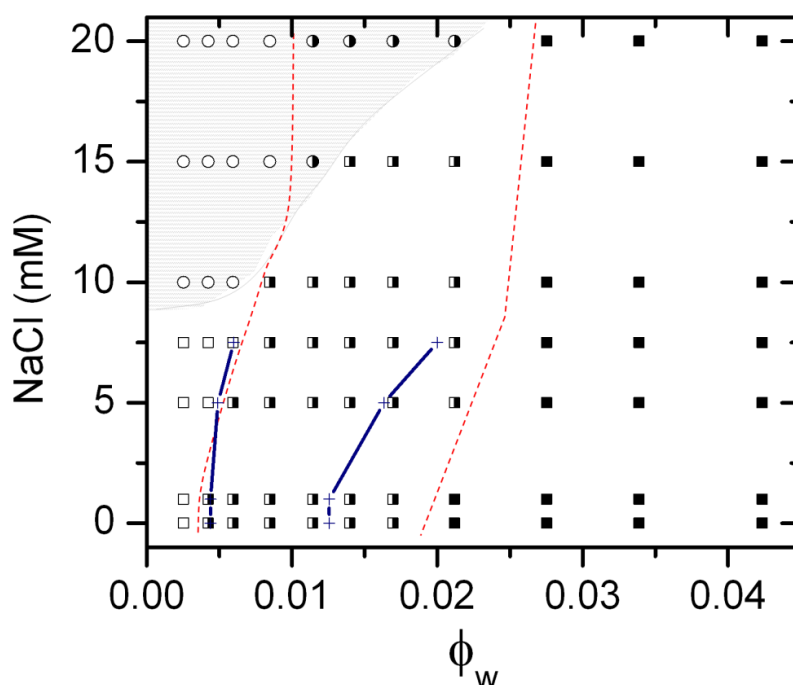
Figure 5.6. State diagram of ZrP platelet suspensions as a function of platelet weight fraction and NaCl concentration. Phase states for ZrP samples include isotropic liquid (open rectangle), isotropic gels (open circle), birefringent gels (half-filled circle), biphasic (half-filled rectangle), and nematic (filled rectangle) liquid crystals. Shaded areas represent the gelled phase, and the biphase region is outlined for both polydisperse (B3 batch, dashed lines) and more monodisperse (B2 batch, crosses linked with solid lines) samples.
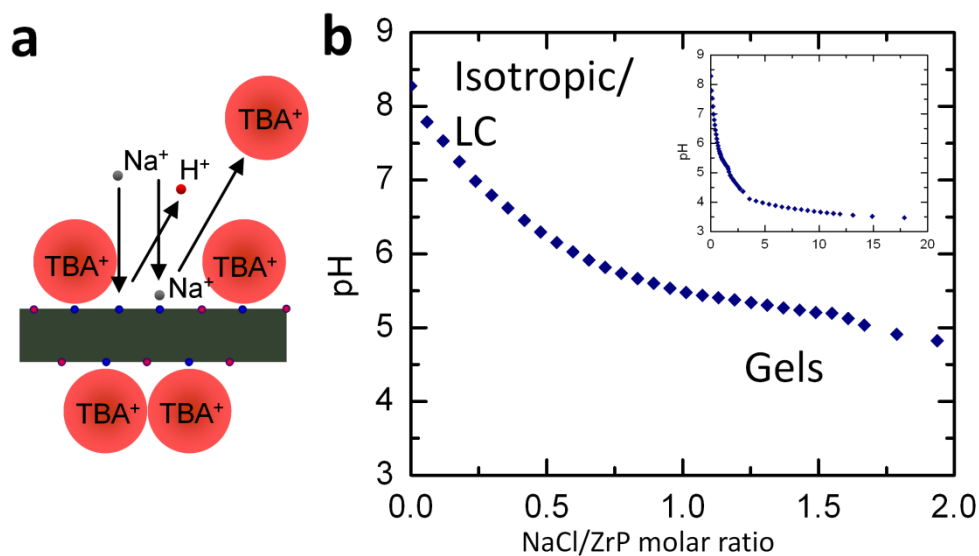
Figure 5.7. (a) Schematic of ion exchange process with Na$^+$. (b) Suspension pH evolution with added NaCl concentration. Insert: pH at broader NaCl/ZrP ratios.

To rationalize this unusual phase behavior, we take a closer look at the structure of the monolayer platelets, the origin of the gel phase, and how the surface charges and inter-particle interactions are modified with the addition of NaCl. Since the exfoliated monolayer platelet Zr(HPO$_4$)(TBAPO$_4$) consists of half-exchanged α-ZrP, with a layer of TBA$^+$ packing on the platelet surface and an underlying residual hydroxyl group in between each TBA$^+$, ion exchange could proceed in the presence of NaCl as Na$^+$ displaces the available protons or the loosely bound TBA$^+$ on the surfaces (Figure 5.7a). Release of the dissociated H$^+$ is into the suspension from the proton displacement process can be detected, as shown in Figure 5.7b a significant, continuous drop of suspension pH with the addition of NaCl until a plateau value of ~3.3 was reached. The suspension enters arrested state at approximate equal molar ratio of NaCl to ZrP, where the pH value drops below 5.5. Direct acidification using HCl also yield similar sol-gel

transition (data not shown), indicating that pH = 5.5 is the critical point where strong attraction arises, presumably in the face-edge direction due to opposite charges at the rims and faces of the platelets.

The specific face-edge attraction is due to the non-homogeneity of the charge distribution that arises from the α-ZrP crystal defects around the edges, where the phosphate groups are bonded to Zr through two or fewer oxygen atoms (as opposed to three for the basal plane). The dangling phosphate groups at the edges are most susceptible to hydrolysis (Equation 5.2), which is a side reaction common to exfoliation using a high concentration of base [163-164], transforming the chemical structure of the platelets (edges) into hydrous zirconia.

$$ZrP(HPO_4)_2 \cdot H_2O + nH_2O + 2xOH^- \leftrightarrow Zr(HPO_4)_{2-x}(OH)_{2x} \cdot (n+1)H_2O + x\,HPO_4^{2-} \quad (5.2)$$

The chemistry of the edges is thus apparently different from that of the faces: the isoelectric point (pI) of unmodified ZrP is between pH 2 and pH 3, whereas literature reported pI value for colloidal zirconia is above pH 6[165]. As the suspension pH decrease to under the pI of zirconia, the edges become positively charged while the basal plane remains negatively charged (due to lower pI value). The opposite charges on the edge and basal plane could attribute to the formation of gels, with face-to-edge configuration (Figure 5.8) as observed in clays. Surface charge redistribution at low pH may account for the possible platelet face-edge attraction, though direct evidence is still required to confirm the actual microscopic structure of the gel phase.
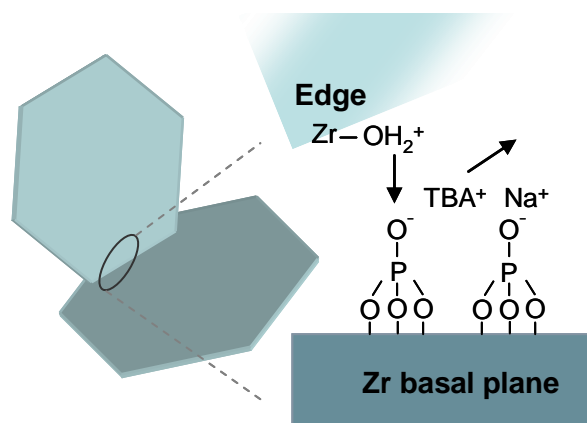
Figure 5.8. Hypothesized mechanism for specific face-edge attraction induced by ion exchange.

From the aspect of ion exchange, interpretation of the phase behavior as a function of NaCl concentration and packing fraction can now be refined as follows. At low ionic strength (0 to 7.5 mM), where the effect of surface charge alteration is minimal due to limited ion exchange (molar ratio of $Zr(HPO_4)(TBAPO_4)/NaCl \gg 1$), the influence of ionic strength can be considered to be an electrostatic screening one, similar to TBACl cases. At higher ionic strengths and low particle concentrations (NaCl >7.5 mM, $Zr(HPO_4)(TBAPO_4)/NaCl \leq 1$), ion exchange between Na^+ ions and surface protons reduces the suspension pH below 5.5, a transition from repulsive to attractive interactions takes place, causing gelled phases to appear. The decrement in suspension pH (i.e., concentration of protons released), controlled by the degree of ion exchange, is roughly proportional to NaCl concentration and inversely proportional to particle concentration according to the chemical balance of the exchange reaction. Therefore, for constant ionic strength, the degree of ion exchange decreases with increasing particle volume fraction (less pH reduction), which leads to an overall weaker attraction at

higher particle concentrations. This explains the gel-to-liquid crystal transition upon increasing platelet fractions that's consistent with the generally trend of jamming phase transitions (as change in interaction potentials).[166]

The concept of jamming phase transition is used to describe jamming transitions for attractive colloids. The critical liquid-gel transition boundaries are formulate as[166-167]

$$\phi_c = \phi_0 \exp\left(- U/\alpha k_B T\right) \tag{5.3}$$

where U is the attractive interparticle energy, ϕ_c is the transition volume fraction and α is the coefficient of order unity. The attractive interparticle potential (U) is, as we reiterate from the previous paragraph, not a fixed value at constant ionic strength. Instead, U increases with increasing NaCl concentration strength (at fixed ϕ_w) and decreasing ϕ_w (at fixed ionic strength) due to ion exchange. As a consequence, the transition from liquid to gel-like behavior can be achieved by either increasing attractive interparticle energy (U) at constant ϕ or vice versa. This explains the positive slope of the gel-liquid crystal transition (boundary line) within the framework of interaction-controlled gel transition.

5.5 Conclusions

In summary, we have studied the ionic strength dependent phase diagram of ZrP monolayer platelets, and validated the use of ion exchange to induce anisotropic interactions among individual platlelets. Liquid crystal states and arrested states were identified and confirmed via polarized imaging, rheology and diffusive wave scattering techniques. Unlike regular clay suspension cases, fluidization occurs at increasing particle concentrations for (NaCl) ionic strength above $\approx$ 8 mM, where low-volume fraction gels started to form. The gelling transitions were shown to depend strongly on

suspension pH (consequence of ion exchange at different NaCl/ZrP ratios), a parameter expected to influence charge interactions. The results offer a novel observation of the gelling behavior of charged discotic suspensions as ion exchange (pH) -modulated interactions come into play. Our work opens up new routes to the formation of discotic colloidal gels, and the comparison with other charged platelet systems should contribute to a better understanding of the role of ion exchange that is fundamental to charged discotic materials.

CHAPTER VI

DISCOTIC LIQUID CRYSTAL AS MOLECULE GONIOMETER

6.1 Synopsis

Suspension of high aspect ratio ZrP nanoplatelet is an alternative discotic media suitable for biomolecule alignment. The central issue that hinders the usefulness of ZrP nanoplatelet is the biocompatibility and the suspension stability at low pH. This section reports lipid layer assembly on exfoliated ZrP platelets. Two common strategies for supported lipid bilayer formation on solid substrates, namely supported lipid bilayer and lipid monolayer formation were implemented. The use of electrostatic-induced attraction between liposomes and nanoplatelets to fabricate lipid-ZrP assembly were ineffective, and disordered lipid-platelet aggregates were formed; Lipid monolayer deposition on hydrophobically modified ZrP were successful in forming stable aqueous suspension of lipid-ZrP complex. Physical limitations for fabricating stable suspensions of phospholipid decorated ZrP nanoplatelets were identified.

6.2 Introduction

Ordered liquid crystals media creates a director filed which can provide net alignment for biomolecules dissolved in solution. This property of discotic media has revolutionized certain fields in biophysics, specifically in the determination of solution structures of biological macromolecules by NMR residual dipolar coupling.[168-170] While the technology has been relying mainly on liquid crystals assembled from discotic lipid disks (i.e. bicelles, Figure 6.1a),[2,171-172] universally applicable, robust system at lower

material cost is still required. Lipid bicelles are intrinsically unstable since the disk-shaped assemblies rely on a delicate lipid phase behavior that is disrupted easily by temperature, pH, or the presence of other soluble molecules. Other systems, such as phages, mineral liquid crystal, and cellulose crystals[173-174] has also been proven suitable for such application. ZrP nanoplatelet is a perspective candidate as novel molecular goniometer since its suspension display nematic alignment at low particle concentrations ($\phi_{w,I}$ < 1 % compared to 30 % used in DMPC/DHPC bicelles).

Lipid/particle assemblies (lipid shell around solid particles) combine the properties of the colloidal core and the biocomopatibilty of lipid vesicles. In general, Supported lipid bilayer formation (Figure 6.1b) on colloidal particles[175] follows a similar procedure and guidelines as lipid layer formation on planar substrates.[176] Many factors dictate the way supported lipid bilayers are formed on hydrophilic substrates. For example, ionic strength can facilitate the adsorption of like-charged vesicles by screening electrostatic interactions.[177] Another effective surface modification strategy, lipid monolayer deposition or supported hybrid bilayer[178] is governed by hydrophobic interactions.

In this chapter, we adapt both strategies for ZrP surface modification with lipids. First, we describe charge interaction-directed assembly of lipid bilayers onto exfoliated, hydrophilic ZrP platelets. Next, hydrophobically modified ZrP was prepared, on which lipid monolayer was successfully assembled. FT-IR spectrum showed successful grafting of long chain hydrocarbon onto exfoliated ZrP layers, and the suspension stability in organic/water phases confirmed the hydrophobic character. Additionally, the

hydrophobic modification resulted in self-assembly of ZrP monolayers into lamellas (size in the order of 10~100 μm). The results provide a different aspect on ZrP monolayer functionalization.
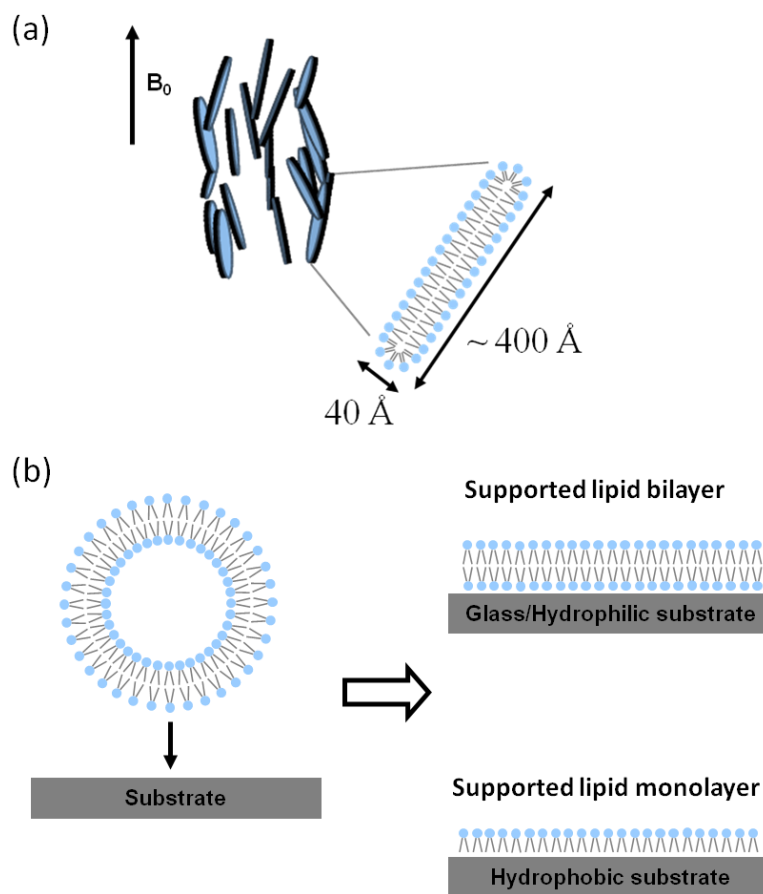
Figure 6.1. Schematics of (a) lipid bicelle alignment induced by external magnetic field, and (b) supported lipid layer assembly on hydrophilic and hydrophobic substrates.

6.3 Materials and Methods

Hydrophilic ZrP monolayers were prepared by standard exfoliation procedure described in section 2.2.4. Hydrophobically modified ZrP was prepared by covalently

linking a long chain hydrocarbon (C_{18}) with isocyante functionality to exfoliated ZrP surfaces using the method described in section 2.2.5.

Small unilamellar vesicles (SUVs) for vesicle fusion were prepared by extrusion method.[179] First, an appropriate amount of different lipids (in Chloroform) were mixed in a glass vial. Next, the solvent was evaporated with a stream of nitrogen and the lipids placed into a vacuum for a couple hours to remove all traces of the organic solvent. The dried lipid film was then reconstituted with deionized water for 1~2 h until a hydrated white cloud appears. The mixture was subjected to 10 freeze thaw cycles using a water bath (65 ℃) and liquid nitrogen (-196 ℃) to break multilamellar lipid vesicles. Finally, the liposome dispersion was passed through a Mini-extruder holding track etch membrane filter with pore size of 100 nm. A new filter was exchanged after five passes. The resulting size of the SUVs was slightly larger than the membrane pore size, as found with dynamic light scattering. The lipid composition of slightly negatively charged vesicles was 100% DOPC (ziwitter ionic lipid) and 0.03% NR-DHPE (negatively charged lipid dye); Composition for negatively charged vesicles was 60% DOPC, 40% DOPG (negatively charged lipid) and 0.03% NR-DHPE.

Supported lipid bilayer on hydrophilic particles was formed by standard vesicle fusion technique.[176,180] The prepared SUV spreading solution was combined with particle suspension at volume ratios that ensure at least 2-fold excess of lipids (total bilayer lipid headgroup area versus surface area of particles). Supported lipid monolayers were prepared following procedures of alkanethiol-phopholipid hybrid bilayer on gold shells.[181] A lipid mixture (pre-dissolved in isopropyl alcohol) was added

to a suspension of hydrophobic particles in 1:3 propanol-water solution. The mixture was then immersed in a sonication bath at 35 ºC, well above the phase transition temperature of the DOPC (T_m = -20°C) and DOPG (T_m = -18°C) lipid. The mixture was then cooled down to room temperature and centrifuged at 1000 rpm for 10 min. The supernatant was removed and the assemblies re-dispersed in water.

6.4 Results and Discussion

6.4.1 Physiochemical Aspect of Lipid/ZrP Platelet Assemblies

While the formation of supported lipid bilayers on silica particles or glass surfaces can be achieved for liposomes with both positive, neutral, and negative charges via the adjustment of deposition conditions (i.e. ionic strength of the solvent to screen any electrostatic repulsion between SUVs and the substrate),[177,182] fusion of positively charged liposomes onto exfoliated ZrP monolayer was not investigated due to their like-charge characteristic. Ionic solutions, necessary for like-charged liposome to come into contact with the substrate, flocculate ZrP nanoplatelets at tens of millimolar (also dependent on particle concentration, as described in chapter V). Figure 6.2 demonstrates the effect of SUVs' formulation on the assembly, where vesicles with close to zero charge (DOPC/NR-DHPE) and negative charge (DOPC/DOPG/NR-DHPE) were tested. Although both lead to aggregated structures (Figure 6.2b,c compared to Figure 6.2a), the cluster size was clearly reduced for vesicles with higher surface charge. This trend is in agreement with previous reports,[183] where the size of associated lipid-particle structures increases with decreasing vesicle surface charge density at fixed vesicle-to-particle

surface area ratio. Additionally, the small aggregates cannot be re-suspended after washing cycle by centrifugation (Figure 6.2d,e).
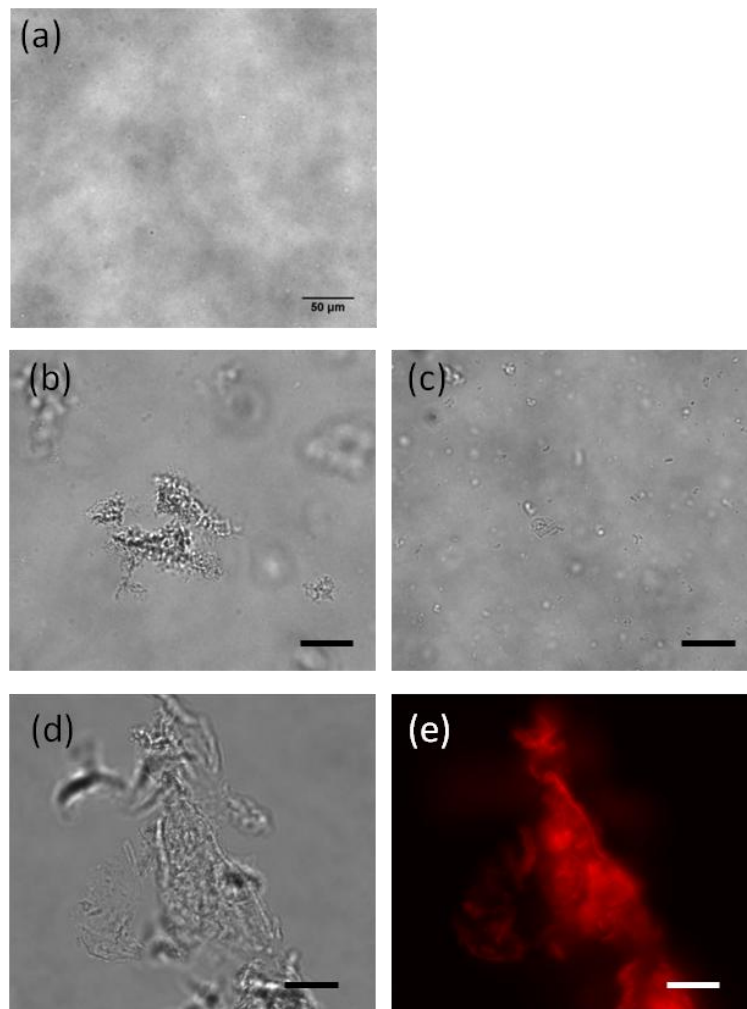
Figure 6.2. Microscopy images of (a) exfoliated ZrP platelets, (b) exfoliated platelets with DOPC/NR-DHPE liposomes, and (c) exfoliated platelets with DOPC/DOPG/NR-DHPE liposomes. (d) and (e) are the bright field and the corresponding fluorescent images of ZrP with DOPC/DOPG/NR-DHPE shown in (c) after excess liposome removal.

Under these experimental conditions, the liposomes functioned as coagulating agents, building disordered platelet-liposome aggregates. For the liposomes to act as

stabilizers (uniform lipid bilayer coating on individual platelets), one possible solution is to increase the liposome concentration even further during the assembly.[183-184] However, this imparts the system very expensive due to the extremely large specific surface area of high aspect ratio disks, and thus high consumption of vesicles. The reduction of materials requires for order phase formation (compared to bicelles) would then be rendered futile in compensation to the large of amount of lipids required. An alternative lipid surface decoration method — hybrid lipid bilayer, is thus pursued as follows.

6.4.2 Hydrophobic Surface Modification and Lipid Monolayer Assembly

Surface modification of ZrP monolayer was achieved by chemically grafting a long chain hydrocarbon (C_{18}-isocyanate) to the surface of exfoliated α-ZrP. Figure 6.3 indicates successful chemical modification of ZrP layers: disappearance of the reactive functional group (isocyanate, IR peak at 2267 cm^{-1}), appearance of peaks at 1568~1610 cm^{-1} from urethane linkage (reaction product of hydroxyl and isocyanate groups) and 2846~2918 cm^{-1} (C-H stretch), with the preservation of the characteristic orthophosphate and pytophosphate peak (1024cm^{-1} and 961cm^{-1}). The modified ZrP, denoted as ZrP-C_{18}, with the long alkyl chains on the surface of the particles is highly hydrophobic. In contrast to unmodified, exfoliated ZrP platelet, which is stable in water (Figure 6.4a) or methanol but not in organic solvents, ZrP-C_{18} can be readily dispersed in organic solvents. Figure 6.4b demonstrates the favorable partition of ZrP-C_{18} in the upper organic phase when mixed with water (lower phase). It was only dispersible in water when lipid monolayer was assembled on the surface, as shown in Figure 6.4c a homogenized sample.
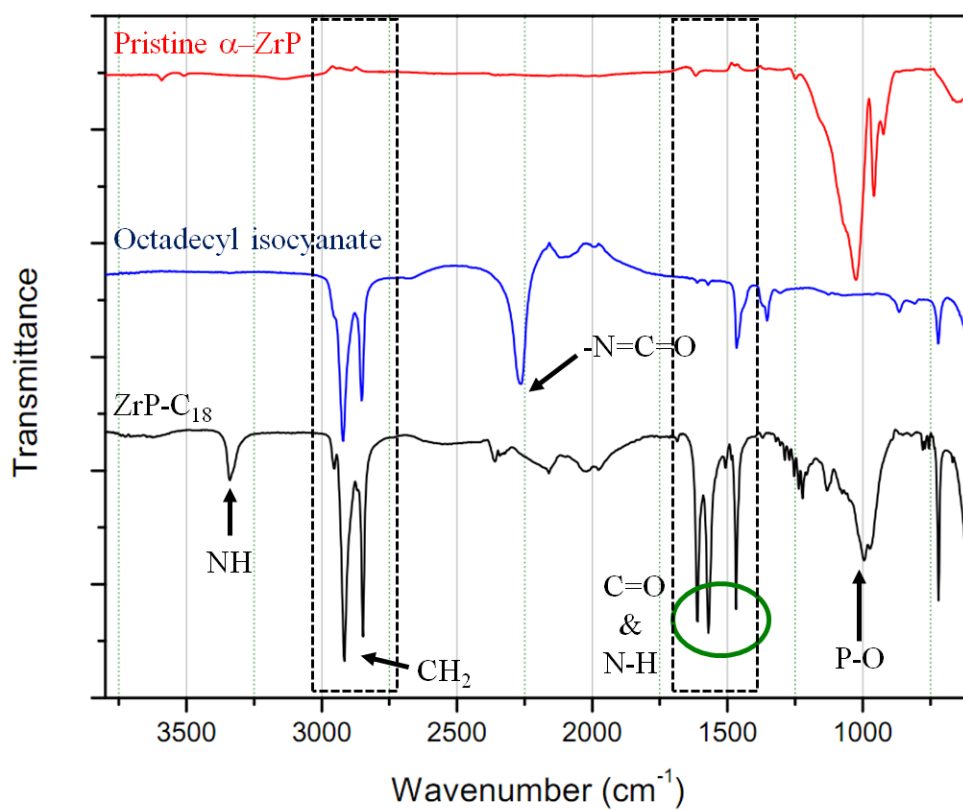
Figure 6.3. FTIR spectrum of unmodified ZrP, octadecyl isocyanate, and the reaction product ZrP-C$_{18}$.
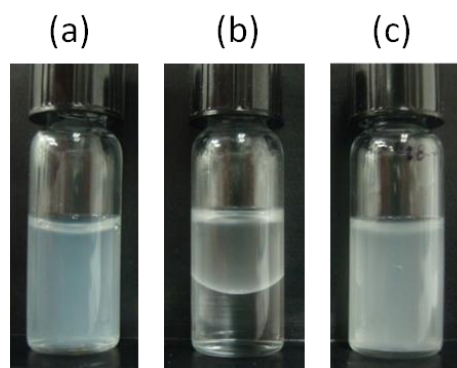
Figure 6.4. Dispersions of (a) exfoliated ZrP platelets in water, (b) ZrP-C$_{18}$ platelets in toluene/water solution, and (c) Lipid-covered ZrP-C$_{18}$ platelets in water.

6.4.3 Hydrophobic Assembly of ZrP Platelets

Upon closer examination of the modified ZrP compound, it appears that they are no longer single-layered, individual platelets as the ones shown in Figure 6.2a. Instead, ZrP-C$_{18}$ are thin, rod-like assemblies that are highly birefringent (Figure 6.5). Deposition of lipid monolayers on the assemblies did not change the morphology of the structures, but merely enhanced the dispersibility in polar solvents. SEM images (Figure 6.6) of dried ZrP-C$_{18}$ show many thin lamellas with length of up to approximately 110 μm and width from several to around 15 μm, a complete morphology transformation from the gel structures (Figure 6.6a) prior to reaction. High magnification image (Figure 6.6d) of the corner of a single lamella suggests that the lamellas are layered structures consists of stacks of individual platelets.
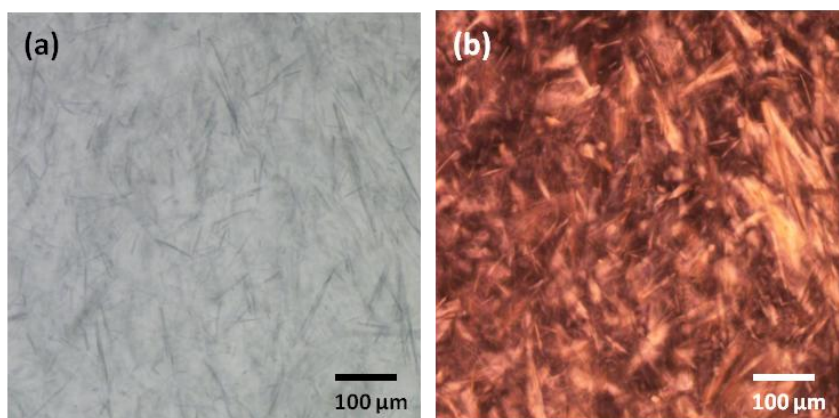
Figure 6.5. (a) Bright field and the corresponding (b) polarized microscopy images of hydrophobic ZrP-C18 assemblies in toluene.
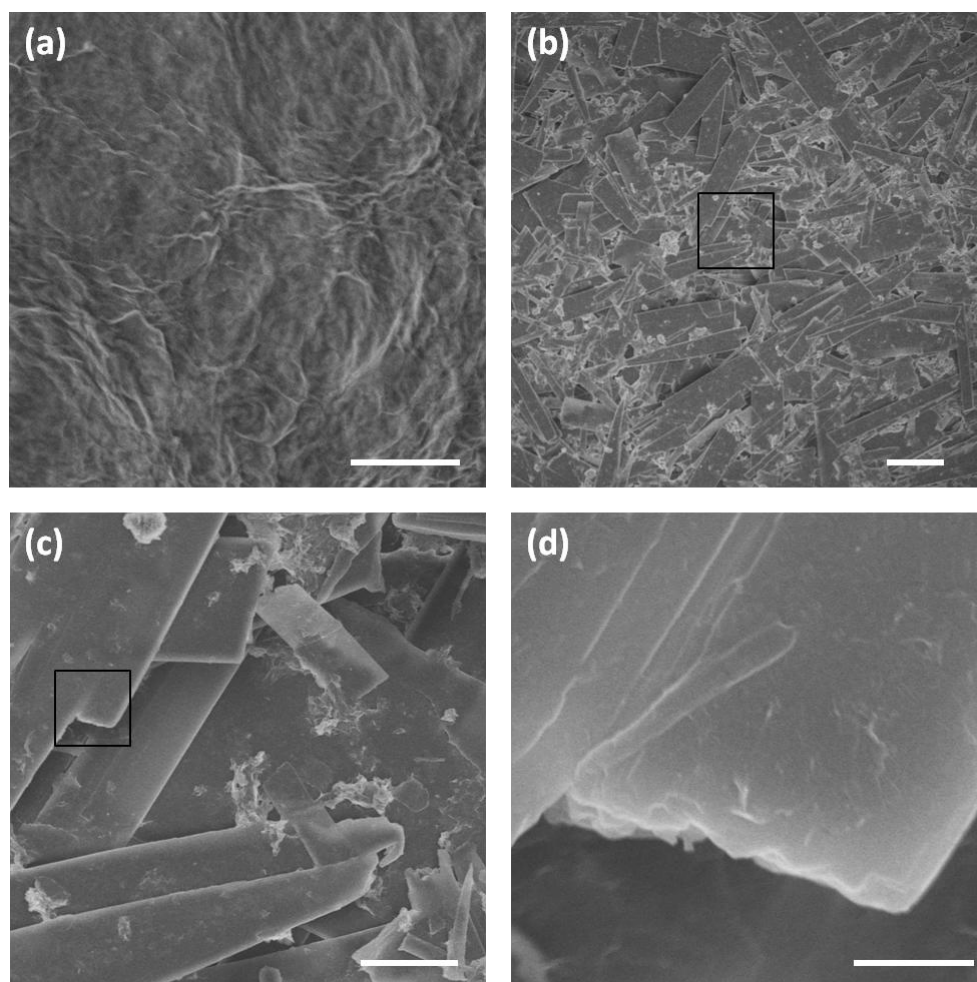
Figure 6.6. SEM images of (a) dried, amorphous ZrP gel (scale bar = 5 μm), (b) restacked ZrP-C$_{18}$ structures at low magnification (scale bar = 20 μm), and the same sample at higher magnifications with scale bars: (c) 5 μm and (d) 500nm.

X-ray powder patterns were collected on materials dried overnight in a 60 ℃ oven. Figure 6.7 shows the XRD pattern of ZrP-C$_{18}$ lamellas and unreacted α-ZrP. It is not surprising to see the disappearance of the 7.6 Å peak that correspond to the interlayer distance of α-ZrP in the ZrP-C18 pattern since the material was exfoliated and gelled (amorphous, data not shown) in the first step of the surface modification (section 2.2.5). The XRD pattern and the structural parameters gave another strong evidence of the

layered structure of ZrP-C$_{18}$. The multiple peaks and the doublet in the scattering pattern indicate that the material is not a pristine crystal like the α-ZrP, but a layered structure with domains or highly ordered regions. The main diffraction peaks (002) are at 2.46° and 2.71°, corresponding to a interlayer spacing of 35.9 Å and 32.6Å. The doublet at 7.28° (12.1 Å) and 7.54° (11.7 Å) are the secondary diffraction peaks. The interlayer distance of the ordered phases are shorter than that predicted for intercalated compound with n-alkylamine (CH$_3$(CH$_2$)$_{n-1}$NH$_2$)of the same chain length: the interlayer spacing d depends linearly on n, following the relation[79] d (Å) = 10 + 2.22 n. Interlayer spacing for n = 18 (octadecyl) turns out to be 49.96 Å, which is much larger than the values measured in the ZrP-C$_{18}$ lamella.
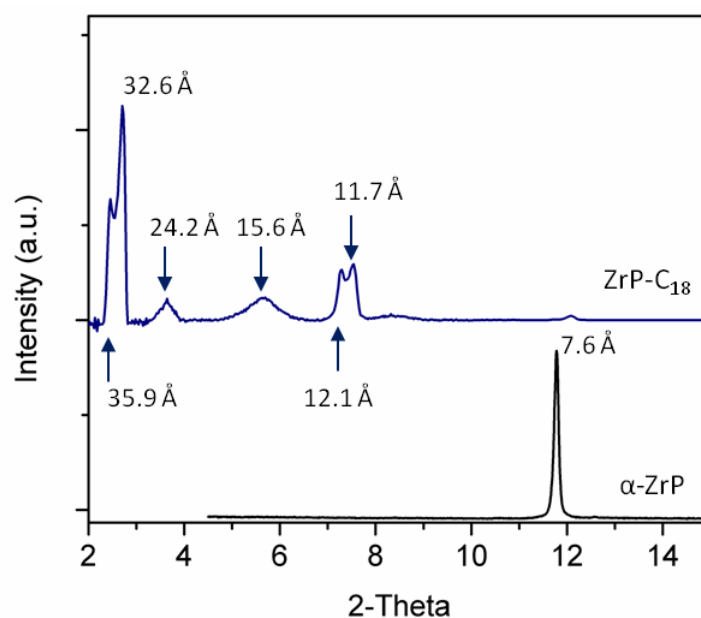
Figure 6.7. XRD pattern of modified (ZrP-C$_{18}$) and unmodified (α-ZrP) ZrP solids.

6.5 Conclusions

In this chapter, we described the two schemes of ZrP surface decoration with phospholipids — vesicle/hydrophilic platelet assembly and lipid/hydrophobic platelet hybrid in the initial goal to fabricate robust, biocompatible ZrP monolayers for biophysical applications. The former method was identified to be inefficient as the optimization requires large quantities of lipid materials, and the type of lipids is limited due to the fact that bilayer assembly on exfoliated ZrP was mediated by charge interactions (ionic solution was avoided due to ion exchange induced aggregation, see chapter V; spontaneous liposome adsorption occurs only when the surface charge is opposite to that of the substrate). On the other hand, successful self-assembly of lipid monolayer on hydrophobically modified ZrP was demonstrated as the compound became hydrophilic and was stabilized by lipids in water, yet strong van der Waals attraction between the grafted alkyl chains on the high surface area platelets lead to the formation of ZrP partially ordered lamella. Experimental results showed that the derivation of lipid coated, individual platelets suffered from various physical constrains. The discovery of the new class of layered ZrP compound (ZrP-C$_{18}$) may inspire future investigation on the morphology of such inorganic-organic hybrids and further the understanding of hydrophobic, platelet-platelet interactions.

CHAPTER VII

EMULSION CONFINED DISCOTIC SUSPENSIONS
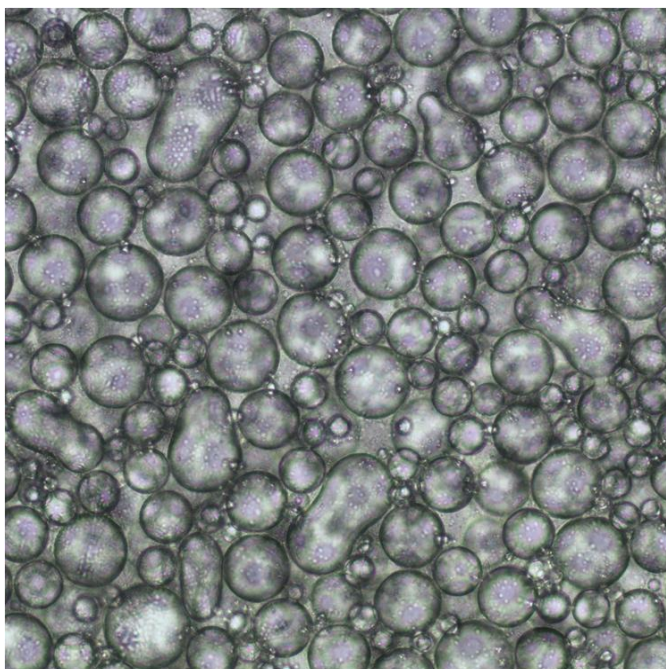
Figure 7.1. Pickering emulsions stabilized by surfactants and nanoplatelets.

7.1 Synopsis

Confinement of colloidal discotics in droplets is of great interests due to its analogy to the emerging field of liquid crystal ordering in confined geometries. In order to create stable capsules for platelet suspensions, the complexity of mixed surfactant-platelet systems was investigated. Although non-functionalized platelets are ineffective emulsifiers, synergistic effect between surfactant and colloidal particles led to the formation of destabilized, partially coalescent structures (Figure 7.1). Drying and buckling transition of emulsion droplets revealed the increasing adsorption of platelets onto the interfaces with increasing particle concentration. Manipulation of platelet

surface chemistry enabled the formation emulsions with improved stability, and successful encapsulation of high concentration discotic suspension was achieved.

7.2 Introduction

Geometric confinement of molecular liquid crystal within micro-sized spheres or shells has been shown to form a range of defect and topologies.[185-186] The change in defect structures could be triggered purely on a geometry basis or by varying boundary conditions.[187-188] Applications of liquid crystals droplets, which utilizes the stimuli-responsive optical properties (e.g. sensing applications), often rely on the control of ordering at the interface, directed by surface anchoring[189-190] or most recently the coupling between bulk liquid crystal and molecules at the interfaces.[191] In addition to I-N transitions, studies on N-S transition in spherical shells, which lead to more complex internal structuring, have also been conducted[192-193]. Research on phase transitions in confined geometries, especially for phase states with additional positional ordering (i.e. smectic, columnar, or other lamellar phases) is still a growing field. So far, little attention has been devoted to phase transition of colloidal discotics in confinement. Ordering behavior of platelet particles in spherical geometries has not yet been reported, and the inherent size scale of colloidal mesogens is expected to have an impact on the understanding of ordering in confinement.

Since the phase transition of discotic colloids is induced by the increased in particle packing fraction, the ultimate goal of this chapter is to establish a stable confinement system for discotic suspension at a wide range of concentrations, where multiple liquid crystalline phases can be probed. Despite the intrinsic behavioral

differences, surfactant molecules and colloidal particles could both function as stabilizers for droplet interfaces.[194] Synergistic effect in mixed surfactant-particle systems may or may not be advantageous to emulsion stability, and is highly dependent on the surface properties of the particles.[195-196] In the case where nonionic surfactant are used (i.e. no adsorption on to hydrophilic particles), assuming the particles favors adsorption onto the interface, it is likely that the particles and surfactants will compete for the available interfacial area.

In this chapter, we investigated emulsifying ability of pure discotic suspensions, nonionic hydrophobic surfactant, and the mixture of both. By systematically varying surfactant/particle concentrations in bulk and microfluidic emulsification, we found that TBA-ZrP platelets adsorb onto the oil-water interfaces in competition with surfactant molecules. Platelets exfoliated with less hydrophobic cations — TPA^+, TEA^+, and TMA^+ exhibited much less affinity toward the oil interface. Additional characterization of the drying/collapse behavior of emulsion droplets have been carried out. Accurate knowledge of platelet assembly at interfaces in mixed surfactant-platelet systems enables us to design stable emulsion for high concentration ZrP encapsulation.

7.3 Materials and Methods

Emulsions are prepared in bulk (mechanical emulsification) as well as a droplet based, microfluidic process. Bulk emulsification involves direct mixing of the combined oil and aqueous solution (total volume 1 mL) with vortex mixture at 2000 rpm for 1 min. The continuous oil phase used in all experiments is composed of 1 wt% Span 80 surfactant in hexadecane unless otherwise specified. The dispersed phase is an aqueous

suspension of ZrP monolayers exfoliated with tetraalkylammonium hydroxide (denoted as TXA-ZrP; X=M for methyl, E for ethyl, P for propyl, and B for butyl in this section). Uniform emulsion droplets were prepared using flow focusing microfluidic device, where the continuous oil phase was introduced from the side channels and the disperse phase introduced in the middle stream, as shown in the schematic (Figure 7.2). The dimensions of the side, main channels, and the orifice are 150, 150, and 50 μm, respectively. The flow rate (Q) of the oil and aqueous phase (usually in the order of 10^{-1} mL/hr) was controlled separately via two syringe pumps, which were connected to the inlets of the channel via PE tubing. Fabrication of the device was described in section 2.3.
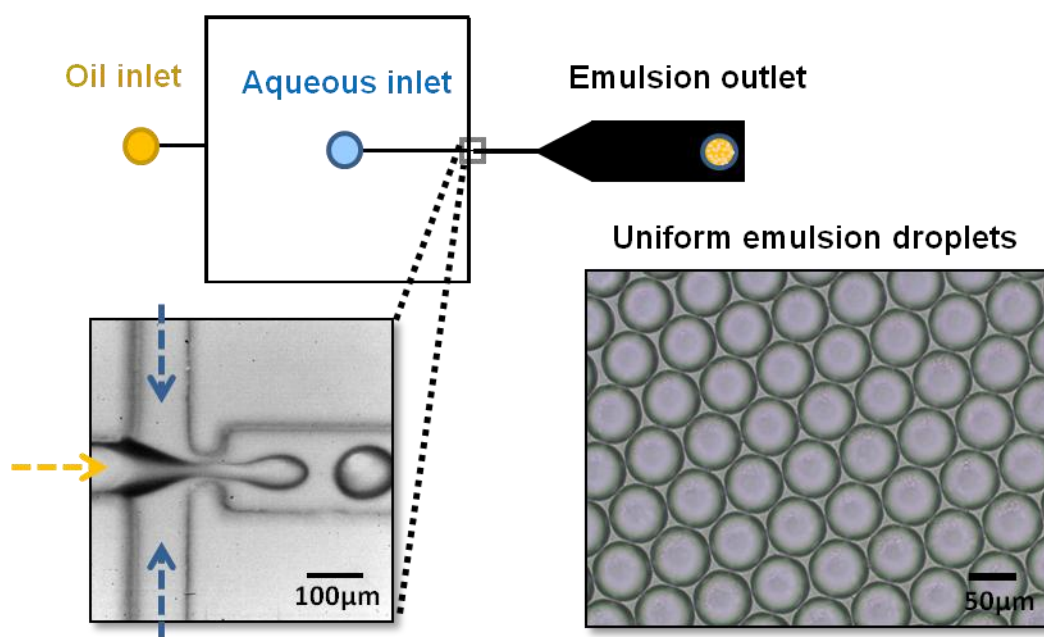
Figure 7.2. Schematic of microfluidic emulsification device in flow focusing geometry. Inserted images show the formation and the resulting emulsion droplets generated at Q_{oil} = 0.4 mL/hr and Q_{aq} = 0.1 mL/hr.

7.4 Bulk Emulsification of Discotic Suspensions

Since the formation of stable water-in-oil (W/O) emulsions is critical in the encapsulation or confinement of ZrP-based discotic suspensions in spherical geometry, the surfactancy of Span 80 in the presence of ZrP platelets in the aqueous phase was evaluated. To determine whether any synergistic effect is present between the hydrophobic surfactant and the hydrophilic particles in forming emulsions, the ability of Span 80 and ZrP platelets to form stable emulsions on its own was first examined. Upon vortex, the lipophilic, nonionic surfactant Span 80 (hydrophile-lipophile balance, HLB value = 3.4), as a common emulsifier to generate inverse emulsions, formed W/O emulsions at 1:4 water-to-hexadecane ratio; emulsion stability decreases with decreasing surfactant concentrations, where droplet coalescence and Oswald ripening eventually leads to the separation of the oil and aqueous phase. Significant emulsion destabilization (phase separation within 24 h) was observed for surfactant concentration below 0.12 wt%. On the other hand, ZrP platelets (exfoliated with tetraalkylammoniums) have no stabilization effect for W/O emulsion, with the bulk water phase released immediately when stirring has stopped.

7.4.1 Emulsions Stabilized by Mixed Surfactant—Platelet System

Mixed surfactant-platelet system was investigated by fixing either the particle or surfactant concentration and varying the other. Figure 7.3 shows the optical micrographs of a series of W/O emulsions stabilized by varying amounts of Span 80, with a fixed particle concentration in the aqueous phase. A significant change in average size (from several microns to 48±9 μm) and a remarkable reduction of emulsion polydispersity

(estimated 20%) was observed with addition of TBA-ZrP platelets in the water phase (Figure 7.3a,b). The droplet size gradually increases with decreasing surfactant concentration (Figure 7.3b~f), indicating decreasing emulsion stability, which is consistent with the increase in surface tension between hexadecane-water interface with decreasing Span 80 concentration below the critical micelle concentration.[197] An intriguing phenomenon, however, is the presence of non-spherical emulsions at Span 80 concentration below 0.5%. A common feature of all emulsions stabilized by surfactant is that they retain spherical shape when not subjected to external forces, a consequence of minimization of surface energy. Emulsion droplets of non-spherical geometry is exclusive to systems where the interfacial area cannot be relaxed, i.e., capsules with elastic shells or jammed particles that cannot escape from the interface into the bulk phase. In the case of Pickering emulsions, non spherical geometries can be obtained by (1) deformation via external forces such as compression or shearing,[198] enlarging surface area of particle stabilized emulsions; an excess amount of Pickering stabilizer in the bulk phase is required to stabilize the newly created surfaces. (2) Arrested coalescence of partially covered Pickering emulsion.[199-200] Here, the observation of emulsions with sphericity less than unity, possibly cause by shearing during vortex and preserved due to particle jamming, suggests the adsorption of platelets onto the emulsion interface at reduced surfactant concentrations. When the surfactant concentration was increased up to 5% (1 wt% TBA-ZrP), the emulsion droplets remained spherical, and negligible variation in size was observed.
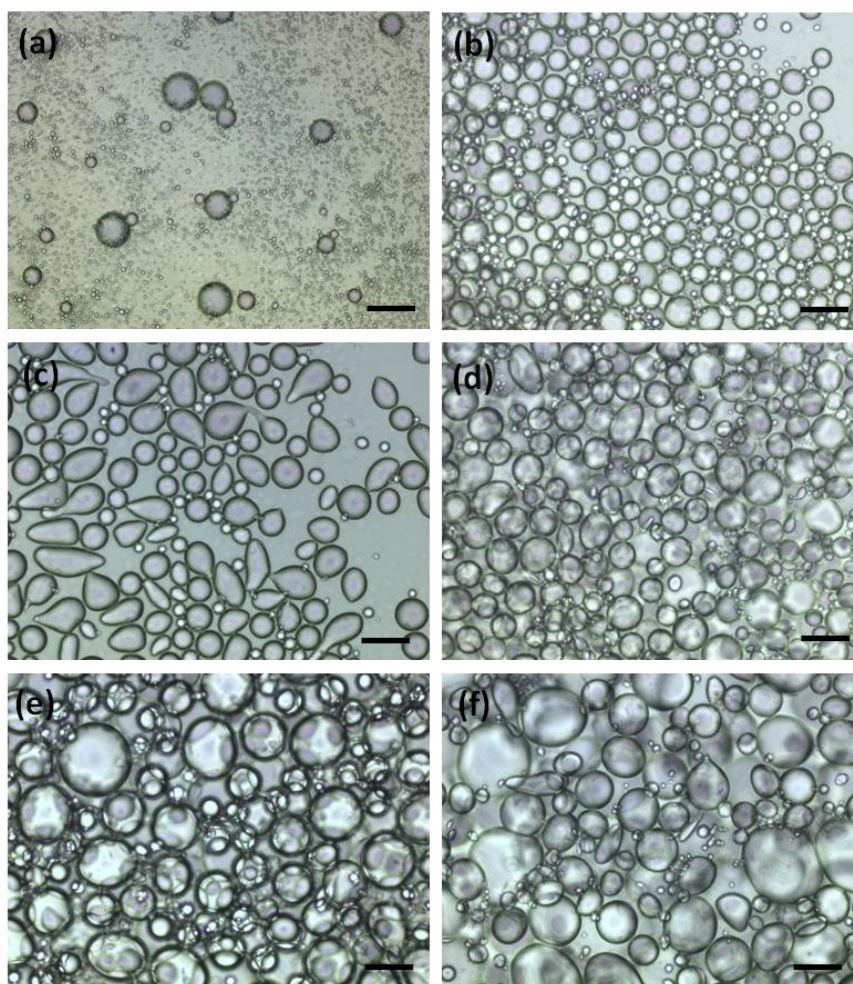
Fig 7.3. Bright filed microscopy images of water-hexadecane emulsions (1:4 volume ratio) after vortex preparation. The water-in-oil emulsions are stabilized by (a) 1 wt% Span 80 in the oil phase alone, 1 wt% TBA-ZrP platelets in the aqueous phase with initial Span 80 concentrations of (b) 1.0, (c) 0.5, (d) 0.25, (e) 0.125, and (f) 0.05 wt% in the oil phase. Scale bars: 100 µm.

At a constant Span 80 concentration (1 wt% in hexadecane), increasing particle concentration led to the formation of non-spherical emulsions (Figure 7.4). As pointed out earlier, the TBA-ZrP platelets, although cannot stabilize W/O emulsion by itself, are attracted to the oil-water interface. In general, droplets containing higher concentration of particles would form, upon particle adsorption to the interface, a denser colloidal

shell. The actual surface coverage, however, is also dependent on the size of the emulsion droplet, which is not controlled in bulk emulsification method. Nevertheless, it is evident from the trend of decreasing sphericity at either decreasing surfactant concentration at fixed particle concentration or increasing particle concentration at fixed surfactant concentration, the adsorption of TBA-ZrP platelets to the interface, creating a mixed platelet-surfactant stabilized emulsion system.
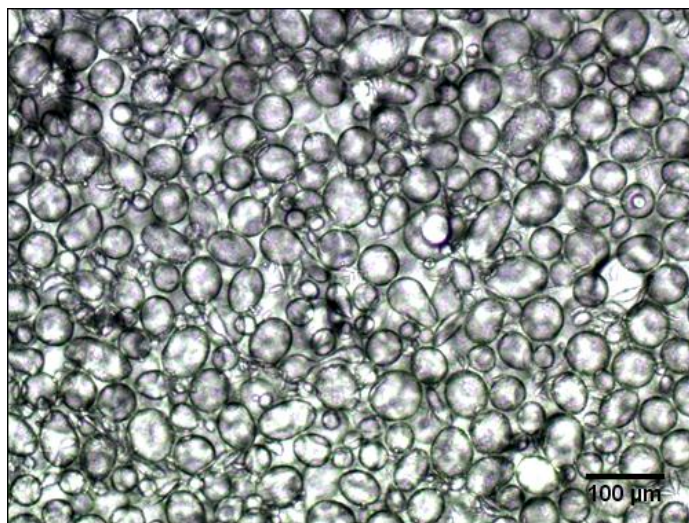
Figure 7.4. Bright filed microscopy image of water-in-hexadecane emulsions (1:4 volume ratio) containing 1 wt% Span 80 in the initial oil phase and around 4 wt% TBA-ZrP platelets in the aqueous phase.

7.4.2 Effect of Particles with Different Surface Properties on the Shape and Type of Emulsions Formed

When non-exfoliated particles were used in place of the exfoliated one, no non-spherical emulsions were formed at any combination of particle/surfactant concentrations. It is then reasonable to hypothesize that TBA-ZrP platelet's high affinity

towards the interface is a direct result of the change in surface properties as modulated by the organic cation TBA^+, which has a considerable organic phase partition coefficient and is often used as phase transferring agents in two phase chemical reaction. To test this hypothesis, we performed bulk emulsification with platelets exfoliated with other tetraalkylammoniums, whose hydrophobicity decreases with decreasing alkyl chain length. Emulsions were prepared by mixing one part of aqueous suspension of TPA^+, TEA^+, and TMA^+ exfoliated ZrP platelets (at five difference particle concentrations in between 1 ~ 12 wt%) with four parts of hexadecane containing 1 wt% Span 80. All afro mentioned emulsions displayed spherical geometry, suggesting little or no adsorption of platelets onto the interface. The results showed that the hydrophobicity of the counter cations on the platelet surfaces plays a critical role in its adhesiveness to the emulsion interface. The explanation of surface property governed particle-interface attraction is supported by the measurement of ion hydrophobicity: Octanol-water partition coefficient of TBA^+ (0.7726) is an order of magnitude higher than that of TPA^+ (0.0457), two orders of magnitude higher than that of TEA^+ (0.0027), and three orders of magnitude higher than that of TMA^+ (0.0002).[201] Additionally, a small number of double emulsions (O/W/O) were formed (Figure 7.5), which inner interface (oil in water) could only be stabilized by more hydrophilic particles.[194] The state of the emulsions was verified by the addition of a hydrophobic dye (Nile Red) in the oil phase. The concentric (or off centered) circles with dark rings (Figure 7.5c,d) demonstrates that the inner circle is an oil drop suspended in aqueous discotic suspension (liquid crystal texture shown in Figure 7.5a).
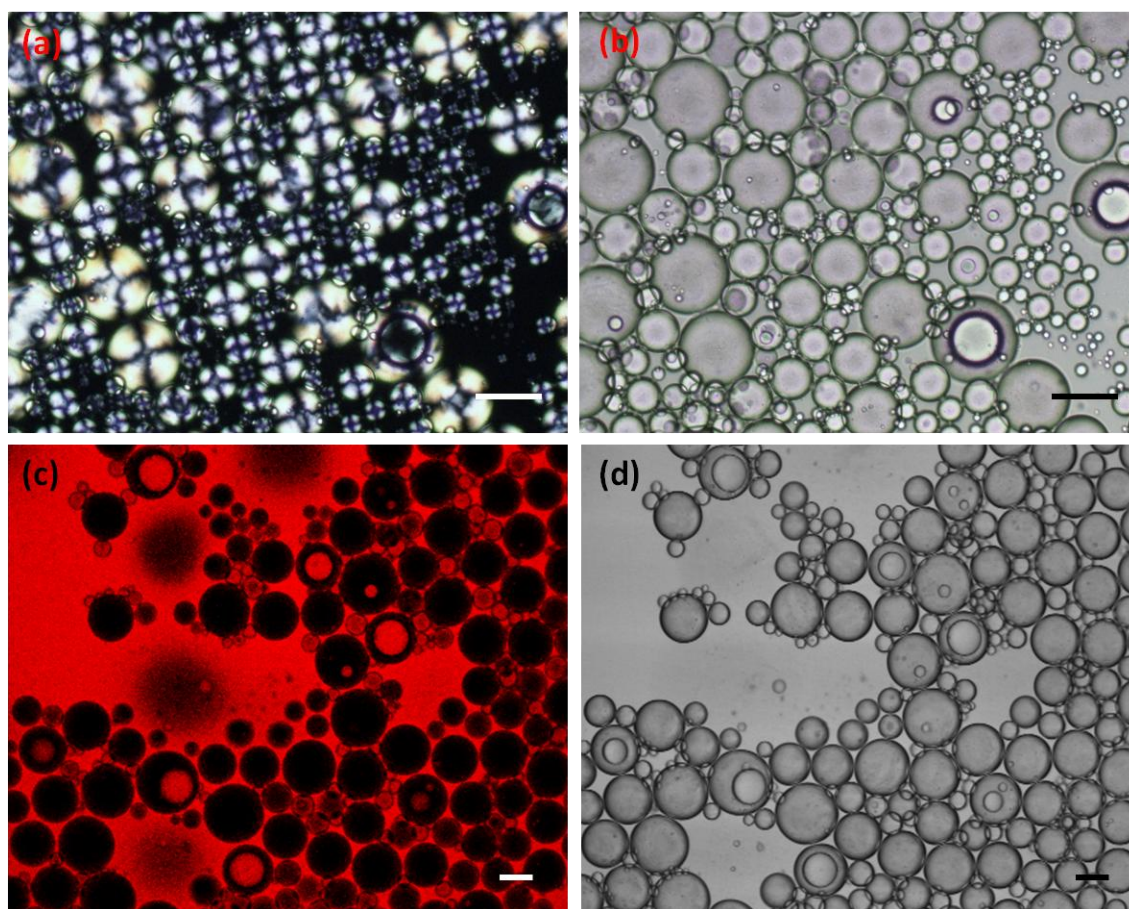
Figure 7.5. (a) Cross-polarized and the corresponding (b) bright field microscopy images of emulsion droplets (1:4 water-to-hexadecane volume ratio) containing 1 wt% Span 80 in the initial oil phase and 11.1 wt% TMA-ZrP in the initial aqueous phase. Identification of W/O and O/W/O emulsion states: (c) Confocal laser microscopy and the corresponding (d) bright field microscopy images of emulsion droplets. Nile red was added to the oil phase prior to emulsification. Scale bars: 100 μm.

7.5 Microfluidic Emulsification of Discotic Suspensions

Microfluidic emulsification technique provides a more versatile platform in which more systematic studies can be carried out. Highly monodisperse (polydispersity < 5 %), size controlled emulsion droplets can be generated by controlling fluid flow within the stable jet region. For instance, at a constant oil flow rate, the resulting droplet

size increases with increasing aqueous flow rate; for a constant aqueous flow rate, reducing oil flow rate results in larger droplet size. The total interfacial area per unit volume can thus be determined from the relative fluid flow rates (i.e. volume ratios between the continuous and disperse phase) and the resulting emulsion size.

7.5.1 Effect of Particle Concentration and Oil/Water Ratio

Figure 7.6 demonstrates the effect of varying TBA-ZrP particle concentration and changing fluid flow rate on microfluidic generated emulsions. At fixed fluid flow rate and surfactant concentration (1 wt% Span 80), increasing particle concentration from 0.13 to 1.8 wt% increases the resulting emulsion size from around 50 μm to 80 μm (Figure 7.6a, b) due to the higher viscosity value of the inner fluid phase.[202] Jammed, partially coalesced emulsions were observed when the particle concentration exceeds 2.4 wt% (Figure 7.6c). Note here that individual, monodisperse droplets were formed at the orifice (data not shown) before the emulsions traveled into the collection chamber and started colliding and coalesce at some distance downstream. These results confirmed our previous statement (conducted from results in Figure 7.4) that increasing particle concentration in the aqueous phase leads to increasing adsorption of platelets onto the emulsion surface. It is still unclear, however, on how the attachment of platelets expelled the surfactant molecule from the interface, leading to the destabilization of emulsion droplets. Conversely, increasing aqueous-to-oil ratio at a constant surfactant and particle concentration (ϕ_w = 1.8 wt%) in the initial oil and water phase decreases the stability of the emulsion droplets (Figure 7.6b, d~f). At lower water-to-oil ratios ($Q_{aq}/ Q_{oil} \leq 1/5$), monodisperse emulsions were formed (polydispersity < 2%). Variation of droplet sizes

with flow parameters is in good qualitative agreement with droplet size scaling in microfluidic flow focusing devices.[203] At higher flow rate ratio, droplet size increased, and demonstrated a biomodal distribution (centered at 118 ± 2 and 154 ± 1), where the smaller size has a higher frequency than the larger one. Large droplets were formed not via droplet pinch off at the orifice, but by the merging of two small droplets (the average droplet volume ratio is 2.17 ± 0.05). Coalesced droplets remain spherical at $\phi = 1.8$ wt% in the dispersed phase, indicating limited interface adsorption.
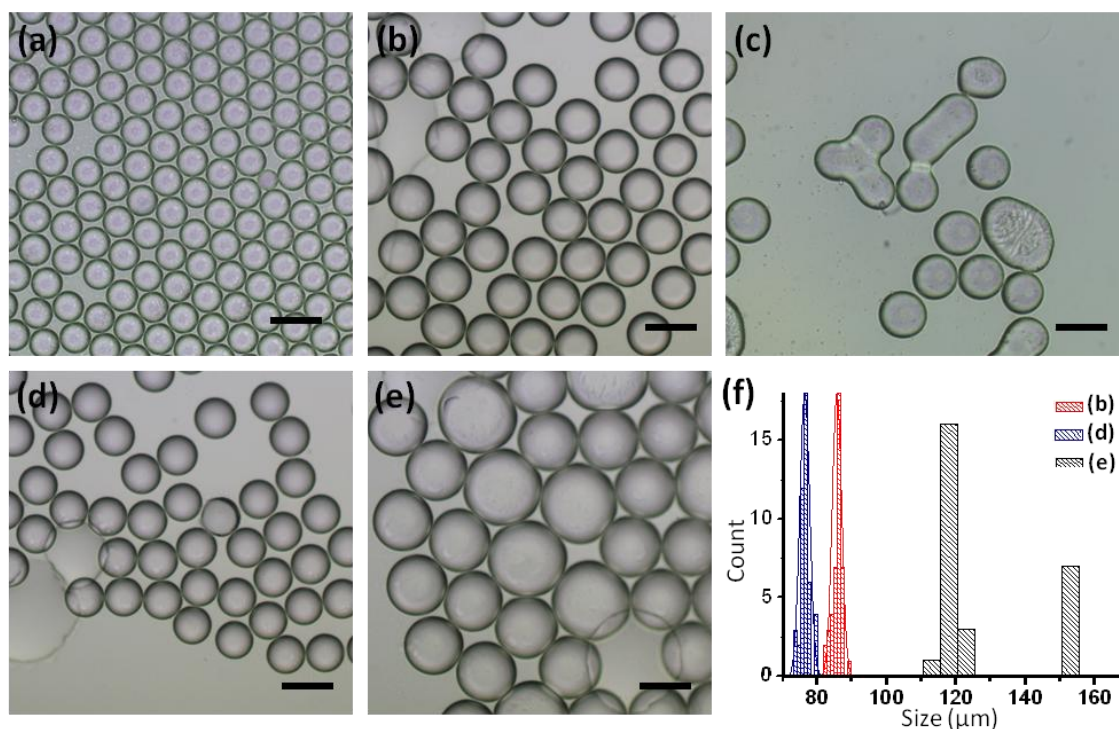
Figure 7.6. Stable and coalesced structures of microfluidic generated emulsion droplets. The concentrations of TBA-ZrP platelets in the aqueous phase are (a) 0.13, (b) 1.8, and (c) 2.4 wt% ($Q_{oil} = 0.5$ mL/hr , $Q_{aq} = 0.1$ mL/hr). The ratio of oil and aqueous flow rates (mL/hr: mL/hr) are (d) 0.6: 0.08 and (e) 0.4: 0.2 ($\phi_w = 1.8$ wt%). (f) Size distributions of droplets containing 1.8 wt% platelets at varying oil/water ratios. Solid lines are the fitted normal distribution. Scale bars: 100 μm.

7.5.2 Drying of Emulsion Droplets

Shape transition of a drying emulsion droplet is characteristic of the type of surface stabilizers (i.e., surfactant molecules or solid particles). In the case of surfactant stabilized emulsions, droplets shrunk while maintaining spherical shape due to minimization of surface energy. As the surface area decrease, surfactants desorbs from the oil-water interface into the dispersed phase in the form of micellar aggregates. On the other hand, for particle stabilized emulsions, the particles are effectively trapped at the interface because the size is much bigger size than surfactant molecules. Consequently, to adapt to the reduced interfacial area from drying, wrinkled surfaces are formed and the emulsion shells (consist of solid particles) would start to buckle.

A small droplet of emulsions was placed on a glass slide, where the water was allowed to evaporate. Figure 7.7 shows the size and shape evolution of the emulsion droplets (0.16 wt% TBA-ZrP) upon water evaporation. Shape transitions proceeded in two stages: Initially, the emulsions shrunk in the same way as the surfactant stabilized system (remain spherical), though the timescale (minutes) for droplet size reduction was faster than that of the pure Span 80 systems (hours). After ten minutes of exposing the sample to ambient conditions, wrinkling of emulsion surfaces occurred, and further drying lead to the formation of rasin-like, nonspherical structures.
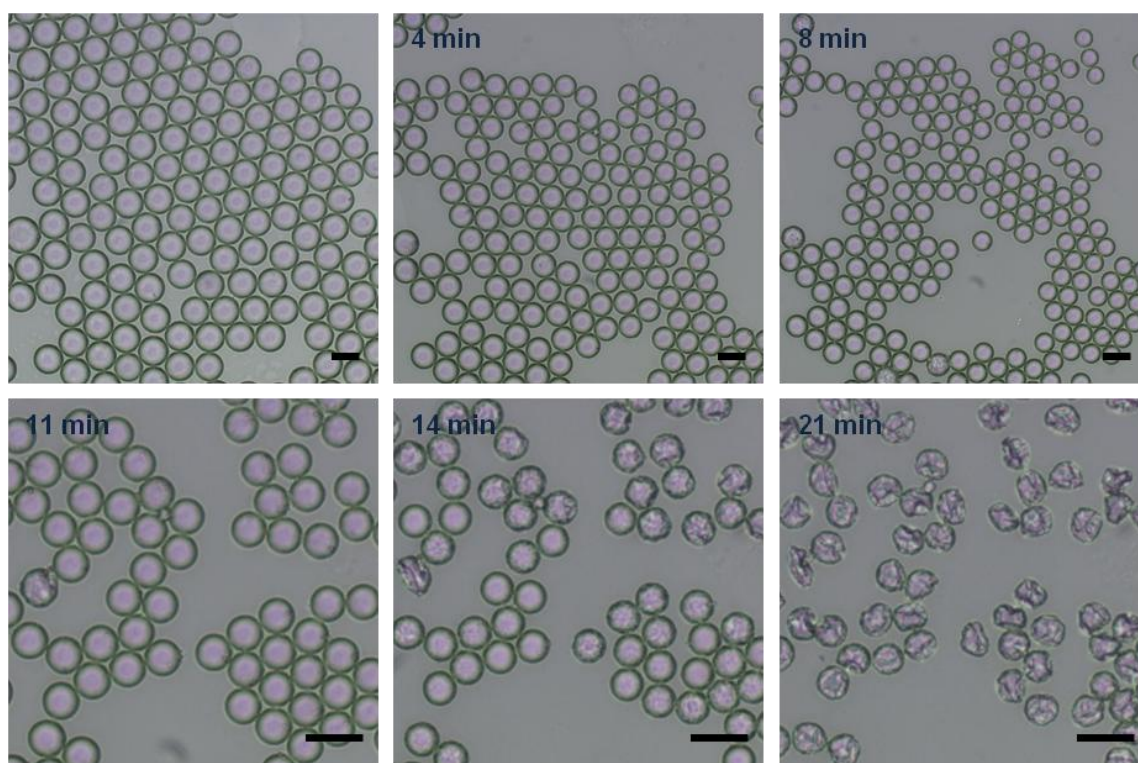
Figure 7.7. Time laps of water evaporation from discotic emulsion droplets. Particle concentration is 0.16 wt%; oil and water flow rates are 0.5 and 0.1 mL/hr, respectively. Scale bar: 50 μm.

The change in the relative diameter D_t/D_0 (D_t: diameter of droplet at time t; D_0: initial droplet diameter) of emulsion droplets is shown in Figure 7.8. The diameters were recorded until buckling or surface wrinkling occurred. Two observations on drying of TBA-ZrP/span 80-based emulsions were made from these experiments: First, the lifetime of spherical emulsions, defined as the period from which the emulsion was placed onto the glass slide to the disappearance of spherical drops (i.e., droplets became non-spherical), decreases with the increase of particle concentration (ϕ_w), which suggests that water permeability increases with the amount of TBA-ZrP platelets in the water phase. Secondly, the extent of droplet shrinkage before buckling decreases with

increasing particle concentration (Figure 7.9). D_c is the critical droplet diameter at which buckling transition was observed. For example, for $\phi_w = 0.14$ wt%, the emulsions shrunk 51% in size before surface wrinkling as oppose less than 2 % for $\phi_w = 1.80$ wt%. Table 7.1 summarized the critical transition sizes for different initial platelet concentrations in the aqueous phase. In general, buckling or surface wrinkling of Pickering emulsions corresponds to interfacial areas smaller than that occupied by interfacially confined particle in closed packed configuration. Close packing of spherical particles at 2-D interfaces yields a fixed surface density. In this scenario, the surface density at which shape transition occurs is a constant value, and the critical particle concentration (assuming the amount of particle adsorption is solely a function of bulk phase concentration) would be the same for all samples, regardless the initial particle concentration before droplet shrinkage or deformation. However, this is not the case for our experiments, where the critical concentrations varied and seemed to follow no specific trend (last column in Table 7.1). Instead, three groups of critical concentrations exist ($\phi_w = 0.12$ %, 0.14~0.6 %, and 1.2~1.8 %). This could be attributed to the influence of platelet adsorption dynamics, particle self-assembly upon drying in closed spherical geometry, rate of water evaporation, and the specific droplet size at deformation transition.
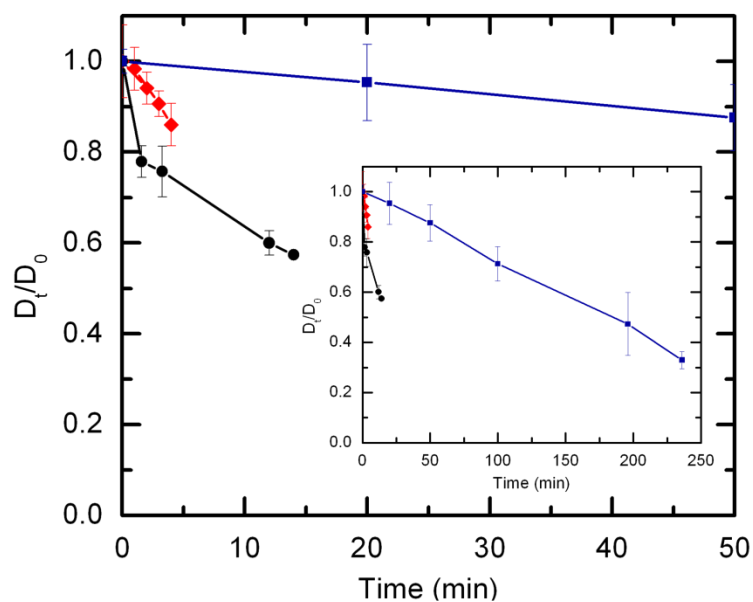
Figure 7.8. Changes of the relative diameter (D_t/D_0) of the emulsion droplets containing varying amounts of TBA-ZrP platelets, including concentrations of 1.2 wt% (◆), 0.24 wt% (●), and 0.12 wt% (■). Insert is the same graph with a broader time scale.
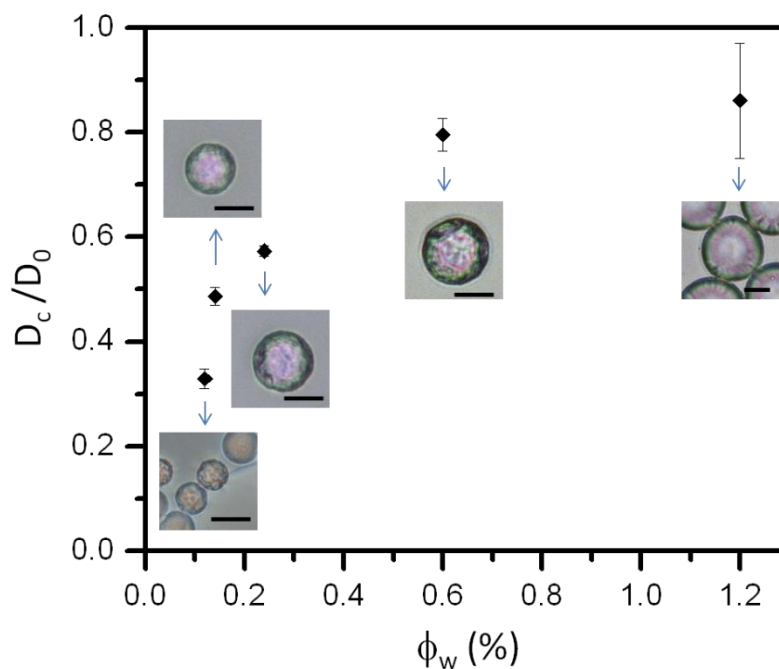
Figure 7.9. Critical (relative) diameters for shape transition at different initial ϕ_w. Inserts are the corresponding droplets upon further shrinkage/deformation. Scale bars: 20 μm.

Table 7.1. Droplet Shrinkage and Critical Deformations

ϕ_w (%)	D_0 (μm)	D_c (μm)	D_c/D_0	$\phi_{w,c}$* (%)
1.8	85.9±1.4	84.9±1.4	0.99±0.03	-
1.2	54.3±4.4	46.7±2.2	0.86±0.11	1.89±0.21
0.6	44.9±1.0	35.7±0.6	0.80±0.03	1.19±0.04
0.24	53.4±0.6	30.6±0.2	0.57±0.01	1.27±0.01
0.14	54.9±1.3	26.7±0.3	0.49±0.02	1.23±0.02
0.12	56.3±1.5	18.5±0.6	0.33±0.02	3.37±0.06

*$\phi_{w,c}$ is the calculated particle concentration at critical shape transition (droplet diameter D_c).

Figure 7.10 shows the shape transition of emulsions with TBA-ZrP (Figure 7.10a,b) and TMA-ZrP (Figure 7.10c) particles upon drying. First, the topology of the buckling layer for TBA-ZrP containing emulsions is compared. For samples with lower initial platelet concentration (Figure 7.7 and Figure 7.10b), surface wrinkling and obvious ripples were observed. As the droplets continue to deform after the smooth spherical surface has faded, buckling caused large scale indentation from all sides (except for droplet-glass contact region) of the structure, similar to the deformation of solid, elastic shells. Conversely, at high TBA-ZrP ϕ_w (Figure 7.10a) droplet shrinkage results in the formation of angled edges, instead of the deflation type deformation.

In contrast to the TBA-ZrP system, shrinkage rate of TMA-ZrP based emulsions only leads to deformation at very high internal suspension concentration (estimated $\phi_{w,c}$ = 0.24 for ϕ_w = 0.01; $\phi_{w,c}$ = 0.1 for ϕ_w = 0.04). Also, no surface wrinkling was observed, as shown by the smooth contour of drying droplets (Figure 7.10c). An interesting aspect of the drying shape transformation of TMA-ZrP emulsions is that most droplets shrank
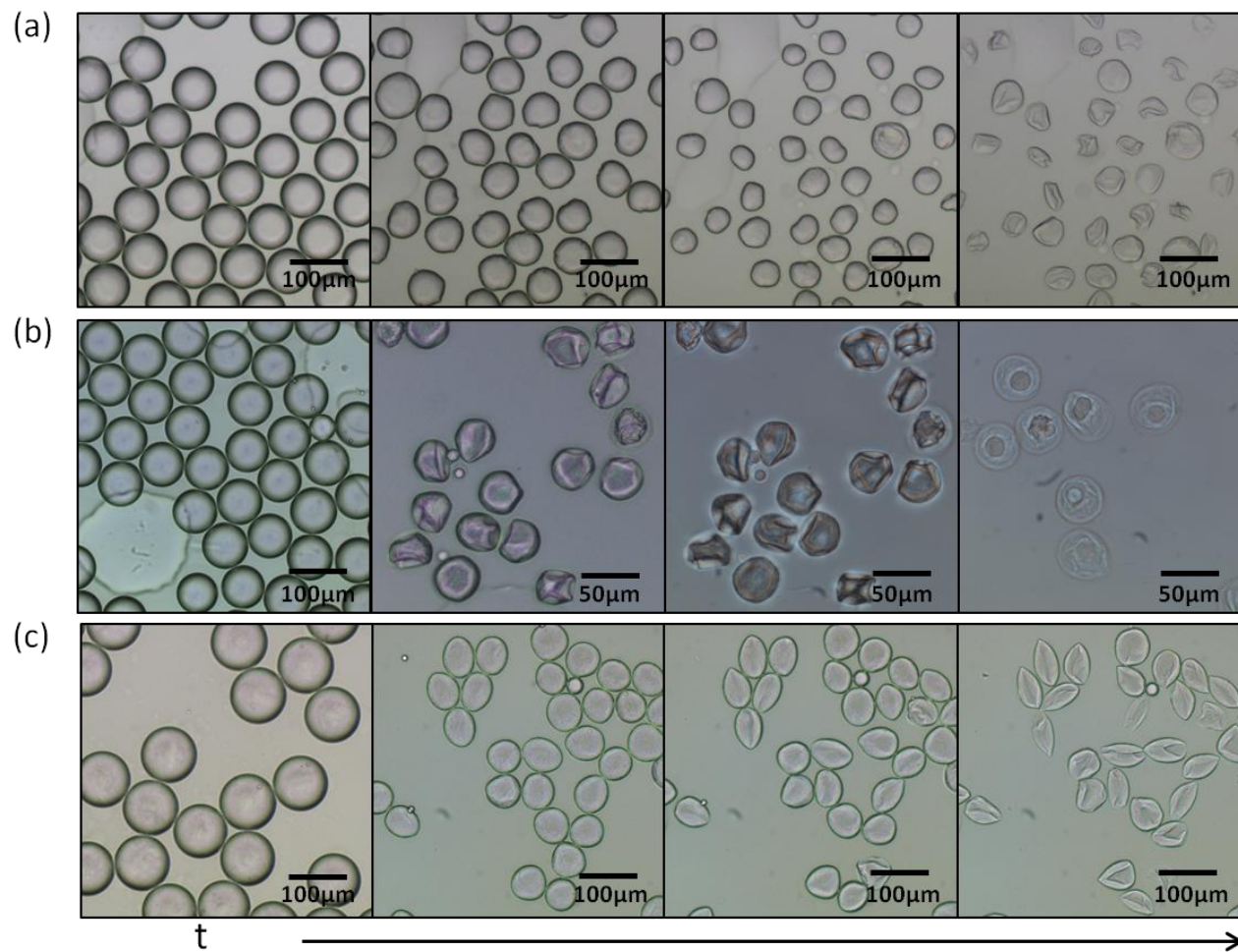
Figure 7. 10. Shape transitions upon droplet drying. Initial aqueous phase contains (a) TBA-ZrP 1.8 wt% (b) TBA-ZrP 0.8 wt% (c) TMA-ZrP 4.2 wt%; oil phase is consist of hexadecane with 1 wt% Span 80. ($Q_{oil}:Q_{aq}$ = 5:1)

uniformly, and transition into either an oval, football shape or a triangular-like shape with increasing sharp corners as they dry. The novel shape transition could be the result of liquid crystal ordering that translates to the structured deformation. Figure 7.11 displays high magnification views of dried emulsion droplets with wrinkly shell (Figure 7.11a,b) and curled films (Figure 7.11b,c). Surface cracking was observed in the dried solids of TMA-ZrP droplets, which is a common morphology in dried films made up of tetraalkyammonium exfoliated ZrP monolayers. Thus we can say, with confidence from the evidence collected via bulk and microfluidic emulsion generation that Pickering emulsions were formed only with TBA-ZrP platelets-Span 80 surfactant systems. For platelets prepared with the other counter ions (TXA$^+$, alkyl chain length $\leq$ 3), there was not enough driving force (i.e. hydrophobic interactions) for the platelets to assemble at the interface and form colloidal shells around the W/O droplet.
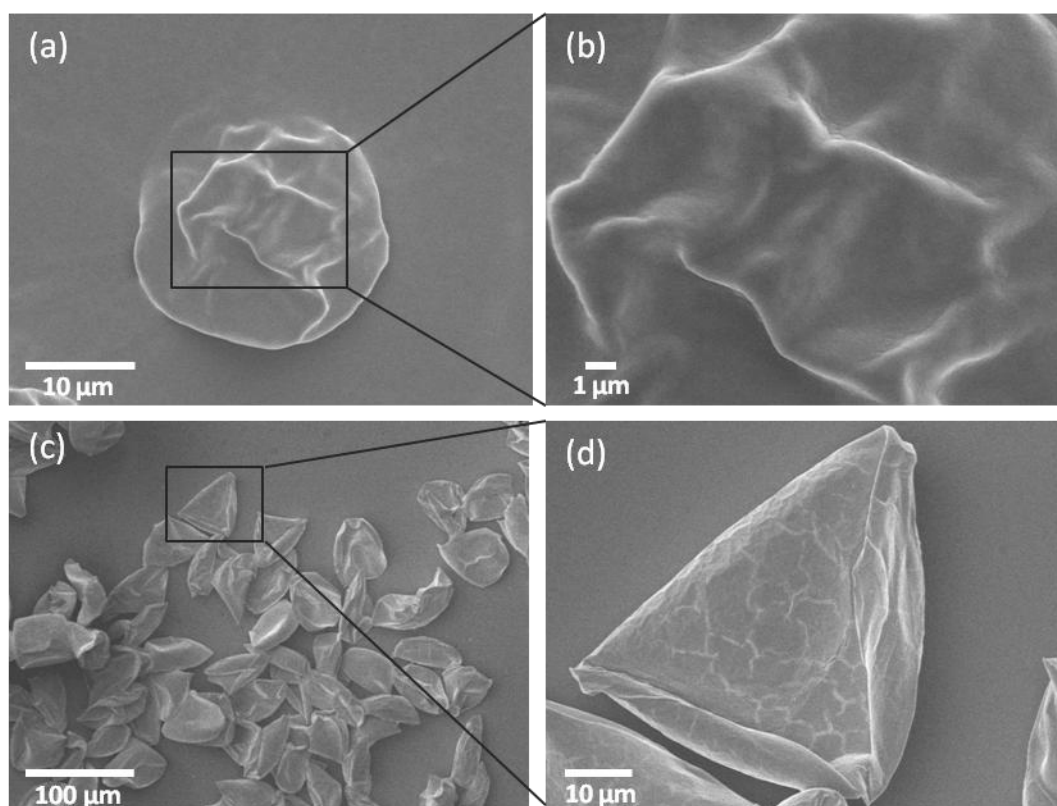
Figure 7.11. Low (left panel) and high (right panel) magnification SEM images of dried solids left over after oil phase removal from emulsion droplets containing (a), (b) TBA-ZrP and (c), (d) TMA-ZrP platelets.

7.5.3 Colloidal Discotic Liquid Crytsals in Emulsion Droplets

As described in previous sections, the stability of the emulsions and the ability to form uniform dicotic droplet depends on factors including surfactant concentration, continuous-to-disperse phase ratio, and most importantly, the type of platelets used and the corresponding particle concentration. At fixed Span 80 concentration and oil-to-water phase ratio, stable, monodisperse emulsion droplets can be formed to incorporation higher concentrations of TMA-ZrP platelets than TBA-ZrP platelets. Figure 7.12 shows emulsion droplets with liquid crystal defects from colloidal discotics

in the I-N biphase and the full phase region. Biaxial liquid crystalline defect ─ two point boojums defect[204] (where two brushes disconnect at the center) was observed in both samples (Figure 7.12a). Higher concentration discotic emulsions displayed stronger birefringence intensity and more distinctive defect lines (Figure 7.12b). Defects of discotic suspensions stored in discreet volumes could provide an alternative or even more sensitive method to study the liquid crystal phase transition.
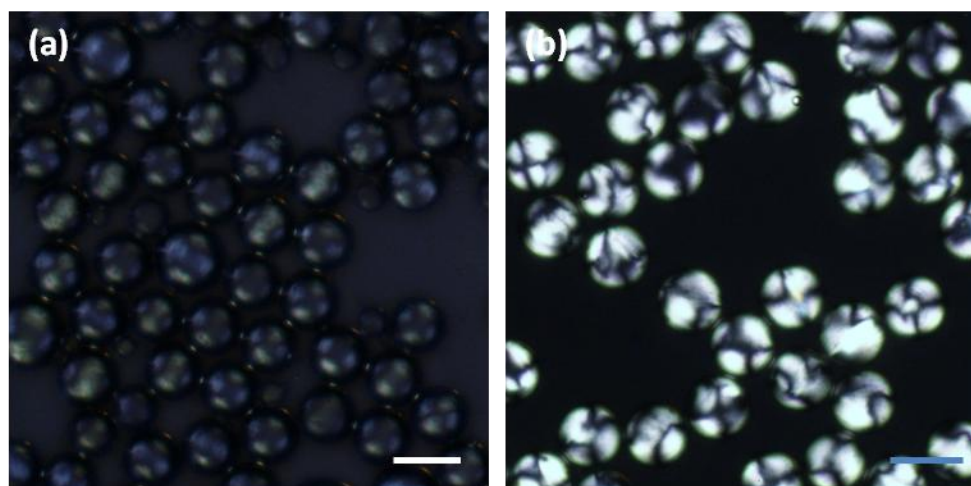
Figure 7.12. Cross-polarized micrograph of discotic droplets containing (a) 1.0 wt% ZrP-TBA and (b) 4.2 wt% ZrP-TMA. Scale bars: 100 μm.

7.6 Conclusions

Different from other mixed particle-surfactant emulsion systems, where the surfactants first adsorbed onto the particles in a pre-mixed single phase,[195,205] we investigated systematically the emulsification of ZrP platelet containing aqueous phase and Span 80 containing oil phase. Strong synergistic effects exist between the surfactant and ZrP platelet in stabilization oil-water interfaces with different curvatures (i.e., favors

W/O or O/W emulsions). For emulsions stabilized by Span 80 and TBA-ZrP, decreasing the surfactant at constant particle concentration or increasing particle concentration at fixed surfactant concentration lead to the formation of non-spherical droplets; in contrast, for TMA-ZrP (the same is applied for TPA-ZrP and TEA-ZrP) system, emulsions remain spherical and some double emulsion were formed upon mixing at high particle concentrations. Non-sphericity of emulsion droplets was attributed to the attachment of slightly lipophilic TBA-ZrP to the water-oil interface, forming platelet-stabilized Pickering emulsions. The inferred TBA-ZrP platelet adsorption was later confirmed by coalescence and drying studies of uniform, microfluidic generated droplets at a range of particle concentrations.

Additionally, water permeability was enhanced in the presence of TBA-ZrP. We observed buckling transition of Span 80/TBA-ZrP emulsions, which can be attributed to platelet jamming at the interface as the interfacial area reduces. The difference in shape transition during drying process can be derived from the different adsorption extent of the platelets on oil-water interface. Understanding how surfactant/ particle concentration and particle surface properties influence the emulsion stability helps identify the parameters for the formation of stable, emulsion confined discotic suspensions.

CHAPTER VIII

CONCLUSIONS AND FUTURE WORK

8.1 Summary

Surface engineering and interaction-controlled self-assembly of amphiphilic molecules and micron-sized, disk-shaped particles at different length scales into ordered structures has been investigated. At a fundamental level, understanding collective behaviors of the individual building blocks is pivotal to the development of novel soft materials, which is the motivation behind this work.

Chapter III described how surface structures of self-assembled block co-polymer vesicles directed the molecule reaction occurring on polymersome surfaces. A fluorescence labeling method was developed to embed probes on such structures, which enabled quantitative description of reactivity of polymersoms. With this, well established fluorescence quenching method, often used in the field of biophysics, was adapted to evaluate reactivity for two surface morphologies: one where the reactive site was attached on a longer polymer than the surrounding polymer brushes, and one was attached on polymer of the same length as the unmodified polymers. It was found that the reactivity of the functional group with small molecules (iodide ions) is higher in the former scenario. The results from additional quenching and ion mobility studies showed that the change in small molecule reactivity on polymersome surfaces was the result of ion retardation in the polymer-rich environment. With the use of depletion attraction, we

also showed that the polymeric surface (of hydrophilic polyethylene gloycol brushes) prevented fusion of polymersomes undergoing strong attraction and deformation.

Chapter IV onwards focused on the second self-assembled system, i.e., colloidal platelets, which despite their abundance in nature have received less attention than their spherical counterparts. The raw material used was a synthetic, inorganic layered crystal α-Zirconium phosphate (α-ZrP). We developed surface modification technique of ZrP monolayers via direct exfoliation with various compounds, including the commonly used tetrabutylammonium hydroxide. Anisotropic particles, like the one used in this work, have the tendency to form discotic nematic fluid, especially when the aspect ratio (diameter/thickness) is large. By systematically varying the chain length of the tetraalkylammonium used for exfoliation, nanoplatelets with different aspect ratios were prepared, and the dependency of isotropic-nematic transition on surface cation moiety was experimentally determined. Fractionation method via isotropic-nemtaic phase separation promoted the analysis of the effect of polydispersity on I-N transition. Size segregation analysis at varying stage on the phase diagram (i.e., different particle concentration from nematic liquid crystal to layered liquid crystal phases, such as smectic or twist grain boundary phase) facilitated the analysis of transition points. Successful exfoliation with a mixture of small alkylamine and a primary amine bearing polymer (i.e. Jeffamines, a water soluble polyether) provided a similar system with improved suspension stability against gelling.

In Chapter V, the dependency of phase transition of charged ZrP nanoplatelet suspensions on ionic strength was investigated by considering ion exchange effects. The

experimentally mapped, two dimensional phase diagram (function of ionic strength and particle concentration) showed that TBA exfoliated ZrP nanoplatelets behave similar to regular charged platelets with advanced stability in the absence of ion exchange. The use of NaCl salt to tune ionic strength, however, induced ion exchange that eventually lead to colloidal gel formation. The synergistic effect of ion exchange presented an unprecedented phase transition route for ZrP platelets; one that can go from an arrested system to isotopic liquid or liquid crystal states at increasing particle concentration. The jammed states, i.e., colloidal gels, were verified and characterized by rheology and light scattering measurements. The existence of crystal edge defect in α-ZrP suggested a possible pH dependent-charge distribution that leads to anisotropic interactions, similar to that of the "house of card" structures in clays, between individual platelets in acidic pH conditions.

Following the various surface modification scheme, Chapter VI presented amphiphilic biomolecule assembly on colloidal platelets of ZrP. Inspired by lipid bicelles (discotic lipid assembly), two general strategies were applied to decorate platelet surfaces with phospholipids: supported lipid bilayer and hybrid lipid bilayer, i.e., lipid monolayer on hydrophobically functionalized substrate. Driven by electrostatic interactions, liposomes of opposite charge to TBA exfoliated ZrP monolayers were attracted to platelet surfaces. However, irreversible lipid-platelet aggregates were formed instead of stable, lipid bilayer-coated platelets. Lipid monolayer assembly on hydrophobic ZrP was more tolerant to lipid compositions since the attachment was controlled solely by hydrophobic interactions, thus the headgroup moiety irrelevant.

While successful monolayer deposition was achieved, hydrophobically modified ZrP monolayers self-assembled into 10~100 micron-sized lamellas prior to physisorption of the phospholipids. Experiments are ongoing to investigate the role of alkyl chain length on the morphology of platelet assemblies organized via strong inter-platelet interactions.

Slight variation in surface property (i.e., the hydrophobicity of the counter cations on the surface) of ZrP nanoplatelets was demonstrated in Chapter VII to have a dramatic effect on the emulsification of discotic suspensions. Water-in-oil Pickering emulsions were formed with Span 80/ TBA-ZrP platelet system, where the nonionic, lipophilic surfactants competed with the particles for oil-water interfacial area. Microfluidic emulsification technique was carried out to establish relationship between particle concentration and the liking to form non-spherical droplets, a characteristic of solid particle-stabilized interfaces. At a fixed surfactant concentration of 1 wt% and aqueous-to-oil ratio of 0.2, microfluidic emulsion droplets containing TBA-ZrP lost the spherical geometry (i.e., partial coalescence started to appear) at particle concentration > 2 %; TMA-ZrP containing droplets remained spherical at all concentrations tested (up to 4.2 %). With bulk emulsification method, spherical droplets containing close to 11 % TMA-ZrP platelets were obtained. Drying shape transition also agrees with the absence of colloidal shell around the emulsion droplets formed with TMA-ZrP platelets. Based on our findings, phase transitions of discotic suspensions in emulsion confinement can be carried out at a wide range of particle concentrations with certain surface functionalized platelets.

8.2 Future Research and Ongoing Projects

8.2.1 Discotic Suspensions as Biomolecule Goniometer

One of the novel biophysical applications of inorganic platelet particles, as pointed out in the introduction as well as in Chapter VI, is the use of discotic liquid crystals to generate anisotropic medium where biomolecule of interest can be dissolved.[2,173] Particle alignment, in the case of ZrP platelets, can be obtained by increasing particle concentration above the I-N transition point or potentially induced by external magnetic field (Figure 8.1). The major roadblock for the use of inorganic liquid crystals is the issue of biocompatibility and suspension stability. This was addressed in previous chapters through various surface modification techniques, including direct exfoliation with Jeffamine polyetheramine (derived from biocompatible polyethylene oxide) and lipid coating on exfoliated particles. The suspension stability of Jeffamine exfoliated α-ZrP (M1000-ZrP) was investigated alongside TBA^+ exfoliated ones at the end of Chapter IV, which showed that suspension of M1000-ZrP is more stable than TBA-ZrP. Preliminary experiments demonstrated quadrupolar splitting in M1000-ZrP discotic suspensions (Figure 8.2), manifesting the idea that this could be used for protein or biomolecule NMR studies. Therefore, the future work investigates the actual application of ZrP in solution NMR starting with structural determination of simple amino acid.[206]
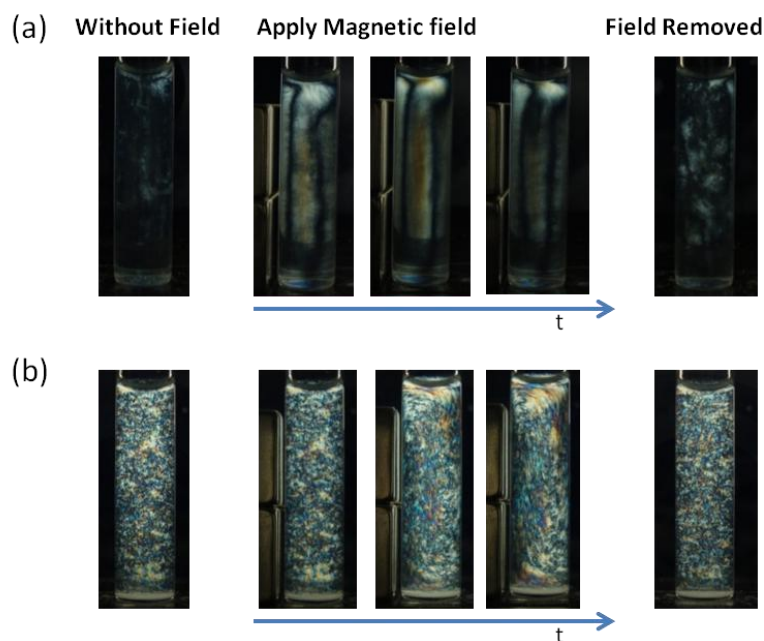
Figure 8.1. External magnetic field induced alignment of ZrP platelets in the (a) biphase region and (b) nematic phase. Permanent magnet was approached and place on the left side of the samples. The first image was taken approximately 30 s after field application.
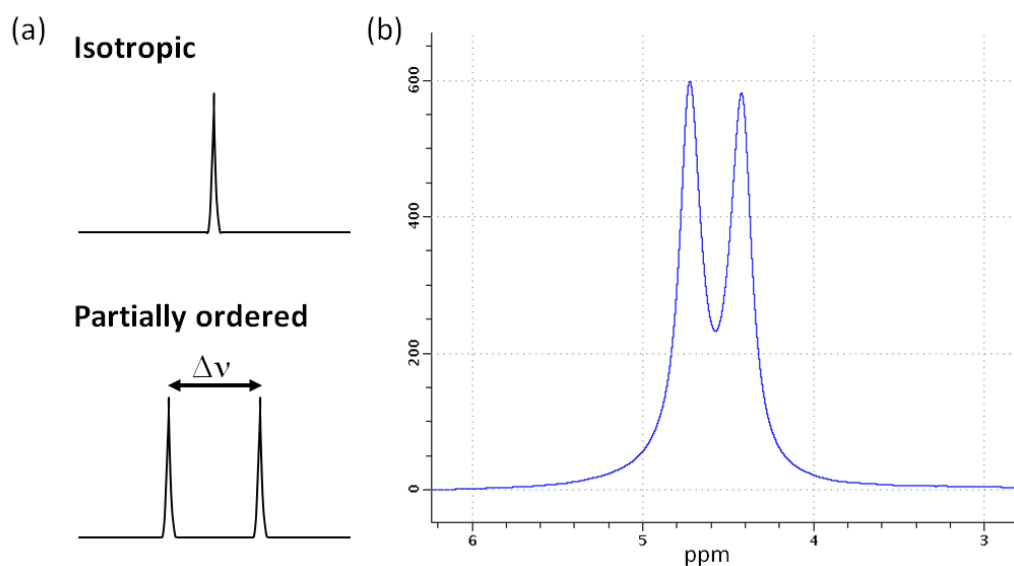
Figure 8.2. (a) Schematic of typical quadrupolar NMR spectrum of isotropic and ordered media. (b) Deuterium NMR spectrum of a discotic platelet suspension (M1000-ZrP, $\phi_w \approx 3$ %). 1 ppm ≈ 61 Hz.

8.2.2 Size-Dependent Gelation and Aging Dynamics of Colloidal Discotic Supsensions

In this dissertation, we have discussed the use of ion exchange induced anisotropic interactions to form colloidal gels. It was found in the studies carried out in Chapter V, that suspension pH is the formative factor in the sol-gel transition. The specific face-edge attraction, i.e. surface charge distribution, in ZrP platelet system can be tuned via pH. By reducing suspension pH with dilute hydrogen chloride to around 5, these so-called sticky spots[207] (patches on colloids where specific attractions were engineered, also referred to as particle valence[208] in most literatures) appears, adding specificity particle-particle interactions. Recently, increasing theoretical[207-209] and experimental efforts have been focusing on patchy particles[210-212] — spherical particles patterned with functionalities or particles of non-spherical shape. New material states of empty liquids and equilibrium gels[207,213] was introduced and experimentally demonstrated with several year-long study on Laponite suspension.[214] Preliminary studies on ZrP of controlled charge distribution (fixing pH at a value above pI_{face} and below pI_{edge}) suggest that this system behaves remarkably similar to that of aging Laponite gels but evolve at a much shorter time scale (Figure 8.3); ZrP suspension enter arrested state at low particle concentration, and phase separation occurs for initially gelled sample in the coexistence region.

We plan to investigate gelation dynamics using optical characterization methods, as the ones presented in Chapter V. It will be interesting to see if the boundary of the transitions and the aging dynamics are affect by the size of the building blocks, which can be varied systematically via synthetic conditions.

| 0.03 | 0.07 | 0.14 | 0.28 | 0.41 | 0.55 | 0.69 | 0.83 | 0.96 | 1.11 | 1.23 | 1.38 |
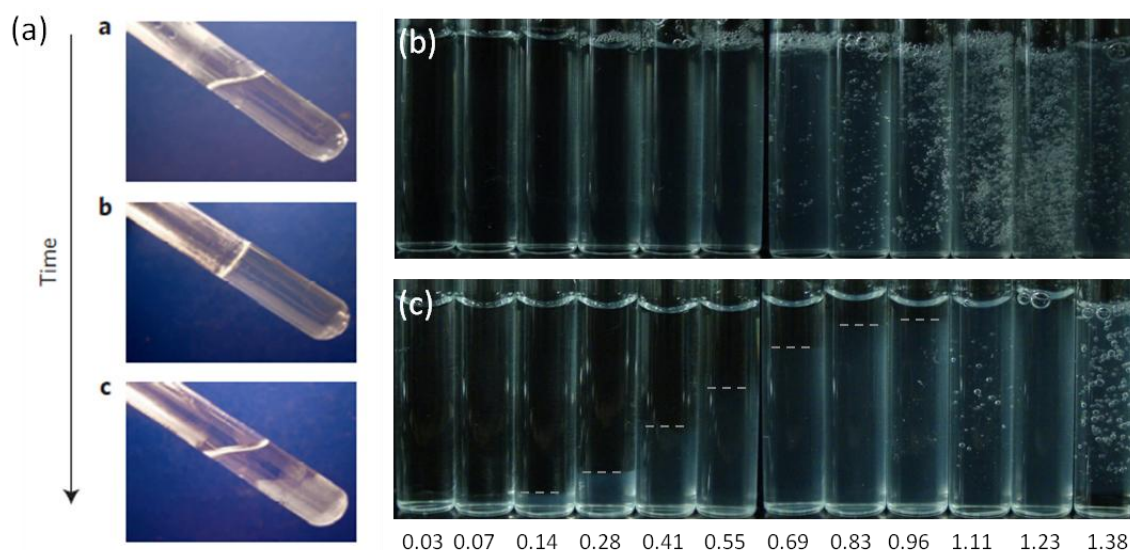
Figure 8.3. (a) Laponite suspension (0.4 wt%) evolution from at an initial fluid phase, to a gel state (time $\approx$ 4000 hr), and finally phase separated state (time $\approx$ 30000 hr).[214] Polarized photograph of ZrP suspensions in pH 5 solutions at increasing platelet concentration (left to right, labeled conc. in %w/w) (b) right after sample preparation and (c) after one week. The dashed lines indicate the boundaries of lower sediment phase and the clear upper phase.

8.2.3 Phase Transition of Disctoic Suspensions in Spherical Confinement

Formation of stable, monodisperse emulsion droplets of platelet suspensions was reported in Chapter VII. Preliminary studies showed that the change in particle concentration in the aqueous phase and spherical confinement leads to distinct changes in liquid crystal textures observed under polarizing microscopy imaging (Figure 8.4). Kinetics of isotropic-nemtaic phase formation for ZrP liquid crystal is still ill defined, since the nucleation and coalescence of nematic tactoids[215] was not observed in bulk (inside thin capillaries or sandwiched between glass slides). We plan on using isolated emulsion droplets to investigate ZrP liquid crystal phase transitions via tracking changes of liquid crystal texture at different equilibrium time after preparation. The spontaneous

formation of double emulsions by mixing high concentration ZrP suspension (TMA$^+$, TEA$^+$, and TPA$^+$ exfoliated particles) with hexadecane and hydrophobic surfactant validated the potential fabrication of O/W/O double emulsions with colloidal discotic shells using capillary microfluidics.
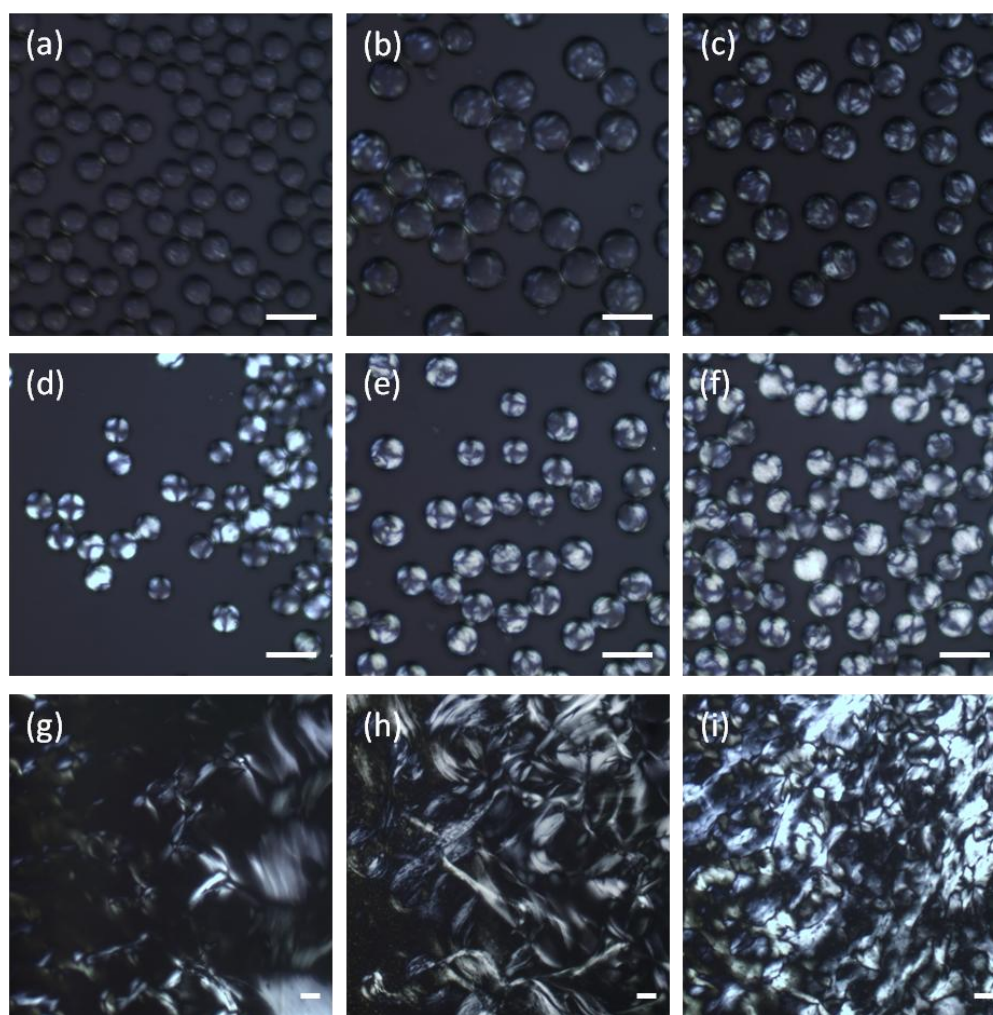
Figure 8.4. Polarized micrographs of TMA-ZrP suspension droplets at particle concentration ≈ (a) 1 %, (b) 1.25 %, (c) 1.5 %, (d) 2 %, (e) 2.5 %, and (f) 3 %. The liquid crytal texture in bulk is shown for sample concentrations of (g) 2 %, (h) 2.5 %, and (i) 3 %. Scale bars: 100 μm.

REFERENCES

(1)   Whitesides, G. M.; Grzybowski, B. *Science* **2002**, *295*, 2418.

(2)   Diller, A.; Loudet, C.; Aussenac, F.; Raffard, G.; Fournier, S.; Laguerre, M.; Grelard, A.; Opella, S. J.; Marassi, F. M.; Dufourc, E. J. *Biochimie* **2009**, *91*, 744.

(3)   Singer, S. J.; Nicolson, G. L. *Science* **1972**, *175*, 720.

(4)   Discher, D. E.; Eisenberg, A. *Science* **2002**, *297*, 967.

(5)   Percec, V.; Wilson, D. A.; Leowanawat, P.; Wilson, C. J.; Hughes, A. D.; Kaucher, M. S.; Hammer, D. A.; Levine, D. H.; Kim, A. J.; Bates, F. S.; Davis, K. P.; Lodge, T. P.; Klein, M. L.; DeVane, R. H.; Aqad, E.; Rosen, B. M.; Argintaru, A. O.; Sienkowska, M. J.; Rissanen, K.; Nummelin, S.; Ropponen, J. *Science* **2010**, *328*, 1009.

(6)   Israelachvili, J. N. In *Intermolecular and Surface Forces*; 2nd ed.; Academic Pres: Burlington, MA, 1991.

(7)   Mouritsen, O. G. *European Journal of Lipid Science and Technology* **2011**, *113*, 1174.

(8)   Marsh, D.; Bartucci, R.; Sportelli, L. *Biochimica et Biophysica Acta (BBA) - Biomembranes* **2003**, *1615*, 33.

(9)   Needham, D.; McIntosh, T. J.; Lasic, D. D. *Biochimica Et Biophysica Acta* **1992**, *1108*, 40.

(10)   BeduAddo, F. K.; Tang, P.; Xu, Y.; Huang, L. *Pharm. Res.* **1996**, *13*, 710.

(11)   Brož, P.; Benito, S. M.; Saw, C.; Burger, P.; Heider, H.; Pfisterer, M.; Marsch, S.; Meier, W.; Hunziker, P. *Journal of Controlled Release* **2005**, *102*, 475.

(12)   Uchegbu, I. F. *Expert Opinion on Drug Delivery* **2006**, *3*, 629.

(13)   Ahmed, F.; Pakunlu, R. I.; Brannan, A.; Bates, F.; Minko, T.; Discher, D. E. *Journal of Controlled Release* **2006**, *116*, 150.

(14)   Grzelakowski, M.; Onaca, O.; Rigler, P.; Kumar, M.; Meier, W. *Small* **2009**, *5*, 2545.

(15)   Egli, S.; Schlaad, H.; Bruns, N.; Meier, W. *Polymers* **2011**, *3*, 252.

(16)   Lin, J. J.; Bates, F. S.; Hammer, D. A.; Silas, J. A. *Phys. Rev. Lett.* **2005**, *95*, 026101.

(17)   Lin, J. J.; Silas, J. A.; Bermudez, H.; Milam, V. T.; Bates, F. S.; Hammer, D. A. *Langmuir* **2004**, *20*, 5493.

(18)   Longo, G. S.; Thompson, D. H.; Szleifer, I. *Langmuir* **2008**, *24*, 10324.

(19)   Russel, W. B.; Saville, D. A.; Schowalter, W. R. *Colloidal dispersions*; 1st ed.; Cambridge University Press: New York, NY, 1999.

(20)   Asakura, S.; Oosawa, F. *The Journal of Chemical Physics* **1954**, *22*, 1255.

(21)   Robbins, M. O.; Kremer, K.; Grest, G. S. *The Journal of Chemical Physics* **1988**, *88*, 3286.

(22)   Alder, B. J.; Wainwright, T. E. *The Journal of Chemical Physics* **1957**, *27*, 1208.

(23)   Holtz, J. H.; Asher, S. A. *Nature* **1997**, *389*, 829.

(24)   Joannopoulos, J. D. *Nature* **2001**, *414*, 257.

(25)   Langmuir, I. *Journal of Chemical Physics* **1938**, *6*, 873.

(26)   Zocher, H. *Zeitschrift für anorganische und allgemeine Chemie* **1925**, *147*, 91.

(27)   Bawden, F. C.; Pirie, N. W.; Bernal, J. D.; Fankuchen, I. *Nature* **1936**, *138*, 1051.

(28)   Onsager, L. *Annals of the New York Academy of Sciences* **1949**, *51*, 627.

(29)   Wensink, H. H.; Lekkerkerker, H. N. W. *Mol. Phys.* **2009**, *107*, 2111.

(30)   Frenkel, D.; Lekkerkerker, H. N. W.; Stroobants, A. *Nature* **1988**, *332*, 822.

(31)   Wensink, H. H. *Journal of Chemical Physics* **2007**, *126*.

(32)   Veerman, J. A. C.; Frenkel, D. *Physical Review A* **1992**, *45*, 5632.

(33)   Wen, X.; Meyer, R. B.; Caspar, D. L. D. *Phys. Rev. Lett.* **1989**, *63*, 2760.

(34)   Jana, N. R.; Gearheart, L. A.; Obare, S. O.; Johnson, C. J.; Edler, K. J.; Mann, S.; Murphy, C. J. *Journal of Materials Chemistry* **2002**, *12*, 2909.

(35)   van der Kooij, F. M.; Kassapidou, K.; Lekkerkerker, H. N. W. *Nature* **2000**, *406*, 868.

(36)   Woltman, S. J.; Jay, G. D.; Crawford, G. P. *Nat Mater* **2007**, *6*, 929.

(37)   Laschat, S.; Baro, A.; Steinke, N.; Giesselmann, F.; Hagele, C.; Scalia, G.; Judele, R.; Kapatsina, E.; Sauer, S.; Schreivogel, A.; Tosoni, M. *Angew. Chem.-Int. Edit.* **2007**, *46*, 4832.

(38)   Eppenga, R.; Frenkel, D. *Mol. Phys.* **1984**, *52*, 1303.

(39)   Bates, M. A.; Frenkel, D. *Journal of Chemical Physics* **1999**, *110*, 6553.

(40)   Allen, M. P. *Phys. Rev. Lett.* **1990**, *65*, 2881.

(41)   Lekkerkerker, H. N. W.; Coulon, P.; Vanderhaegen, R.; Deblieck, R. *Journal of Chemical Physics* **1984**, *80*, 3427.

(42)   Hemmen, H.; Ringdal, N. I.; De Azevedo, E. N.; Engelsberg, M.; Hansen, E. L.; Meheust, Y.; Fossum, J. O.; Knudsen, K. D. *Langmuir* **2009**, *25*, 12507.

(43)   Martinez-Raton, Y.; Velasco, E. *Journal of Chemical Physics* **2011**, *134*.

(44)   Sun, D. Z.; Sue, H. J.; Cheng, Z. D.; Martinez-Raton, Y.; Velasco, E. *Physical Review E* **2009**, *80*, 041704.

(45)   Michot, L. J.; Bihannic, I.; Maddi, S.; Funari, S. S.; Baravian, C.; Levitz, P.; Davidson, P. *Proc. Natl. Acad. Sci. U. S. A.* **2006**, *103*, 16101.

(46)   Yamaguchi, D.; Miyamoto, N.; Fujita, T.; Nakato, T.; Koizumi, S.; Ohta, N.; Yagi, N.; Hashimoto, T. *Physical Review E* **2012**, *85*, 011403.

(47)   Michot, L. J.; Bihannic, I.; Maddi, S.; Baravian, C.; Levitz, P.; Davidson, P. *Langmuir* **2008**, *24*, 3127.

(48)   Miyamoto, N.; Nakato, T. *The Journal of Physical Chemistry B* **2004**, *108*, 6152.

(49)   van der Beek, D.; Lekkerkerker, H. N. W. *Langmuir* **2004**, *20*, 8582.

(50)   van der Kooij, F. M.; Vogel, M.; Lekkerkerker, H. N. W. *Physical Review E* **2000**, *62*, 5397.

(51)   Ringdal, N. I.; Fonseca, D. M.; Hansen, E. L.; Hemmen, H.; Fossum, J. O. *Physical Review E* **2010**, *81*, 041702.

(52)   Sun, L. Y.; Boo, W. J.; Sue, H. J.; Clearfield, A. *New Journal of Chemistry* **2007**, *31*, 39.

(53)   Whitesides, G. M. *Nature* **2006**, *442*, 368.

(54)   Dittrich, P. S.; Manz, A. *Nat Rev Drug Discov* **2006**, *5*, 210.

(55)   Stone, H. A.; Stroock, A. D.; Ajdari, A. *Annual Review of Fluid Mechanics* **2004**, *36*, 381.

(56)   Seiler, K.; Harrison, D. J.; Manz, A. *Anal Chem* **1993**, *65*, 1481.

(57)   Harrison, D. J.; Manz, A.; Fan, Z.; Luedi, H.; Widmer, H. M. *Anal Chem* **1992**, *64*, 1926.

(58)   Ng, J. M. K.; Gitlin, I.; Stroock, A. D.; Whitesides, G. M. *Electrophoresis* **2002**, *23*, 3461.

(59)   Teh, S. Y.; Lin, R.; Hung, L. H.; Lee, A. P. *Lab on a Chip* **2008**, *8*, 198.

(60)   Anna, S. L.; Bontoux, N.; Stone, H. A. *Appl. Phys. Lett.* **2003**, *82*, 364.

(61)   Garstecki, P.; Fuerstman, M. J.; Stone, H. A.; Whitesides, G. M. *Lab on a Chip* **2006**, *6*, 437.

(62)   Utada, A. S.; Lorenceau, E.; Link, D. R.; Kaplan, P. D.; Stone, H. A.; Weitz, D. A. *Science* **2005**, *308*, 537.

(63)   Dendukuri, D.; Doyle, P. S. *Adv. Mater.* **2009**, *21*, 4071.

(64)   Shim, J. U.; Cristobal, G.; Link, D. R.; Thorsen, T.; Fraden, S. *Crystal Growth & Design* **2007**, *7*, 2192.

(65)   Gong, T.; Shen, J.; Hu, Z.; Marquez, M.; Cheng, Z. *Langmuir* **2007**, *23*, 2919.

(66)   Li, L.; Ismagilov, R. F. *Annu Rev Biophys* **2010**, *39*, 139.

(67)   Lee, M. H.; Prasad, V.; Lee, D. *Langmuir* **2010**, *26*, 2227.

(68)   Dinsmore, A. D.; Hsu, M. F.; Nikolaides, M. G.; Marquez, M.; Bausch, A. R.; Weitz, D. A. *Science* **2002**, *298*, 1006.

(69)   Kinnibrugh, K. G.; Chang, Y.-W.; Casey, L. M.; Silas, J. A.; Cheng, Z. 2009.

(70)   Lakowicz, J. R. *Principles of fluorescence spectroscopy*; 3rd ed.; Springer, 2006.

(71)   Stevens, B. *Chemical Physics Letters* **1987**, *134*, 519.

(72)   Giri, R. *Spectrochimica Acta Part A: Molecular and Biomolecular Spectroscopy* **2004**, *60*, 757.

(73)   Moriya, T. *Bulletin of the Chemical Society of Japan* **1984**, *57*, 1723.

(74)   Chris, D. G. *Measurement Science and Technology* **2001**, R53.

(75)   Rechthaler, K.; Köhler, G. *Chemical Physics* **1994**, *189*, 99.

(76)   Nad, S.; Pal, H. *The Journal of Physical Chemistry A* **2000**, *104*, 673.

(77)   Tablet, C.; Hillebrand, M. *Journal of Photochemistry and Photobiology A: Chemistry* **2007**, *189*, 73.

(78)   Casciola, M.; Alberti, G.; Donnadio, A.; Pica, M.; Marmottini, F.; Bottino, A.; Piaggio, P. *Journal of Materials Chemistry* **2005**, *15*, 4262.

(79)   Casciola, M.; Capitani, D.; Donnadio, A.; Munari, G.; Pica, M. *Inorganic Chemistry* **2010**, *49*, 3329.

(80)   He, P.; Mejia, A. F.; Cheng, Z. D.; Sun, D. Z.; Sue, H. J.; Dinair, D. S.; Marquez, M. *Physical Review E* **2010**, *81*.

(81)   Berne, B. J.; Pecora, R. *Dynamic Light Scattering: With Applications to Chemistry, Biology, and Physics*; Dover: Mineola, NY, 2000.

(82)   Xia, Y.; Whitesides, G. M. *Angewandte Chemie International Edition* **1998**, *37*, 550.

(83)   Discher, B. M.; Bermudez, H.; Hammer, D. A.; Discher, D. E.; Won, Y. Y.; Bates, F. S. *J. Phys. Chem. B* **2002**, *106*, 2848.

(84)   Discher, B. M.; Hammer, D. A.; Bates, F. S.; Discher, D. E. *Current Opinion in Colloid & Interface Science* **2000**, *5*, 125.

(85)   Discher, B. M.; Won, Y. Y.; Ege, D. S.; Lee, J. C. M.; Bates, F. S.; Discher, D. E.; Hammer, D. A. *Science* **1999**, *284*, 1143.

(86)   Bermudez, H.; Hammer, D. A.; Discher, D. E. *Langmuir* **2004**, *20*, 540.

(87)   Skalak, R.; Zarda, P. R.; Jan, K. M.; Chien, S. *Biophysical Journal* **1981**, *35*, 771.

(88)   Neu, B.; Meiselman, H. J. *Biophysical Journal* **2002**, *83*, 2482.

(89)   Marenduzzo, D.; Finan, K.; Cook, P. R. *The Journal of Cell Biology* **2006**, *175*, 681.

(90)   Lee, J.; Lentz, B. R. *Proceedings of the National Academy of Sciences* **1998**, *95*, 9274.

(91)   Lentz, B. R. *Eur. Biophys. J. Biophys. Lett.* **2007**, *36*, 315.

(92)   Evans, E.; Needham, D. *Macromolecules* **1988**, *21*, 1822.

(93)   Evans, E.; Needham, D. *Macromolecules* **2002**, *21*, 1822.

(94)   Seifert, U.; Lipowsky, R. *Physical Review A* **1990**, *42*, 4768.

(95)   Das, S.; Du, Q. *Physical Review E* **2008**, *77*, 011907.

(96)   Nam, J.; Santore, M. M. *Phys. Rev. Lett.* **2011**, *107*, 078101.

(97)   Jeppesen, C.; Wong, J. Y.; Kuhl, T. L.; Israelachvili, J. N.; Mullah, N.; Zalipsky, S.; Marques, C. M. *Science* **2001**, *293*, 465.

(98)   Moore, N. W.; Kuhl, T. L. *Langmuir* **2006**, *22*, 8485.

(99)   Longo, G.; Szleifer, I. *Langmuir* **2005**, *21*, 11342.

(100)   Evans, E. A. *Biophysical Journal* **1985**, *48*, 175.

(101)   Evans, E. A. *Biophysical Journal* **1985**, *48*, 185.

(102)   Paula, S.; Volkov, A. G.; Deamer, D. W. *Biophysical Journal* **1998**, *74*, 319.

(103)   Zeng, H.; Durocher, G. *Journal of Luminescence* **1995**, *63*, 75.

(104)   Yasuda, H.; Lamaze, C. E.; Ikenberry, L. D. *Die Makromolekulare Chemie* **1968**, *118*, 19.

(105)   Vrij, A. *Pure and Applied Chemistry* **1976**, *48*, 471.

(106) Ramachandran, A.; Anderson, T. H.; Leal, L. G.; Israelachvili, J. N. *Langmuir* **2010**, *27*, 59.

(107) Ziherl, P.; Svetina, S. *Proceedings of the National Academy of Sciences* **2007**, *104*, 761.

(108) Manyuhina, O. V.; Fasolino, A.; Christianen, P. C. M.; Katsnelson, M. I. *Physical Review E* **2009**, *80*, 010403.

(109) Shedlovsky, T. *J. Am. Chem. Soc.* **1932**, *54*, 1411.

(110) Wang, S. C.; Tsao, H. K. *Macromolecules* **2003**, *36*, 9128.

(111) Masaro, L.; Zhu, X. X. *Prog. Polym. Sci.* **1999**, *24*, 731.

(112) Vrentas, J. S.; Duda, J. L. *Journal of Polymer Science: Polymer Physics Edition* **1977**, *15*, 417.

(113) Vrentas, J. S.; Duda, J. L. *Journal of Polymer Science: Polymer Physics Edition* **1977**, *15*, 403.

(114) Landry, M. R.; Gu, Q.; Yu, H. *Macromolecules* **1988**, *21*, 1158.

(115) Yu, D. H. S.; Torkelson, J. M. *Macromolecules* **1988**, *21*, 1033.

(116) Wisnudel, M. B.; Torkelson, J. M. *Macromolecules* **1996**, *29*, 6193.

(117) Sandler, S. I. *Chemical, bIochemical, and engineering thermodynamics*; 4th ed.; John wiley & Sons, Inc., 2006.

(118) Ozdemir, C.; Guner, A. *Journal of Applied Polymer Science* **2006**, *101*, 203.

(119) Unsworth, L. D.; Tun, Z.; Sheardown, H.; Brash, J. L. *Journal of Colloid and Interface Science* **2006**, *296*, 520.

(120) Dewhurst, P. F.; Lovell, M. R.; Jones, J. L.; Richards, R. W.; Webster, J. R. P. *Macromolecules* **1998**, *31*, 7851.

(121) Faure, M. C.; Bassereau, P.; Lee, L. T.; Menelle, A.; Lheveder, C. *Macromolecules* **1999**, *32*, 8538.

(122) Dan, N.; Tirrell, M. *Macromolecules* **1993**, *26*, 6467.

(123) Currie, E. P. K.; Wagemaker, M.; Cohen Stuart, M. A.; van Well, A. A. *Macromolecules* **1999**, *32*, 9041.

(124) Elman, J. F.; Johs, B. D.; Long, T. E.; Koberstein, J. T. *Macromolecules* **1994**, *27*, 5341.

(125) Priolo, M. A.; Gamboa, D.; Grunlan, J. C. *Acs Applied Materials & Interfaces* **2010**, *2*, 312.

(126) Wang, K.; Chen, L.; Wu, J.; Toh, M. L.; He, C.; Yee, A. F. *Macromolecules* **2005**, *38*, 788.

(127) Stankovich, S.; Dikin, D. A.; Dommett, G. H. B.; Kohlhaas, K. M.; Zimney, E. J.; Stach, E. A.; Piner, R. D.; Nguyen, S. T.; Ruoff, R. S. *Nature* **2006**, *442*, 282.

(128) Xu, Z.; Gao, C. *Nat Commun* **2011**, *2*, 571.

(129) Nakato, T.; Miyamoto, N.; Harada, A. *Chem Commun* **2004**, 78.

(130) Martinez-Haya, B.; Cuetos, A. *Physical Review E* **2010**, *81*, 4.

(131) Delhorme, M.; Labbez, C.; Jönsson, B. *The Journal of Physical Chemistry Letters* **2012**, 1315.

(132) Zhang, S. D.; Reynolds, P. A.; van Duijneveldt, J. S. *Journal of Chemical Physics* **2002**, *117*, 9947.

(133) Keller, S. W.; Kim, H.-N.; Mallouk, T. E. *J. Am. Chem. Soc.* **1994**, *116*, 8817.

(134) Kim, H.-N.; Keller, S. W.; Mallouk, T. E.; Schmitt, J.; Decher, G. *Chemistry of Materials* **1997**, *9*, 1414.

(135) Clearfield, A. *Inorganic ion exchange materials*; CRC Press, 1982.

(136) Sue, H. J.; Gam, K. T.; Bestaoui, N.; Spurr, N.; Clearfield, A. *Chemistry of Materials* **2004**, *16*, 242.

(137) Alberti, G.; Casciola, M.; Costantino, U. *Journal of Colloid and Interface Science* **1985**, *107*, 256.

(138) Sun, L. Y.; O'Reilly, J. Y.; Kong, D. Y.; Su, J. Y.; Boo, W. J.; Sue, H. J.; Clearfield, A. *Journal of Colloid and Interface Science* **2009**, *333*, 503.

(139) Lubensky, T. C.; Renn, S. R. *Physical Review A* **1990**, *41*, 4392.

(140) Goodby, J. W. *Current Opinion in Colloid & Interface Science* **2002**, *7*, 326.

(141) Rossi, L.; Sacanna, S.; Velikov, K. P. *Soft Matter* **2011**, *7*, 64.

(142) van der Beek, D.; Petukhov, A. V.; Oversteegen, S. M.; Vroege, G. J.; Lekkerkerker, H. N. W. *European Physical Journal E* **2005**, *16*, 253.

(143) Marechal, M.; Cuetos, A.; Martinez-Haya, B.; Dijkstra, M. *The Journal of Chemical Physics* **2011**, *134*, 094501.

(144) Mejia, A. F.; Chang, Y.-W.; Ng, R.; Shuai, M.; Mannan, M. S.; Cheng, Z. D. *Physical Review E* **2012**, *In press*.

(145) Hristova, K.; Needham, D. *Macromolecules* **1995**, *28*, 991.

(146) Fang, M. M.; Kaschak, D. M.; Sutorik, A. C.; Mallouk, T. E. *J. Am. Chem. Soc.* **1997**, *119*, 12184.

(147) Bestaoui, N.; Spurr, N. A.; Clearfield, A. *Journal of Materials Chemistry* **2006**, *16*, 759.

(148) Boo, W. J.; Sun, L. Y.; Liu, J.; Moghbelli, E.; Clearfield, A.; Sue, H. J.; Pham, H.; Verghese, N. *Journal of Polymer Science Part B-Polymer Physics* **2007**, *45*, 1459.

(149) Horsley, S. E.; Nowell, D. V.; Stewart, D. T. *Spectrochimica Acta Part A: Molecular Spectroscopy* **1974**, *30*, 535.

(150) Yang, H. C.; Aoki, K.; Hong, H. G.; Sackett, D. D.; Arendt, M. F.; Yau, S. L.; Bell, C. M.; Mallouk, T. E. *J. Am. Chem. Soc.* **1993**, *115*, 11855.

(151) van der Beek, D.; Lekkerkerker, H. N. W. *Europhysics Letters* **2003**, *61*, 702.

(152) Mourchid, A.; Delville, A.; Lambard, J.; Lecolier, E.; Levitz, P. *Langmuir* **1995**, *11*, 1942.

(153) Gabriel, J. C. P.; Sanchez, C.; Davidson, P. *Journal of Physical Chemistry* **1996**, *100*, 11139.

(154) Lubensky, T. C.; Mukhopadhyay, R.; Radzihovsky, L.; Xing, X. J. *Physical Review E* **2002**, *66*, 011702.

(155) Lacoste, D.; Lau, A. W. C.; Lubensky, T. C. *European Physical Journal E* **2002**, *8*, 403.

(156) Russel, W. B.; Saville, D. A.; Schowalter, W. R. In *Colloidal Dispersions*; 1st ed.; Cambridge University Press: New York, NY, 1999, p 347.

(157) Michot, L. J.; Baravian, C.; Bihannic, I.; Maddi, S.; Moyne, C.; Duval, J. F. L.; Levitz, P.; Davidson, P. *Langmuir* **2009**, *25*, 127.

(158) Michot, L. J.; Bihannic, I.; Porsch, K.; Maddi, S.; Baravian, C.; Mougel, J.; Levitz, P. *Langmuir* **2004**, *20*, 10829.

(159) Mourchid, A.; Lecolier, E.; Van Damme, H.; Levitz, P. *Langmuir* **1998**, *14*, 4718.

(160) Viasnoff, V.; Lequeux, F. o.; Pine, D. J. *Review of Scientific Instruments* **2002**, *73*, 2336.

(161) Di, X. J.; Win, K. Z.; McKenna, G. B.; Narita, T.; Lequeux, F.; Pullela, S. R.; Cheng, Z. D. *Phys. Rev. Lett.* **2011**, *106*.

(162) Mourad, M. C. D.; Byelov, D. V.; Petukhov, A. V.; de Winter, D. A. M.; Verkleij, A. J.; Lekkerkerker, H. N. W. *J. Phys. Chem. B* **2009**, *113*, 11604.

(163) Kaschak, D. M.; Johnson, S. A.; Hooks, D. E.; Kim, H. N.; Ward, M. D.; Mallouk, T. E. *J. Am. Chem. Soc.* **1998**, *120*, 10887.

(164) Alberti, G.; Marmottini, F. *Journal of Colloid and Interface Science* **1993**, *157*, 513.

(165) Leong, Y.-K.; Scales, P. J.; Healy, T. W.; Boger, D. V. *Journal of the American Ceramic Society* **1995**, *78*, 2209.

(166) Trappe, V.; Prasad, V.; Cipelletti, L.; Segre, P. N.; Weitz, D. A. *Nature* **2001**, *411*, 772.

(167) Segre, P. N.; Prasad, V.; Schofield, A. B.; Weitz, D. A. *Phys. Rev. Lett.* **2001**, *86*, 6042.

(168) Kummerlowe, G.; Luy, B. In *Annual Reports on Nmr Spectroscopy, Vol 68*; Webb, G. A., Ed. 2009; Vol. 68, p 193.

(169) Tjandra, N. *Struct. Fold. Des.* **1999**, *7*, R205.

(170) Tjandra, N.; Bax, A. *Science* **1997**, *278*, 1111.

(171)   Prestegard, J. H.; Bougault, C. M.; Kishore, A. I. *Chemical Reviews* **2004**, *104*, 3519.

(172)   Sanders, C. R.; Prosser, R. S. *Structure* **1998**, *6*, 1227.

(173)   Desvaux, H.; Gabriel, J. C. P.; Berthault, P.; Camerel, F. *Angew. Chem.-Int. Edit.* **2001**, *40*, 373.

(174)   Fleming, K.; Gray, D.; Prasannan, S.; Matthews, S. *J. Am. Chem. Soc.* **2000**, *122*, 5224.

(175)   Troutier, A. L.; Ladaviere, C. *Adv. Colloid Interface Sci.* **2007**, *133*, 1.

(176)   Sackmann, E. *Science* **1996**, *271*, 43.

(177)   Cremer, P. S.; Boxer, S. G. *J. Phys. Chem. B* **1999**, *103*, 2554.

(178)   Plant, A. L. *Langmuir* **1993**, *9*, 2764.

(179)   MacDonald, R. C.; MacDonald, R. I.; Menco, B. P. M.; Takeshita, K.; Subbarao, N. K.; Hu, L.-r. *Biochimica et Biophysica Acta (BBA) - Biomembranes* **1991**, *1061*, 297.

(180)   Tamm, L. K.; McConnell, H. M. *Biophysical Journal* **1985**, *47*, 105.

(181)   Levin, C. S.; Kundu, J.; Janesko, B. G.; Scuseria, G. E.; Raphael, R. M.; Halas, N. J. *J. Phys. Chem. B* **2008**, *112*, 14168.

(182)   Moura, S. P.; Carmona-Ribeiro, A. M. *Langmuir* **2005**, *21*, 10160.

(183)   Troutier, A. L.; Delair, T.; Pichot, C.; Ladaviere, C. *Langmuir* **2005**, *21*, 1305.

(184)   Nordlund, G.; Lönneborg, R.; Brzezinski, P. *Langmuir* **2009**, *25*, 4601.

(185)   Lopez-Leon, T.; Fernandez-Nieves, A. *Colloid and Polymer Science* **2011**, *289*, 345.

(186)   Volovik, G. E.; Lavrentovich, O. D. *Zhurnal Eksperimentalnoi I Teoreticheskoi Fiziki* **1983**, *85*, 1997.

(187)   Gupta, J. K.; Sivakumar, S.; Caruso, F.; Abbott, N. L. *Angewandte Chemie International Edition* **2009**, *48*, 1652.

(188) Fernández-Nieves, A.; Vitelli, V.; Utada, A. S.; Link, D. R.; Márquez, M.; Nelson, D. R.; Weitz, D. A. *Phys. Rev. Lett.* **2007**, *99*, 157801.

(189) Sivakumar, S.; Wark, K. L.; Gupta, J. K.; Abbott, N. L.; Caruso, F. *Adv Funct Mater* **2009**, *19*, 2260.

(190) Lin, I.-H.; Miller, D. S.; Bertics, P. J.; Murphy, C. J.; de Pablo, J. J.; Abbott, N. L. *Science* **2011**, *332*, 1297.

(191) Moreno-Razo, J. A.; Sambriski, E. J.; Abbott, N. L.; Hernandez-Ortiz, J. P.; de Pablo, J. J. *Nature* **2012**, *485*, 86.

(192) Liang, H. L.; Schymura, S.; Rudquist, P.; Lagerwall, J. *Phys. Rev. Lett.* **2011**, *106*.

(193) Lopez-Leon, T.; Fernandez-Nieves, A.; Nobili, M.; Blanc, C. *Phys. Rev. Lett.* **2011**, *106*.

(194) Binks, B. P. *Current Opinion in Colloid & Interface Science* **2002**, *7*, 21.

(195) Binks, B. P.; Rodrigues, J. A.; Frith, W. J. *Langmuir* **2007**, *23*, 3626.

(196) Reger, M.; Sekine, T.; Okamoto, T.; Watanabe, K.; Hoffmann, H. *Soft Matter* **2011**, *7*, 11021.

(197) Opawale, F. O.; Burgess, D. J. *Journal of Colloid and Interface Science* **1998**, *197*, 142.

(198) Bon, S. A. F.; Mookhoek, S. D.; Colver, P. J.; Fischer, H. R.; van der Zwaag, S. *European Polymer Journal* **2007**, *43*, 4839.

(199) Studart, A. R.; Shum, H. C.; Weitz, D. A. *The Journal of Physical Chemistry B* **2009**, *113*, 3914.

(200) Pawar, A. B.; Caggioni, M.; Ergun, R.; Hartel, R. W.; Spicer, P. T. *Soft Matter* **2011**, *7*, 7710.

(201) Zhang, L.; Gorset, W.; Dresser, M. J.; Giacomini, K. M. *Journal of Pharmacology and Experimental Therapeutics* **1999**, *288*, 1192.

(202) Nie, Z. H.; Seo, M. S.; Xu, S. Q.; Lewis, P. C.; Mok, M.; Kumacheva, E.; Whitesides, G. M.; Garstecki, P.; Stone, H. A. *Microfluidics and Nanofluidics* **2008**, *5*, 585.

(203) Ward, T.; Faivre, M.; Abkarian, M.; Stone, H. A. *ELECTROPHORESIS* **2005**, *26*, 3716.

(204) Merkel, K.; Kocot, A.; Vij, J. K.; Korlacki, R.; Mehl, G. H.; Meyer, T. *Phys. Rev. Lett.* **2004**, *93*, 237801.

(205) Cui, Y. N.; Threlfall, M.; van Duijneveldt, J. S. *Journal of Colloid and Interface Science* **2011**, *356*, 665.

(206) Klochkov, V. V.; Klochkov, A. V.; Thiele, C. M.; Berger, S. *Journal of Magnetic Resonance* **2006**, *179*, 58.

(207) Bianchi, E.; Largo, J.; Tartaglia, P.; Zaccarelli, E.; Sciortino, F. *Phys. Rev. Lett.* **2006**, *97*, 4.

(208) Russo, J.; Tartaglia, P.; Sciortino, F. *Journal of Chemical Physics* **2009**, *131*.

(209) Zaccarelli, E.; Buldyrev, S. V.; La Nave, E.; Moreno, A. J.; Saika-Voivod, I.; Sciortino, F.; Tartaglia, P. *Phys. Rev. Lett.* **2005**, *94*.

(210) Glotzer, S. C.; Solomon, M. J. *Nature Materials* **2007**, *6*, 557.

(211) Caswell, K. K.; Wilson, J. N.; Bunz, U. H. F.; Murphy, C. J. *J. Am. Chem. Soc.* **2003**, *125*, 13914.

(212) Hiddessen, A. L.; Rodgers, S. D.; Weitz, D. A.; Hammer, D. A. *Langmuir* **2000**, *16*, 9744.

(213) Zaccarelli, E. *Journal of Physics-Condensed Matter* **2007**, *19*.

(214) Ruzicka, B.; Zaccarelli, E.; Zulian, L.; Angelini, R.; Sztucki, M.; Moussaid, A.; Narayanan, T.; Sciortino, F. *Nature Materials* **2011**, *10*, 56.

(215) Zhang, Z. X.; van Duijneveldt, J. S. *Journal of Chemical Physics* **2006**, *124*.

VITA

Ya-Wen Chang received her Bachelor of Science degree in chemical engineering from National Taiwan University, Taiwan in June 2006. In August 2006, she entered the doctorate program in chemical engineering department at Texas A&M University and received her Ph.D. degree in August 2012.

Ya-Wen may be reached at yawenwin@gmail.com or through Dr. Zhengdong Cheng at Chemical Engineering Department, Texas A&M University, College Station, TX 77843-3122.